UNIVERSITY OF OKLAHOMA
GRADUATE COLLEGE

BUTTON SAMPLE HOLDER APPLICATIONS FOR MID-INFRARED SPECTROSCOPY STUDIES OF MINERALS

A DISSERTATION
SUBMITTED TO THE GRADUATE FACULTY
in partial fulfillment of the requirements for the
Degree of
DOCTOR OF PHILOSOPHY

BY
HEIDI F. NONEMAN
Norman, Oklahoma
2025

Downloaded from SHAREOK. Persistent Handle URL: https://hdl.handle.net/11244/341216

BUTTON SAMPLE HOLDER APPLICATIONS FOR MID-INFRARED SPECTROSCOPY STUDIES OF MINERALS

A DISSERTATION APPROVED FOR THE
DEPARTMENT OF CHEMISTRY AND BIOCHEMISTRY

BY THE COMMITTEE CONSISTING OF

Dr. Robert L. White, Chair

Dr. Mark A. Nanny

Dr. Zhibo Yang

Dr. Christina R. Bourne

© Copyright by HEIDI F. NONEMAN 2025
All Rights Reserved.

This work is dedicated to my family. To my parents, I am eternally grateful for your lifelong support and guidance. Without you, I would never have had the courage to enter into this pursuit. To my husband Andrew, your persistence, encouragement, and love inspire me every day. Your strength bolstered me when I doubted myself and gave me the drive to complete this journey.

Acknowledgements

I would like to thank Dr. Robert L. White for his guidance, patience, and instruction. I am grateful and humbled to have grown under the tutelage of such an amazing chemist and frontier thinker. Your keen curiosity for innovation and dedication to your craft inspires me to expand my thinking and to become a better scientist. Thank you for engaging in conversation over new ideas, promoting an environment where students felt they had a voice, and always catching me up to speed on the latest workings of your brain.

I would like to thank Dr. Mark A. Nanny for his input and constructive critiques that forced me to demonstrate the potential impact of my research. I would like to thank Dr. Zhibo Yang and Dr. Christina Bourne for their willingness to join my committee and learn about my Ph.D. journey at its sunset. I would like to thank Dr. Si Wu and Dr. Laura Isobel-McCall for their guidance and encouragement in the early years of my Ph.D. pursuit. Additionally, I would like to thank Jaspreet Singh for welcoming me into the White Lab and always being willing to show me the ropes.

Finally, a special thanks goes to my parents, husband, and all the former academic mentors that brought me to this point. To my mom Janice Noneman who fostered a love of science in me from a young age and a desire to leave the world better than I found it - thank you. To my dad Gary Noneman who spent countless hours nurturing my intellectual curiosities, teaching me to strive for perfection, and

pushing me to shoot for the moon believing all the while that I could get there – thank you. To my husband Andrew Krug for always challenging me to delve deeper, think bigger, and pushing me to be my best – thank you. To Professor Elizabeth Snipes, Dean James Ruebel, Dr. Patricia Lang, Dr. James Rybarczyk for recognizing and cultivating my potential as both a scholar and a chemist – thank you. I truly appreciate all of the love, effort, and knowledge you all have poured into me to make this moment possible. I can only hope to make you proud and leave the world better than I found it.

Abstract

Infrared (IR) spectroscopy is a rapid and non-destructive molecular analysis method derived from the infrared radiation and matter. Its use is prevalent throughout industrial, academic, and government laboratories for materials characterization. Despite its ubiquity, major advancements in methods or sampling techniques have been largely stagnant since the 1960's. This dissertation presents mid-IR spectroscopy mineralogical applications of a novel button sample holder and describes various analytical features of this new technique.

Buttons are manufactured by spot welding various sizes of stainless-steel meshes to polished stainless-steel backings. The thin wire mesh and shallow well of a button sample holder allow for easy preparation and analysis of thin layers of neat solid, liquid, paste, and grease samples. Additionally, radiation reflected off the steel wires and backing allow for diffuse reflectance infrared Fourier transform spectroscopy (DRIFTS) analysis of non-scattering samples like liquids.

Button sample holders eliminate the necessity of time-consuming, expensive, and potentially sample altering predilution and handling. The sieving ability of the mesh selects for particle sizes smaller than the void sizes of the mesh. Well depth and wire diameter limit the maximum allowable sample layer thickness. Furthermore, the robust button design permits abrasive sampling which removes small amounts of sample by simply rubbing the rough button mesh over a sample surface. This method is applicable to in-situ sampling, storage, and analysis. It is

especially ideal for samples where minimal damage is desired and sample homogenization is not possible, such as archaeological and historical artifacts.

Traditional DRIFTS and variable temperature DRIFTS (VT-DRIFTS) were employed for this body of work. Diffuse reflectance from the samples and button is collected at all angles except the incident radiation angle. Total pathlengths on the order of a few microns are possible, thus permitting analyses of high absorptivity neat samples, such as coals and carbon black. With attention to particle size homogenization, mesh choice, and sample packing, layer thickness could be reproducibly adjusted. Versatility of sample type and variable total pathlengths offer an advantage over conventional methods like attenuated total reflectance infrared spectroscopy (ATR-IR).

The sensitivity and reproducibility of VT-DRIFTS measurements with button sample holders was demonstrated through various mineralogical applications. The first of these studies, performed on clay minerals such as kaolinite, was done with a modified traditional VT-DRIFTS setup after replacing the sample cup with a button sample holder and removing the sealed environmental chamber. This increased optical throughput, eliminated diluent interactions, and mitigated temperature-dependent alignment issues. It also enhanced measurement sensitivity and minimized spectral artifacts.

The utility of Button VT-DRIFTS was further enhanced through the construction of a heating and cooling block made of stacked thermoelectric chips.

Using this device, infrared spectra at temperatures between -40 °C and 150 °C could be reached and maintained within seconds. This apparatus was combined with a programmable temperature controller to implement unique heating and cooling profiles. Continuous and step temperature profiles could be applied to probe different sample properties and discriminate between reversible and irreversible changes. This allowed for a quick pre-analysis to determine if further exploration of temperature-dependent changes in particular samples is warranted.

The innovative thermoelectric heating and cooling apparatus was combined with button sample holders to investigate molecular level dehydration and rehydration processes and low temperature induced structural changes in additional mineral samples. Reversible and irreversible temperature-dependent changes were observed via spectral subtractions using this method. These differences are not readily apparent when simply overlaying spectra of samples before and after cooling. Furthermore, conventional variable temperature studies often require probing large temperature differences or using multiple samples. This methodology uniquely allows for variable temperature studies of temperature-dependent structural changes on a single sample. The selectivity and reproducibility of Button VT-DRIFTS studies permitted monitoring and discrimination of changes in different hydroxyl group types in solid state mineral samples.

Table of Contents

Acknowledgements v

Abstract vii

Table of Contents x

Figures List xiv

Chapter 1: Introduction 1

1.1 Spectroscopy 1

1.1.1 Origins 1

1.1.2 Working Principle 4

1.2 Infrared Spectroscopy 9

1.3 IR Active Vibrations 10

1.4 IR Spectral Regions 18

1.5 Mid-IR Transmission Spectroscopy 19

1.6 Mid-IR Reflectance Spectroscopy 22

1.6.1 Specular Reflectance 23

1.6.2 Attenuated Total Reflectance 24

1.6.3 Diffuse Reflectance 25

1.6.4 Variable Temperature Diffuse Reflectance Infrared Fourier Transform Spectroscopy 29

1.7 Hyphenated Systems 30

Chapter 2: Button-IR Design, Working Principle, and Sampling Considerations 32

2.1 Introduction 32

2.1.1 Instrumentation 33

2.2 Button Sample Holder 35

2.2.1 Button Fabrication 35

2.3 Button-IR VT-DRIFTS Heating Configurations 40

2.3.1 Quartz Holder VT-DRIFTS Apparatus 40

2.3.2 Button-IR with Thermoelectric Chip Heating/Cooling 43

2.4 Working Principle 49

2.5 Sampling Considerations 51

2.5.1 Liquid Sample Loading 52

2.5.2 Solid Sample Loading 54

2.5.3 Abrasion Sample Loading 59

2.6 Button Sample Holder Orientation 62

2.6.1 Method 63

2.6.1 Button Rotation Studies 65

2.7 Summary 69

Chapter 3: A High Sensitivity Variable Temperature Diffuse Reflectance Infrared Fourier Transform Spectroscopy Investigation of Temperature Dependent Structure Changes in Kaolinite 70

3.1 Background 70

3.1.1 Introduction 70

3.1.2 Kaolinite 71

3.2 Experimental 74

3.3 Results and Discussion 76

3.4. Conclusions 95

Chapter 4: Diffuse Reflectance Infrared Studies of Minerals 98

4.1 Introduction 98

4.2 Apparatus 103

4.3 Temperature versus Time Profiles 105

4.4 Sample Mineral Thermal Properties 109

4.4.1 Silica 110

4.4.2 Montmorillonite Clay 122

4.4.3 Gypsum 128

4.4.4 Coal 138

4.5 Summary and Conclusions 151

Chapter 5: Conclusions and Looking Forward 155

References 162

Appendix A – Mesh Photos and Laser Scattering Properties 198

Appendix B – Crystal Modeling Parameters 201

Appendix C – Copyright 202

Figures List

Figure 1.1: Schematic of Isaac Newton's prism experiment demonstrating the refraction and dispersion of white light into seven colors. Wavelength ranges of visible light consist of: Red (750-625 nm), Orange (625-590 nm), Yellow (590-565 nm), Green (565-500 nm), Blue (500-485 nm), Indigo (485-450nm), Violet (450-380 nm).....2

Figure 1.2: The sun produces a continuous spectrum(bottom). Fraunhofer lines are the names of dark lines appearing in the fully dispersed solar spectrum (top) due to absorption by gases in the atmosphere and outer photosphere of the sun.....4

Equation 1.1: Planck's Equation.....6

Figure 1.3: Electromagnetic spectrum in wavelength.....6

Figure 1.4: Morse potential energy curve showing the vibrational levels for a given electronic state of a diatomic molecule. Rotational levels are between discreet vibrational levels. Vibrational and rotational transitions can be observed by using infrared (IR) spectroscopy. 7

Figure 1.5: Representation of a theoretical HOMO – LUMO transition in UV spectroscopy. 8

Figure 1.6: The homonuclear diatomic molecule O_2 is not IR active due to its lack of a dipole moment change during stretching. The heteronuclear diatomic

molecule HCl is IR active because its dipole moment changes during the stretching vibration. 11

Equation 1.2: Natural frequency of a harmonic oscillator vibration. 12

Figure 1.7: Common stretching and bending vibration modes in polyatomic molecules. (+) indicates a motion in front of the plane and (-) indicates a motion behind the plane. 13

Table 1.1: Factors Determining the Number of Experimental Vibrational Modes[49] 14

Figure 1.8: Schematic of symmetric and asymmetric stretching vibrations for carbon dioxide (CO_2) and water (H_2O), demonstrating how molecular shape can influence the IR activity of these vibrations. 15

Equation 1.3: Equation for the calculation of vibrational modes possible for a molecule. 16

Equation 1.4: Wavenumber (ν) as it mathematically relates to wavelength (λ), the speed of light (c), Planck's constant (h), and photon energy (E). 18

Figure 1.9: Schematic demonstration of how changing the incident angle can alter the pathlength in transflectance IR. Longer pathlengths result from larger incident angles. Shorter pathlengths result from smaller incident angles. ... 19

Figure 1.10: Schematic of a transmission IR liquid sample cell. 20

Equation 1.5: Beer's Law shows that Absorbance (A) is directly proportional to the molar absorptivity (ε), pathlength (b), and concentration (c). 21

Figure 1.11: Specular reflectance IR measures radiation reflected from the sample at the same angle as the incident angle. Diffuse reflectance IR measures radiation reflecting at all angles except for the specular angle. ATR-IR detects the radiation reaching the detector after it has passed through the ATR crystal and has been attenuated by evanescent wave interactions with the sample at the sample-crystal interface. 23

Equation 1.6: Kubelka-Munk transformation equation. 27

Figure 2.1: Photograph of the Praying Mantis optics. Ellipsoid mirrors are centered over a button sample holder at the end of a sample introduction slide. 35

Figure 2.2: Diagrams of the exposed mesh button and the recessed mesh button. The left shows a side view of the exposed mesh button next to a top view. The right shows the same views for a recessed mesh button. 36

Table 2.1: Listing of mesh sizes with wire diameter, cavity size, weave type, and the preferred sample type that each mesh is best suited for. 37

Figure 2.3: Photos of mesh sizes taken under approximately 30X magnification via a microscope (10X) and iPhone zoom (3X) to demonstrate various void sizes and weave patterns. 38

Figure 2.4: Photograph of fixed slider and rotating slider. 40

Figure 2.5: Diagram of the variable temperature diffuse reflection infrared spectroscopy apparatus with the button sample holder placed on top of a quartz tube containing a cartridge heater. Red arrows indicate the direction of

the heat transfer. The thermocouple is placed in contact with the sample surface..... 42
Figure 2.6: TEC button sample holder heater/cooler. 43
Figure 2.7: Button heating/cooling apparatus with stacked thermoelectric chips. The button sample holder used with this apparatus contained a permanently attached thermocouple. 46
Figure 2.8: (a) Empty, (b) solid, and (c) liquid filled buttons with typical reflections for each case. 49
Figure 2.9: Plots of emissivity versus wavenumber for empty buttons with 50, 100, and 200 meshes. 50
Figure 2.10: Plots of diffuse reflectance emissivity versus wavenumber for empty buttons containing 635 and 2800 wire meshes. 51
Figure 2.11: Paraffin oil spectra obtained by using half-filled 100, 635, and 2800 mesh buttons. Spectra were obtained at button rotation angles corresponding to maximum emissivity. 53
Figure 2.12: Turquoise sample baseline drift as a function of added material using the abrasion sample collection method. 57
Figure 2.13: Full button versus thin layer spectra of carbon black. The blue spectrum was obtained with a 100 mesh button filled to the top of the wires with carbon black. The orange spectrum was obtained by placing a thin layer of particles in the button. 58

Figure 2.14: (A) Photograph of sampling locations. (B) Spectra of stabilized turquoise sampled at the polymer coating and at a location that appears to be both polymer and turquoise. (C) Difference spectrum obtained by subtracting the polymer scrape spectra from the polymer and stone spectra. 60

Figure 2.15: Button orientation marker evolution: The first button prototype started out with no alignment markers. Once spectral changes due to button orientation were noted, an alignment mark was added as in the middle button. This alignment mark was a small indentation at one edge of the button. The alignment pin holes in the button on the right were added to further enhance alignment reproducibility. 63

Figure 2.16: Profile view of button cavity demonstrating different sample depths (i.e. different total pathlengths) due to wire curvature. 65

Figure 2.17: Plots of single beam intensity versus rotation angle for individual meshes (50, 100, 200, 635, 2800) 68

Figure 3.1: Diagram of the variable temperature diffuse reflection infrared spectroscopy apparatus with button sample holder. 71

Figure 3.2: Kaolinite Structure (a) Ball and stick (b) Crystal faces. Red balls represent oxygen atoms. Dark blue balls represent silicon atoms. Light blue balls represent aluminum atoms. White balls represent hydrogen atoms. The octahedral layer is highlighted with green crystal faces. The tetrahedral layer

is highlighted with red crystal faces. Crystal structure from Bish (1993).[164] Structural modelling was accomplished by using the VESTA software.[165] .. 73

Figure 3.3: (a) Overlay of infrared spectra measured while heating. (b) Overlay of five infrared spectra measured at 150 °C. (c) Overlay of infrared spectra measured while cooling. 79

Figure 3.4: Integrated absorbance for the adsorbed water H-O-H bending vibration band (solid line) and sample temperature (dash line) as a function of time. Straight lines denote linear regression best fit lines. 82

Figure 3.5: Top: DRIFTS spectra for kaolinite measured at 30 and 150 °C. Bottom: Relative standard deviations of measured intensities for three successively acquired spectra as a function of wavenumber. 84

Figure 3.6: (Top) VT-DRIFTS spectra obtained at 30 °C and (Bottom) difference spectra for (a) O-H stretching vibrations and (b) framework vibrations. 86

Figure 3.7: (a) VT-DRIFTS Band maximum location and (b) integrated band area variations as a function of time for the 3698 cm^{-1} (at 30 °C) O-H stretching vibration. Sample temperatures are denoted by the dash line in (a). 91

Figure 3.8: (a) VT-DRIFTS Band maximum location and (b) integrated band area variations as a function of time for the 3623 cm^{-1} (at 30 °C) O-H stretching vibration. Sample temperatures are denoted by the dash line in (a). 93

Figure 4.1: Photograph of a conventional button (left) and the modified button (right). 102

Figure 4.2: Top view of the sample heating/cooling apparatus. 104

Figure 4.3: (a) Linear heating/cooling ramp, (b) stair-step, and (c) step-up/down temperature programs. 107

Figure 4.4: (a) α-quartz structure crystal lattice model from Rosa et al.[214] (b) X-ray diffraction determined crystal structure from Glinnemann et al.[215] Structural modelling was accomplished by using the VESTA software.[165] (c) Left - profile depiction of an ideal hexagonal prismatic crystal. Middle – Realistic view from top of α-quartz pyramid (top) with offset prismatic faces (bottom). Right – hexagonal unit cell of α-quartz. 112

Figure 4.5: Representation of amorphous silica gel containing hydrogen bonded water molecules. 114

Figure 4.6: Infrared spectra for α-quartz (red) and silica gel (blue) (a) before heating and (b) at 150 °C. 117

Figure 4.7: Reversible (green) and irreversible (black) spectrum changes resulting from heating α-quartz to 150 °C. 119

Figure 4.8: Intensity versus step temperature (red) trends at 1208 cm^{-1} (triangles) and 1056 cm^{-1} (circles). Dashed lines denote intensities after cooling (blue) back to 30 °C. 120

Figure 4.9: Reversible (green) and irreversible (black) spectrum changes resulting from heating silica gel from 30 to 150 °C. 121

Figure 4.10: Integrated band area between 1700 and 1600 cm^{-1} (solid line) and sample temperature (dashed line) for silica gel plotted as a function of time. 122

Figure 4.11: Schematic of montmorillonite structure from Gournis et al.[225] Structural modelling was accomplished by using the VESTA software.[165] 123

Figure 4.12: Infrared spectra for montmorillonite clays enriched in K^+ (red) and Ca^{2+} (blue). 125

Figure 4.13: Irreversible spectrum changes resulting from heating to 150 °C for the K^+ (red) and Ca^{2+} (blue) enriched montmorillonite samples. 126

Figure 4.14: Band intensity area between 1700 and 1600 cm^{-1} versus time plots for the K^+ (red) and Ca^{2+} (blue) montmorillonite clay samples. The dashed line represents measured sample temperatures. 127

Figure 4.15: Schematic of the gypsum structure from Schofield et al.[233] Structural modelling was accomplished by using the VESTA software.[165] 129

Figure 4.16: Gypsum infrared spectra obtained at 30 °C, after heating to 150 °C, and after cooling back to 30 °C. 131

Figure 4.17: Integrated band intensity (area) spanning the O-H stretching vibration range (3800–3000 cm^{-1}) as a function of step temperature. Circles represent band areas from spectra obtained at the step temperatures and squares represent areas in spectra measured after cooling from those temperatures. 134

Figure 4.18: Gypsum infrared spectrum differences calculated by subtracting (a) the initial 30 °C spectrum from the 50 °C spectrum (solid) and the 50 °C spectrum from the subsequent 30 °C spectrum (dotted), (b) the 30 °C spectrum from the 80 °C spectrum (solid) and the 80 °C spectrum from the subsequent 30 °C spectrum (dotted), and (c) the 30 °C spectrum from the 150 °C spectrum (solid) and the 150 °C spectrum from the subsequent 30 °C spectrum (dotted). 137

Figure 4.19: (a) Infrared spectra of a lignite coal sample obtained at 25 °C (blue) and 150 (red) °C. (b) Reversible (blue) and irreversible (red) spectrum changes resulting from heating the lignite from 25 to 150 °C. 140

Figure 4.20: Incremental (a) reversible and (b) irreversible spectrum changes resulting from heating the lignite coal sample sequentially from 25 °C to each of the designated step temperatures. 144

Figure 4.21: Infrared band areas for the 2000–700 cm^{-1} (red) and 3600–2000 cm^{-1} (blue) ranges plotted as a function of lignite coal step temperature. 145

Figure 4.22: Normalized infrared spectrum intensities at 2850 cm^{-1} (red) and 2925 cm^{-1} (blue) as a function of lignite coal step temperature. Triangles represent intensities in spectra measured at the step temperatures and squares represent intensities in spectra obtained after subsequently cooling to 25 °C. 146

Figure 4.23: (a) Infrared spectra of bituminous coal obtained at 25 °C (blue) and 150 (red) °C. (b) Reversible (blue) and irreversible (red) spectrum changes resulting from heating bituminous coal from 25 to 150 °C. 148

Figure 4.24: Bituminous coal 3690 cm^{-1} band maximum variations in spectra obtained at each step temperature (triangles) and after cooling to 25 °C (squares). 149

Figure 4.25: Incremental (a) reversible and (b) irreversible spectrum changes resulting from heating the bituminous coal sample to each step temperature. 151

Chapter 1: Introduction

1.1 Spectroscopy

Spectroscopy is a field of study that measures and explains the electromagnetic spectrum. Applied spectroscopy is the study of materials and how they interact with precise wavelengths on the electromagnetic spectrum. All spectroscopic methods are possible due to measurable interactions of electromagnetic radiation (EM) with matter. EM radiation can induce energy transitions in an analyte. The energy absorbed can excite matter from the ground state to an excited state and the energy released when excited states return to the ground state is unique to specific atom or molecular orbitals, making spectroscopy a powerful investigative tool. Spectrochemical analyses provide both qualitative and quantitative information. In modern spectroscopy, a spectrum consists of a plot of absorbance, transmittance, or radiation intensity as a function of some measure of photon energy.[1]

1.1.1 Origins

The word spectrum was first applied to describe crude spectra of sunlight observed by Isaac Newton in 1672. He demonstrated that visible light consists of a collection of radiation with colors that can be viewed by passing it through a prism. Newton's experimental setup can be seen in the schematic in Figure 1.1.[2 3]

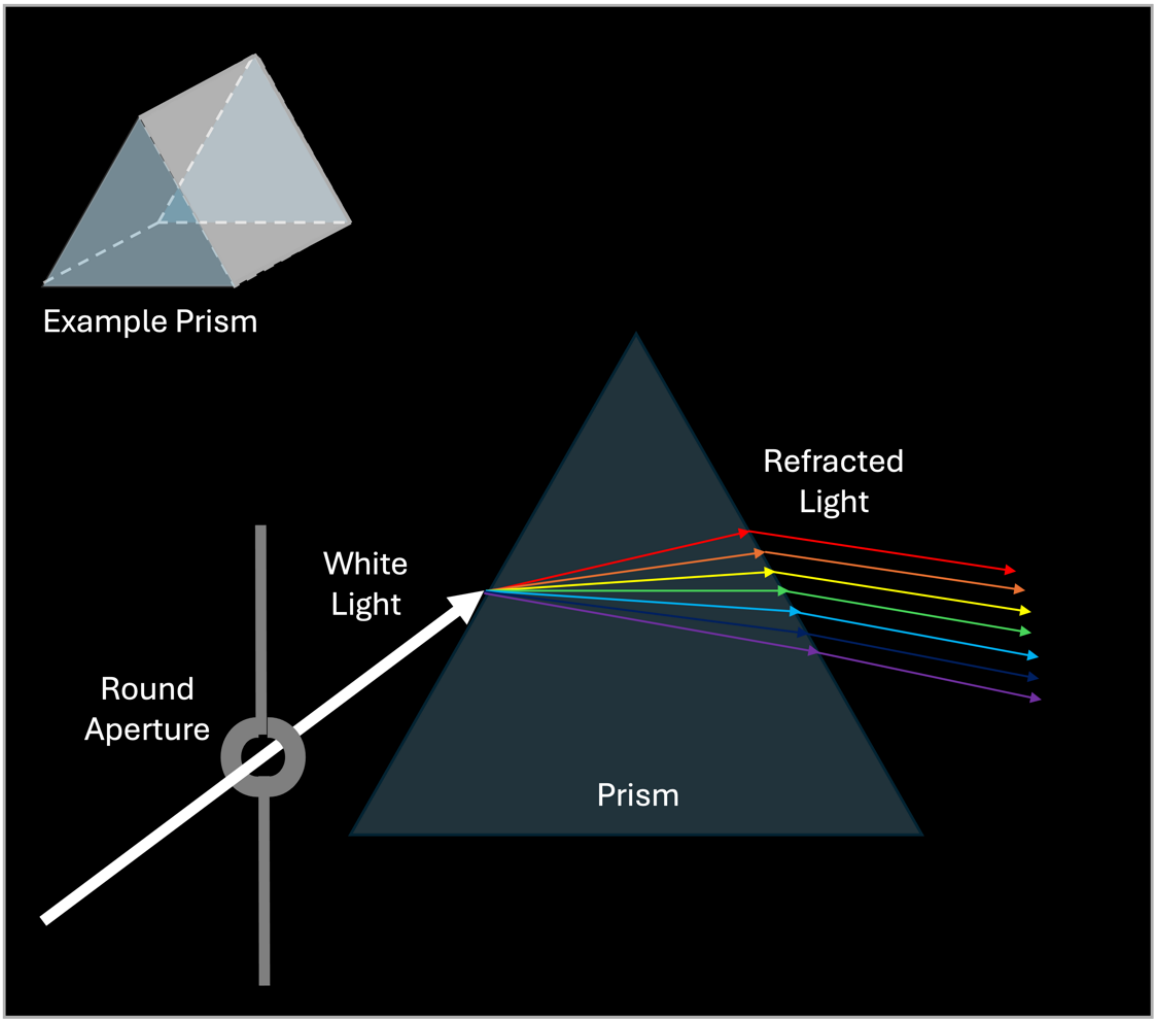

Figure 1.1: Schematic of Isaac Newton's prism experiment demonstrating the refraction and dispersion of white light into seven colors. Wavelength ranges of visible light consist of: Red (750-625 nm), Orange (625-590 nm), Yellow (590-565 nm), Green (565-500 nm), Blue (500-485 nm), Indigo (485-450nm), Violet (450-380 nm).

W. Herschel and J.W. Ritter showed that radiation outside the visible light wavelength region existed with the discovery of the infrared and ultraviolet ranges in 1800 and 1801 respectively. Further advances were made by W. H. Wollaston in 1802 and Joseph Fraunhofer in 1814 when they employed a slit aperture rather than a pinhole and observed the first spectral absorption lines known as Fraunhofer lines. These lines appear as dark lines in the fully dispersed solar spectrum due to absorption by gases in the atmosphere and the outer photosphere of the sun at characteristic wavelengths as seen in Figure 1.2. Fraunhofer is also credited with the invention of the transmission diffraction grating, an optical grating that disperses the electromagnetic spectrum into its wavelengths via diffraction. Building on W. H. F. Talbot's 1826 observation that different salts produced different colors when burned, G. R. Kirchoff and R. Bunsen made significant leaps forward with their 1859 finding that each element has unique spectral lines.[3] This breakthrough laid the groundwork for application of spectrochemical methods for atomic and molecular identification and quantification. Spectrochemical analyses are now applied at both a macro and micro level across multiple fields including chemistry, materials science, astronomy, biology, medicine, and physics.

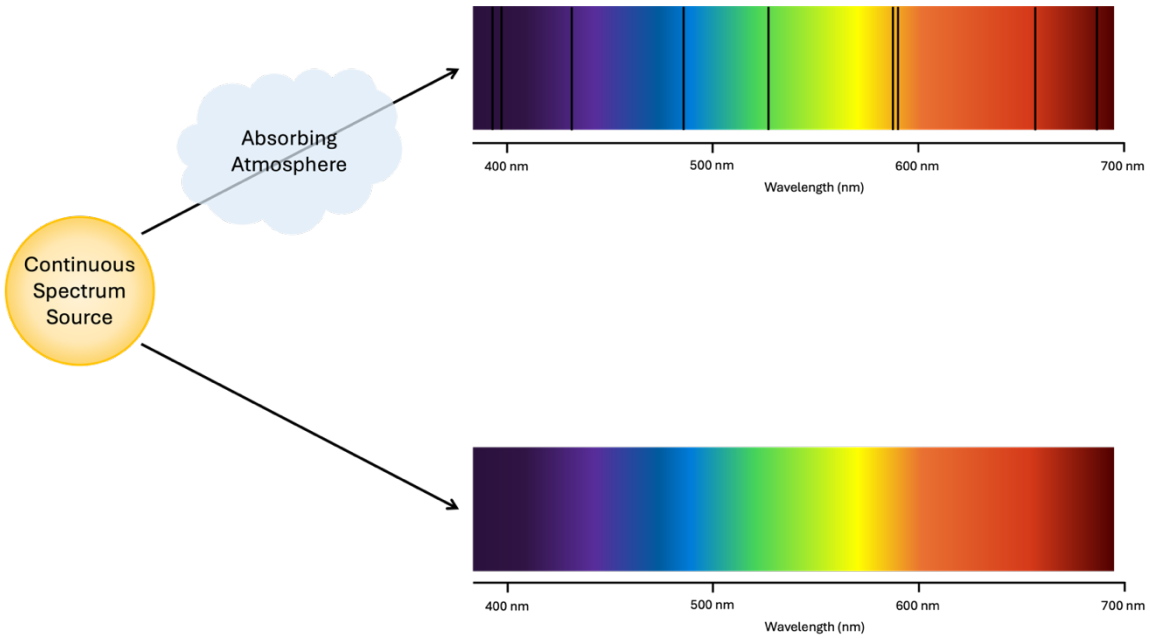

Figure 1.2: The sun produces a continuous spectrum(bottom). Fraunhofer lines are the names of dark lines appearing in the fully dispersed solar spectrum (top) due to absorption by gases in the atmosphere and outer photosphere of the sun.

1.1.2 Working Principle

Spectroscopy functions on two underlying principles. First, that at a quantum mechanical level, atoms naturally exist in a ground state and molecules exhibit zero-point energy at absolute zero. In the ground state, all electrons reside in their lowest energy orbitals. Zero-point energy is the minimum vibrational energy of chemical bonds at absolute zero. A second principle of spectroscopy states that atomic and molecular analytes can transition from their ground states to excited states by external perturbations via applications of energy due to heat, radiation, and chemical reactions. The analyte absorbs some of the applied

energy, temporarily exists in an excited state, and then returns to its ground state, possibly emitting a characteristic radiative energy profile in the process. Spectrochemical information can be obtained by measuring the energy absorbed or emitted by the chemical species of interest. Qualitative spectroscopic data can be used for analyte identification, whereas quantitative spectrochemical analysis is used to determine analyte concentration.

Spectroscopy applications are typically categorized as atomic and molecular. Both methods measure the interactions of electromagnetic radiation and matter. Atomic spectroscopy involves the study of free atomic species and can be used to determine elemental compositions. Molecular spectroscopy provides information regarding electronic energy states and atom-atom vibrations, which depend on bond strengths, lengths, and angles.

Interactions between EM radiation and matter can be influenced by the bulk properties of the matter being studied. A “bulk property” is a unique material characteristic such as density, refractive index, luster, hardness, particle size, opacity, and other things that influence how light interacts with a given sample (i.e. whether light is transmitted, absorbed, reflected, diffracted, etc.) Radiation-matter interactions are further complicated by the fact that electromagnetic radiation has both particle and wave properties. For example, the energy of a photon can be described as both a discreet quantity and a particular wavelength using Planck’s equation (Equation 1.1), which shows the mathematical relationship between

energy and wavelength. In Planck's equation, E is energy in joules (J), h is Planck's constant ($6.63 * 10^{-34}\ J\ s$), c is the speed of light ($3.00 * 10^{8}\ m\ s^{-1}$), λ is the wavelength (m), and f is frequency (Hz).

$$E = \frac{hc}{\lambda} = hf$$

Equation 1.1: Planck's Equation

Electromagnetic radiation spans a wide range of wavelengths which are artificially divided into seven distinct regions: radio waves, microwaves, infrared radiation, visible light, ultra-violet light, x-rays, and gamma rays. These regions (Figure 1.3) are delineated based on how their wavelengths and frequencies interact with matter.

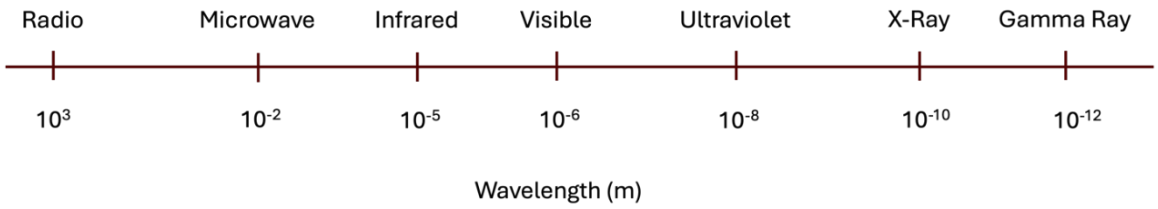

Figure 1.3: Electromagnetic spectrum in wavelength.

The wavelengths included in these regions correlate with the energy transitions that they induce in atoms and molecules. For example, radio waves may induce rotational transitions in the gas phase, infrared radiation can excite

molecular vibrations and rotations (Figure 1.4), and ultraviolet light can induce transitions of valence and middle shell electrons (Figure 1.5).

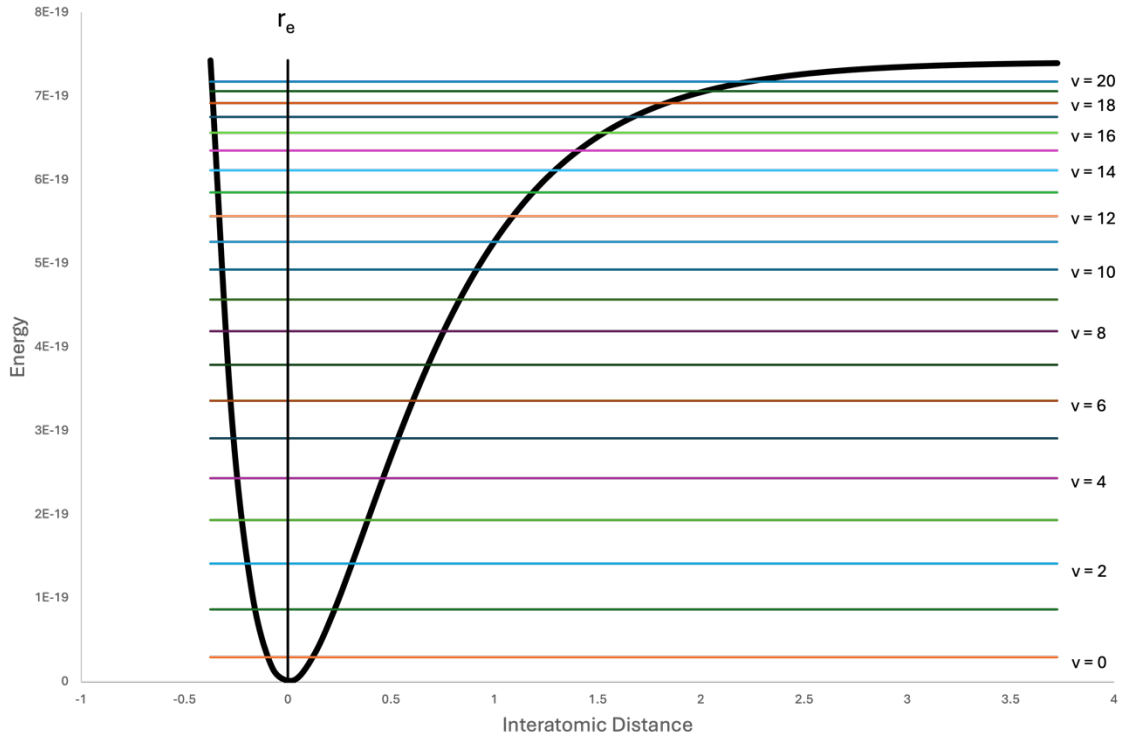

Figure 1.4: Morse potential energy curve showing the vibrational levels for a given electronic state of a diatomic molecule. Rotational levels are between discreet vibrational levels. Vibrational and rotational transitions can be observed by using infrared (IR) spectroscopy.

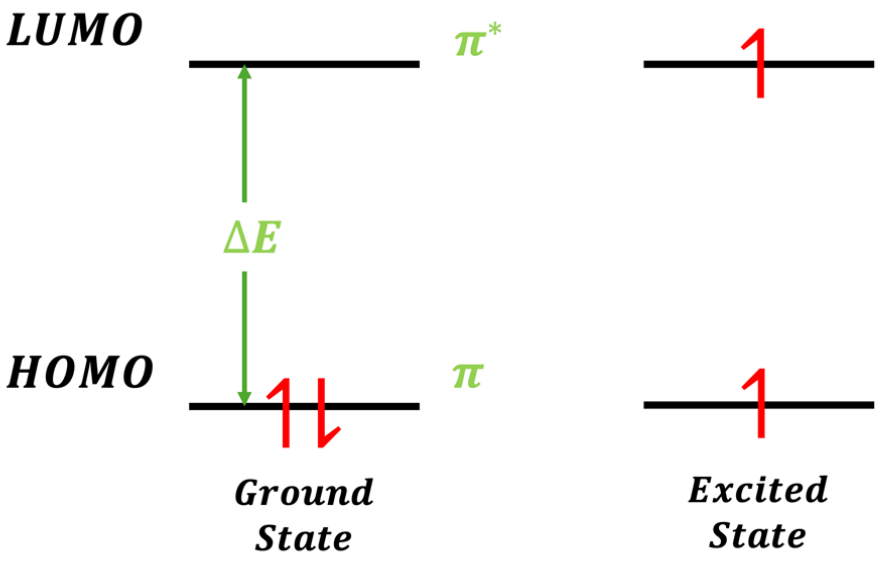

Figure 1.5: Representation of a theoretical HOMO – LUMO transition in UV spectroscopy.

Infrared spectroscopic studies are particularly powerful because, with the exception of homonuclear diatomics, the majority of molecular species are IR active. Spectrochemical information obtained in the infrared region can be used to identify absorbance bands associated with specific functional groups, enabling molecular structure identifications. Indeed, infrared spectroscopy is widely applicable and has been used to investigate samples from different matrices, including environmental[4-17], biological[18-19], regulatory[20-24], forensics[25], and humanities[26-31] contexts.

1.2 Infrared Spectroscopy

Infrared (IR) spectroscopy is a rapid and non-destructive vibrational spectroscopic method that utilizes the infrared portion of EM radiation. It allows scientists to probe molecular structures via the interactions between infrared radiation and polarizable bonds within matter through absorption, emission, and reflection. There are three processes in which a molecule can absorb radiation and shift between discrete quantized energy states: rotational transitions, vibrational transitions, and electronic transitions. Infrared radiation (10^{13} – 10^{14} Hz) is not energetic enough to bring about electronic transitions, therefore, IR spectroscopy takes advantage of molecular vibration transitions when bonds are exposed to infrared radiation.[32-33] Infrared radiation excites molecular vibrations and rotations as exhibited in the Morse Potential diagram in Figure 1.4. IR spectroscopy is applicable to all molecules that experience a change in dipole moment during a vibration.

The first documented observation of infrared radiation came from an 1800 experiment in which English astronomer William Herschel fortuitously placed a thermometer just outside the red wavelengths of the visible spectrum of diffracted light during an experiment. Unknown to him at the time, the recorded increase in temperature was due to infrared radiation; aptly named “infra” and “red” meaning just below red.[34] It wasn’t until over 100 years later when the discovery and mapping of absorbance bands unique to particular functional groups made infrared

spectroscopy a functional tool for qualitative molecular analysis.[35-36] Using a spectrometer containing a rock salt prism, a galvanometer, and a thermocouple, Coblentz obtained infrared spectra for 135 organic compounds.[35] However, the day long acquisition time, specialized training, and intricate sample preparation requirements made infrared spectroscopy difficult to implement.

The advent of the interferometer, the application of Fourier transformation (FT) to interferograms, and a need for better synthetic rubber characterization methods during the mid 1940s drastically enhanced the popularity of IR and drove the method towards mass commercialization by Beckman and Perkin Elmer over the next three decades.[37-38] Subsequent improvements revolutionized infrared spectroscopy making it faster, cheaper, and more user friendly. When combined with its non-destructive nature, these advancements made FTIR an indispensable vibrational spectroscopy tool throughout the 1960s and 1970s. Although less prevalently used today, FTIR spectroscopy is still used for chemical characterization[39], climate monitoring[40], contaminant tracing[41], “green” materials development[42], forensics[43], planetary modelling[44-47], and materials identification[48].

1.3 IR Active Vibrations

As previously discussed, the infrared region of EM radiation interacts with molecular bonds. To be IR active (i.e. provide an infrared spectrum), there must be a change in the dipole moment during the molecular vibration. A molecular dipole results from electronegativity differences between individual atoms, which

result in a difference in charge densities across the molecule. The relative magnitudes of these differences can be estimated, and dipole moments can be predicted based on electronegativity trends, the orientation of the molecule, and the photon electric vector. Polar molecules, like water, have a permanent dipole and are IR active. Homonuclear diatomic molecules that yield Raman spectra are not IR active because they lack a dipole moment change during vibrations, as demonstrated in Figure 1.6. Although the bonds in homonuclear diatomic molecules stretch, this does not produce a change in dipole moment.[32-33] Thus, only heteronuclear diatomic molecules and asymmetric molecular vibrations in polyatomic molecules are IR active.

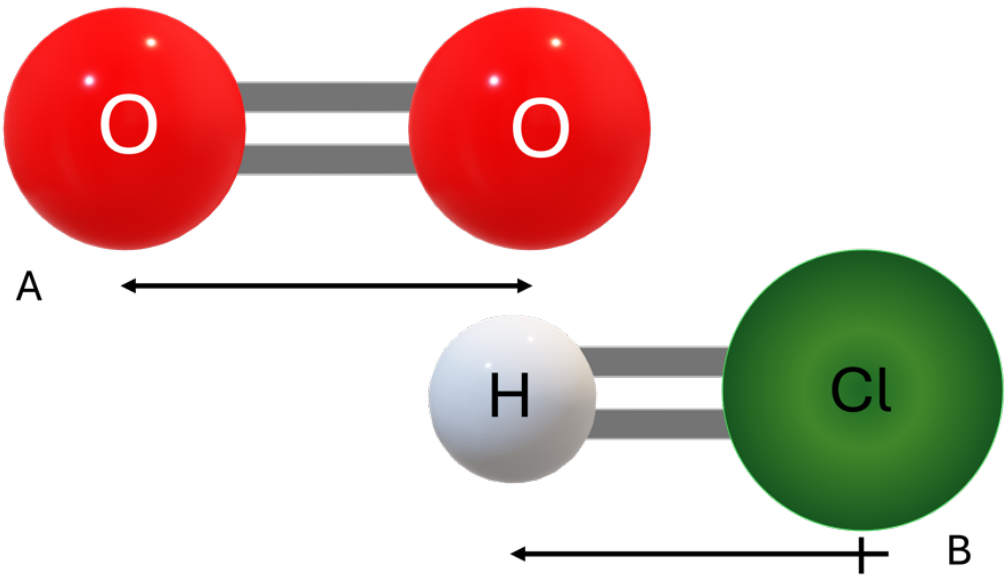

Figure 1.6: The homonuclear diatomic molecule O_2 is not IR active due to its lack of a dipole moment change during stretching. The heteronuclear diatomic molecule HCl is IR active because its dipole moment changes during the stretching vibration.

Characteristic IR spectral bands at unique frequencies often correspond to particular functional groups, which permits the identification of these groups within samples. These bands arise due to the absorption of infrared radiation at resonant frequencies characteristic of the dipole moment rate of change for particular bonds comprising a functional group. The frequencies required to induce dipole changes are characteristic of the vibration absorbing the energy and equal to the "natural vibration frequency". Natural frequencies of bond stretching vibrations can be modeled as simple harmonic oscillations. In this model, the chemical bond between two atoms is represented by a weak spring. Natural vibrational frequencies are calculated by using Equation 1.2.[32-33]

$$v_m = \frac{1}{2\pi}\sqrt{\frac{k}{m}}$$

Equation 1.2: Natural frequency of a harmonic oscillator vibration.

In this equation, v_m represents the natural frequency of the stretching vibration; *k* represents the spring force constant, related to the bond strength; and *m* represents the reduced mass of the two atoms attached by the bond. In a simple diatomic molecule, this is a stretching vibration.[32-33]

There are six distinctive molecular vibration types that can produce dipole moment changes, depending on molecule orientation and connected atom

identities. These motions can be described as: bending, rocking, wagging, twisting, breathing, and stretching. These vibrations fall into two distinct categories: stretching and bending motions. IR stretching modes arise from a constant change in interatomic radii between atoms and can be categorized as either symmetric or asymmetric. IR bending vibrations can be classified as one of four types: in-plane scissoring, in-plane rocking, out-of-plane wagging, and out-of-plane twisting. These motions are illustrated in Figure 1.7.

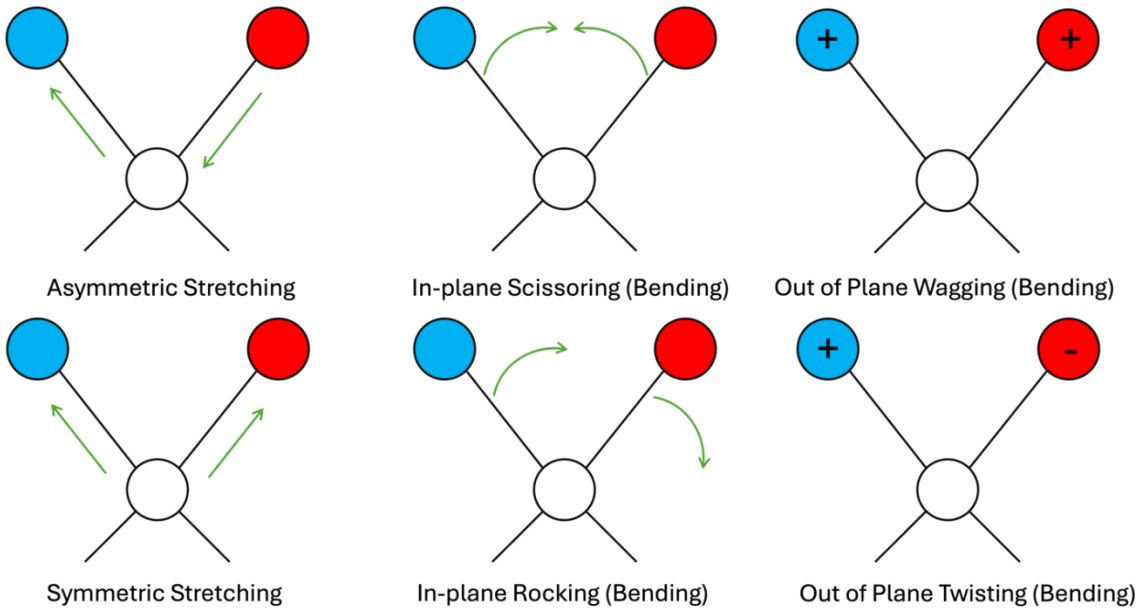

Figure 1.7: Common stretching and bending vibration modes in polyatomic molecules. (+) indicates a motion in front of the plane and (-) indicates a motion behind the plane.

Although molecular vibration information derived from infrared spectra cannot provide an exact structure, the location and relative intensity of bands can

often be attributed to specific functional groups, which provides qualitative structural information. Spectral interpretation is complicated by the fact that some infrared bands that are theoretically active fail to appear in spectra due to several factors (see Table 1.1).[49]

Factors Influencing the Number of Experimental IR Active Normal Modes
1. Molecular Symmetry - Vibrations that don't result in a dipole change will not be IR active. 2. Degeneracy or Near Degeneracy of Vibrational Modes - If the energies of two or more vibrations are identical or nearly identical, several individual vibrations may be represented by a single peak in the IR spectrum. 3. Instrumentally Undetectable Vibrations - If the vibrational intensity (absorbance) is too low, it may be below the detectable range of the instrumentation. - The vibration is outside the frequency range of the instrument.

Table 1.1: Factors Determining the Number of Experimental Vibrational Modes[49]

For example, degeneracy and low absorptivity make the empirical and theoretical infrared spectrum of carbon dioxide different. Carbon dioxide contains two C=O bonds that are polarizable. This molecule experiences asymmetric and symmetric stretching vibrations, although only the asymmetric stretch is IR active.

Because water is a bent molecule, both the asymmetric and symmetric stretches are observed in the IR spectrum. Figure 1.8 shows how the CO_2 and H_2O molecular structures result in different IR activities for their asymmetric and symmetric stretches.

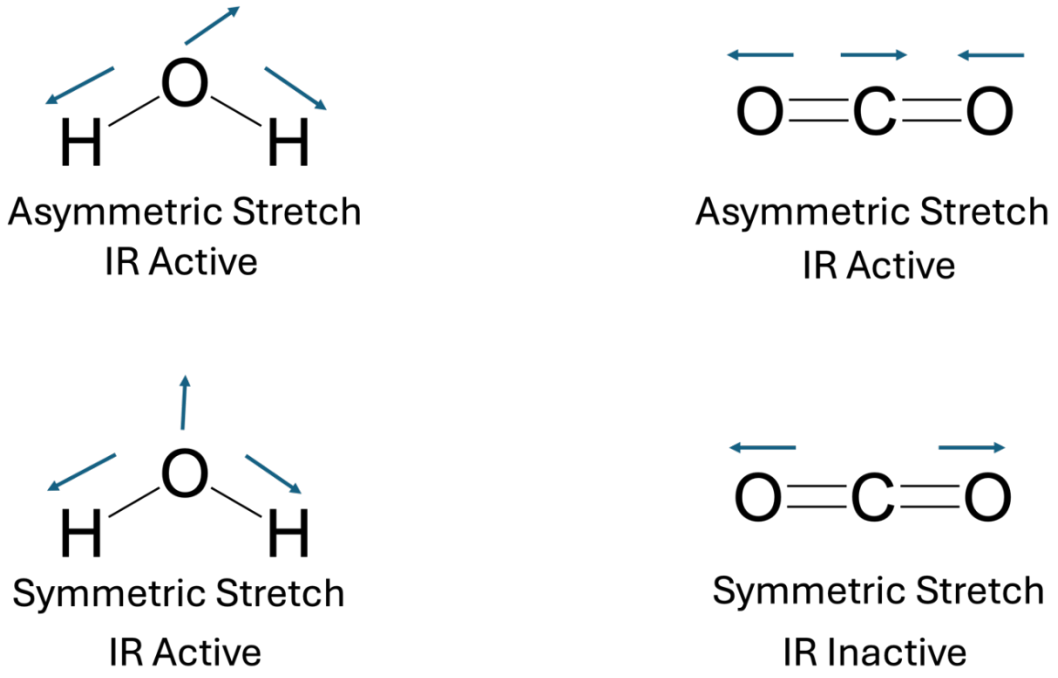

Figure 1.8: Schematic of symmetric and asymmetric stretching vibrations for carbon dioxide (CO_2) and water (H_2O), demonstrating how molecular shape can influence the IR activity of these vibrations.

In polyatomic molecules, the total number of fundamental vibrational modes can be calculated by knowing the molecular formula and if the molecule is linear by using Equation 1.3, where N is the number of atoms in the molecule. There are 3 translational degrees of freedom afforded to single atoms in 3-dimensional

space. Therefore, there are 3N degrees of freedom for a molecule containing N atoms. Larger molecules, therefore, have more possible vibrations. The bonds holding atoms together in a molecule restrict certain degrees of freedom, i.e. motions are translational, rotational, and vibrational. Translational and rotational modes for non-linear molecules are described relative to the x, y, and z axes, leaving 3N-6 vibrational modes. For linear molecules, rotation around the principal symmetry axis produces no change, therefore 3N-5 degrees of freedom are left for vibrational modes. It is important to note, however, that the total number of vibrational modes is not necessarily the same as the total number of IR active modes. In addition to fundamental vibrations, molecular spectra contain weak overtones and combination bands, which are derived from the fundamental vibrations.

$3\mathrm{N}-5$	$3\mathrm{N}-6$
Linear	Nonlinear

Equation 1.3: Equation for the calculation of vibrational modes possible for a molecule.

Infrared spectroscopy is an analysis technique that yields a unique infrared spectrum that depends on molecular structure. The information contained in an infrared spectrum is directly related to the molecular structure and to the localized

environments of the atoms involved in the IR active vibrations. Although absorption frequencies are theoretically predictable based on functional group structure, shifts occur due to interactions between the molecule and its local environment. The magnitudes of these shifts depend on bond strengths, electron density distributions across bonds, and bond angles. Small variations in these factors can lead to different visual spectral outcomes – i.e. broad versus narrow bands, red versus blue shifts, strong versus weak absorbances, et cetera. Local environment perturbations and other factors combine to cause spectral band broadening, vibrational coupling, overtones, combination bands, and difference bands, which significantly distorts measured results from theoretical predictions. Interpretation of infrared spectra can therefore be complex and difficult.

Despite this difficulty, researchers have been successful at applying IR analysis for chemical characterization and quantification. Typically, three divisions are used to describe infrared spectra as a function of wavenumber (i.e. cm^{-1}): near-IR (12,800 – 4000 cm^{-1}), mid-IR (4000 – 200 cm^{-1}), and far-IR (200 – 10 cm^{-1}). Most molecular vibrations occur at frequencies within the mid-IR (MIR) range and techniques tend to be the most user friendly in this region. Therefore, MIR is the most commonly studied infrared region.[49] Additionally, MIR contains the "fingerprint region" which can be used to identify specific molecules. This region not only provides highly characteristic molecular structure information, but also is

uniquely suited for monitoring subtle changes due to external perturbations (i.e. heating, pH, etc.). All studies contained herein were performed in the MIR region.

1.4 IR Spectral Regions

The three infrared subregions (NIR, MIR, and FIR) are delineated from one another based on wavenumber ($\bar{\nu}$), which is the inverse of wavelength (in cm^{-1}) as seen in Equation 1.4.

$$\frac{1}{\lambda} = \bar{\nu} = \frac{E}{hc}$$

Equation 1.4: Wavenumber ($\bar{\nu}$) as it mathematically relates to wavelength (λ), the speed of light (c), Planck's constant (h), and photon energy (E).

The wavelengths designated for each region are named based on their positions relative to the visible spectrum – NIR 12,800-4000 cm^{-1}, MIR 4000-200 cm^{-2}, and FIR 200-10 cm^{-1}. Variations in these wavelength ranges are sometimes specified due to the type of detector used.

NIR Transflectance (Reflection Absorption)

Transflectance utilizes principles of absorption and reflectance spectroscopy by passing incident radiation through a thin sample film applied to a reflective substrate. Incident radiation passes through the sample and reflects to a detector. Differences between incident and detected radiation reveals wavenumbers at which radiation is absorbed by the sample. As shown in Figure

1.9, alteration of the angle of incidence allows for a controllable variable pathlength.

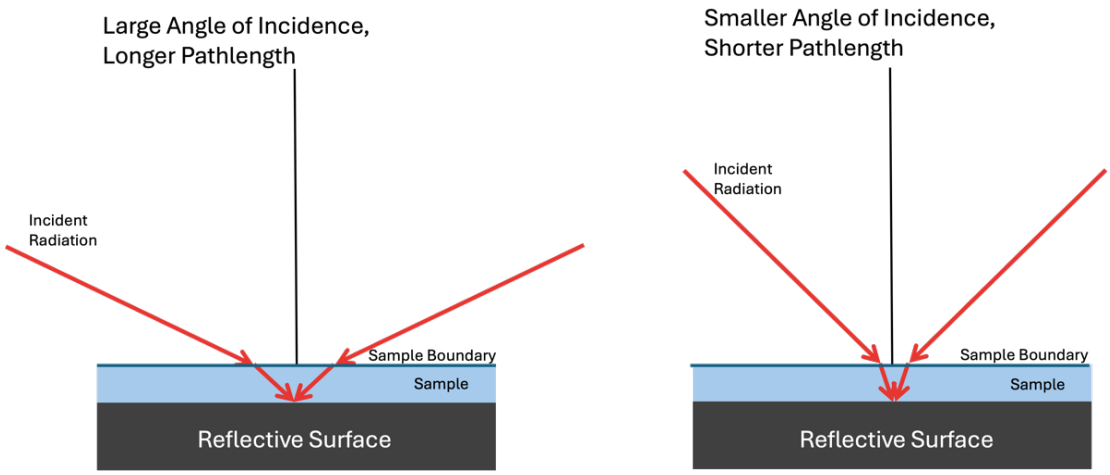

Figure 1.9: Schematic demonstration of how changing the incident angle can alter the pathlength in transflectance IR. Longer pathlengths result from larger incident angles. Shorter pathlengths result from smaller incident angles.

Transflectance is commonly employed in the NIR in various practical applications that involve soil and agricultural science, medicine and biochemistry, and food and drink regulation.[50-53] NIR applications are typically quantitative analyses, whereas MIR applications more often involve qualitative analyses, such as functional group identifications.

1.5 Mid-IR Transmission Spectroscopy

The most commonly utilized MIR methods are transmission, reflectance, and attenuated total reflectance (ATR) spectroscopy. All three methods use the same basic principle to probe the nature of interactions between light and matter

and vast comparative spectral libraries exist for these methods. Transmittance and reflectance differ based on the angles at which incident radiation strike the sample.

In both transmission and ATR spectroscopy, radiation passes through the sample to some degree before reaching the detector whereas radiation reflects from the sample surface in reflectance spectroscopy. Due to these different requirements, different optical systems and sample preparation methods are required for each method.

In Transmission-IR, infrared radiation passes completely through the sample. It can be absorbed completely or partially. It can also be reflected and therefore not detected (Figure 1.10).

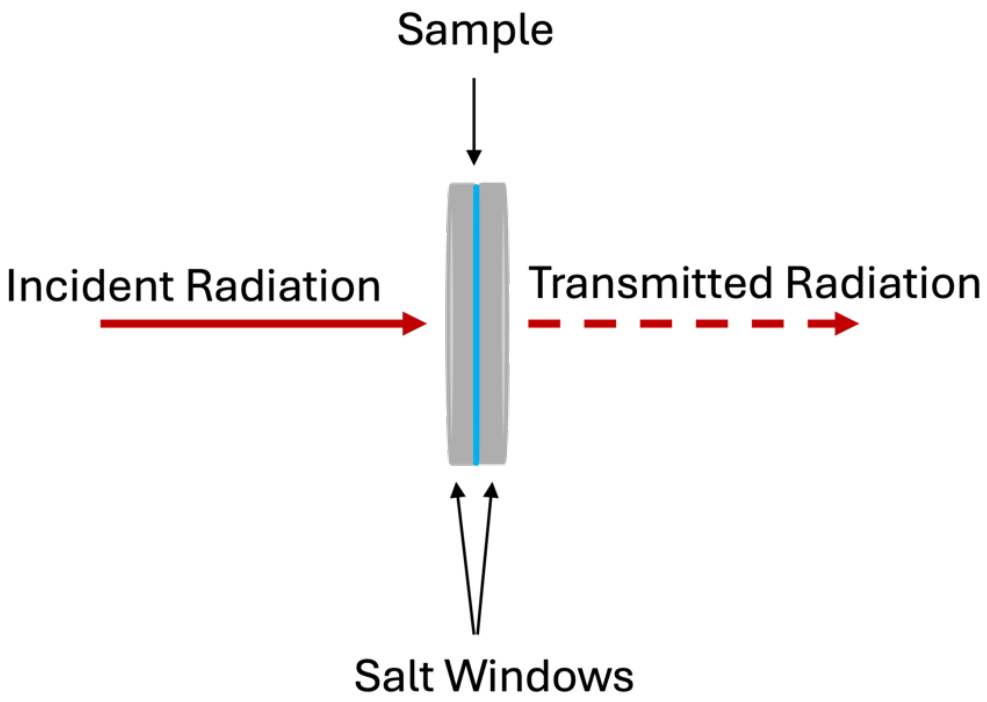

Figure 1.10: Schematic of a transmission IR liquid sample cell.

When incident radiation is either totally absorbed or reflected, no radiation reaches the detector, and no molecular structure information is obtained. Radiation reaching the detector is attenuated at wavenumbers where the sample absorbs. This allows for both qualitative characterization and quantitative description of samples because Transmission-IR absorbances typically obey the Beer-Lambert Law, which states that the absorbance of incident radiation, when passed through a fixed pathlength cell, is directly proportional to the concentration of the substance, the molar absorptivity, and the absorption path length. These relationships are formally presented by the Beer's Law Equation 1.5 below, where A is absorbance, ε is molar absorptivity, b is pathlength, and c is concentration.

$$A=\varepsilon bc$$

Equation 1.5: Beer's Law shows that Absorbance (A) is directly proportional to the molar absorptivity (ε), pathlength (b), and concentration (c).

The sample handling methods required for transmission IR spectroscopy utilize infrared transparent windows. These salt windows must be kept free of contamination and perfectly flat with no fogging. Any topographical variation or fogging in the surfaces of salt windows can produce spectral artifacts. Common IR transparent salt window materials, like KBr, cannot be used with aqueous samples.

Transmission spectra are typically reported in percent transmittance as a function of wavenumber. Due to the high molar absorptivities of most samples,

neat samples cannot be used for transmission spectroscopy and sample dilution is required. Thick layers and neat samples are usually not appropriate for transmission spectroscopy due to complete absorption of radiation, which results in the “bottoming out” of spectral features. To avoid loss of peak shape information, solid samples are typically ground to homogenous small particles and mixed in low concentrations ranging from 0.2% to 1.0% with an IR transparent salt such as KBr and then pressed into a pellet. Solid samples may also be prepared as Nujol mulls in which a finely ground (typically 1-2 micron particles) solid is mixed with mineral oil and placed between two IR transparent windows. Liquid samples are commonly analyzed by placing them between two IR transparent salt (i.e. KBr) windows for non-water containing samples and zinc selenide windows for water containing samples. Infrared radiation can then be passed through the sample with the pathlength determined by the thickness of spacers placed between the windows. Gas samples are handled in a similar manner. Samples are enclosed in a long cylinder with IR transparent windows on both ends. Gases are less dense than liquids, therefore, longer pathlengths can be employed.

1.6 Mid-IR Reflectance Spectroscopy

Unlike transmittance infrared spectroscopy and as the name would indicate, infrared radiation reflects from the sample in reflectance infrared spectroscopy. Reflectance-IR spectral features result from interactions of incident radiation with the sample, which can be categorized into three types: specular reflectance,

diffuse reflectance, and attenuated total reflection (ATR). Figure 1.11 illustrates the spatial and angular differences between these three reflectance types.

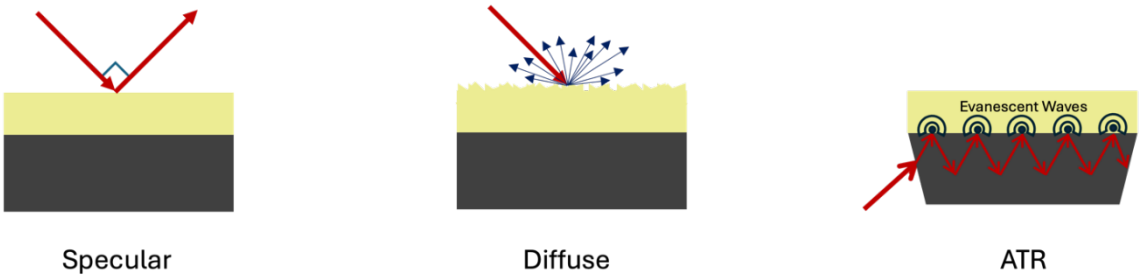

Figure 1.11: Specular reflectance IR measures radiation reflected from the sample at the same angle as the incident angle. Diffuse reflectance IR measures radiation reflecting at all angles except for the specular angle. ATR-IR detects the radiation reaching the detector after it has passed through the ATR crystal and has been attenuated by evanescent wave interactions with the sample at the sample-crystal interface.

1.6.1 Specular Reflectance

Specular reflectance methods detect radiation reflected from the sample at the same angle as the angle of incidence. Specular reflection measurements are commonly used to measure the thickness of coatings on smooth, reflective surfaces for samples such as: polymers, art, and metallic solids.[54-57] It can also be applied to studies of reflective materials such as glass, ceramic coatings, and certain minerals.[58-62]

When performed on these samples with a nearly horizontal angle of incidence (i.e. ~90°), specular reflectance infrared spectra are vastly different from absorbance spectra. In order to obtain spectra comparable to absorbance measurements, specular reflectance data must be converted by using a Kramers-Kronig Transformation (KKT).[63-64]

1.6.2 Attenuated Total Reflectance

Attenuated Total Reflectance infrared spectroscopy is one of the most commonly used IR techniques today due to its user friendliness, applicability to neat (i.e. undiluted) samples, and non-destructive nature. With the ATR approach, radiation reflected through a crystal with a high refractive index penetrates slightly into a sample with lower refractive index placed at the crystal surface. At certain incident angles, nearly all the light is reflected back into the crystal at the crystal/sample interface, yielding near total internal reflection. Upon reflection, an evanescent wave that extends just beyond the crystal surface interacts with a thin layer of the sample, which is in direct contact with the crystal.[65] The sample absorbs some of the evanescent wave, which decreases (attenuates) the intensity of the radiation reflected back into the crystal. The ratio of the signal detected with a sample present to that obtained prior to adding the sample results in the infrared spectrum of the material placed on the crystal surface. ATR can be used for analysis of organic and inorganic solid and liquid samples.[66-70]

Although widely used, ATR-IR suffers from a few significant pitfalls. Evanescent wave sample penetration distances are wavenumber-dependent, making attempts at direct comparison with transmission cell measurements problematic. Small variations in peak intensity and band location shifts occur due to the amount of reflected radiation in ATR-IR versus Transmission-IR. Furthermore, evanescent waves penetrate only a few micrometers into the sample, thus peaks with high molar absorptivity are easily detected whereas those with lower absorptivity are not readily apparent in spectra. Finally, ATR crystals must be meticulously cleaned to avoid scratches and a flat and even crystal surface must be maintained to ensure good contact with samples during analyses.

1.6.3 Diffuse Reflectance

Diffuse reflectance infrared Fourier transform spectroscopy (DRIFTS) measures radiation reflected at all angles except the incident angle, i.e. all non-specular reflected radiation. DRIFTS is applicable to samples containing rough surfaces or irregularly shaped particles, which preferentially scatter radiation in all directions. One advantage of DRIFTS over transmittance spectroscopy is that it requires significantly less sample preparation and allows the application of infrared spectroscopy to neat powders and rough surface samples.[71]

Due to the inhomogeneous nature of samples with irregular surfaces like powders, diffuse reflectance spectra depend on interactions between the sample and infrared radiation and also the light scattering properties of the sample.[72] Thus,

spectra are heavily dependent upon factors such as sample refractive index, particle or sample layer size, particle size distributions, sample homogeneity, and particle packing. Despite paying close attention to those factors during sample preparation, diffuse reflectance spectra may appear different than traditional transmission IR spectra. Low intensity bands are often larger, whereas high intensity bands may appear broadened or rounded.[71]

Many theories have been posited to describe and account for the spectral effects of the complex combination of absorbance and scattering in DRIFTS measurements. The mostly widely accepted mathematical model for DRIFTS is the Kubelka-Munk (KM) Optical Theory.[73-74] This theory, which lends its name to the Kubelka-Munk intensity units commonly found on DRIFTS spectra, approximates the relationship between sample concentration and reflection properties by ratioing a single beam spectrum of a KBr diluted sample to the spectrum obtained for pure KBr.

The Kubelka-Munk Optical Theory model was originally developed for the analysis of paint films.[75] This theory relies on several assumptions including, but not limited to: the sample is contained within a layer of infinite length and width, particle size is significantly smaller than sample thickness, incident radiation is applied diffusely and homogenously across the sample surface, light only interacts with the sample surface via scattering and absorption, the sample layer is isotropic and homogenous, the sample contains small optical heterogeneities, no external

or internal surface reflection occurs, and that the scattering coefficient and absorption coefficient of a given sample remain constant regardless of layer thickness.[76] The Kubelka-Munk function that was derived by Paul Kubelka and Franz Munk is given by Equation 1.6. It consists of a two factor transformation that accounts for incident and reflected radiation (R_∞) and takes into account absorption and scattering coefficients.[75] The calculation is performed for reflectance intensities at each wavenumber and allows the absorption (K) and scattering (s) characteristics of the sample to be obtained from DRIFTS measurements.

$$f(R_\infty) = \frac{(1 - R_\infty)^2}{2R_\infty} = \frac{K}{s} = \frac{C}{k}$$

K: Absorption coefficient of the sample material

s: Scattering coefficient of the sample material

R_∞: reflectance of a sufficiently thick sample

C: sample concentration

k: derived constant, k=s/2.303ε

Equation 1.6: Kubelka-Munk transformation equation.

The Kubelka-Munk equation assumes a semi-infinite sample consisting of infinitesimally thin layers of particles and that the scattering coefficient, *s,* can sufficiently account for light propagation throughout the sample (i.e. multiple

internal scatterings at particle boundaries). This semi-empirical value is largely dependent upon particle size and sample refractive index and is regarded as a constant in the Kubelka-Munk function. Treating the scattering coefficient as a constant yields a linear relationship between K and the maximum $f(R_\infty)$ value for any given peak. In reality, the scattering constant changes with sample particle size and packing density, therefore care must be taken when loading samples to consistently achieve reproducible results.[75, 77] The ratio of the absorption coefficient (K) to the scattering coefficient therefore can be represented as a function of sample reflectance (R) from the semi-infinite layer. Assuming proper sample handling, the K/s ratio should be linearly related to concentration.[71, 78] Essentially, as sample concentration increases and therefore radiation absorption increases, the K/s ratio also increases.

Clearly demonstrated by the equation, the Kubelka-Munk theory results in a higher sensitivity for discrimination of weak absorbers as the *K/s* ratio approaches zero. This theory is less accurate when applied to high absorbing chemical species.[79] This results in slight but notable differences between reflectance IR spectra that have undergone Kubelka-Munk transformations and traditional absorbance spectra. Low intensity bands representing weakly absorbing species will be larger in KM reflectance spectra. Peaks resulting from highly absorbing species, (i.e. strong intensity bands), will be broader and rounder than their proxies in transmission IR absorbance spectra.[71] These variations can

generally be mitigated via proper sample handling and by using IR software processing packages. The button-IR results presented in subsequent chapters also offers a way to mitigate these peak deforming effects.

Despite the abundance of assumptions required for the Kubelka-Munk theory and the relative complexity of sample handling, it has been successfully applied in numerous studies and is the most accepted model for approximating Beer's law-like calibration curve linearities with concentrations when employing MIR diffuse reflectance spectroscopy.[7, 16, 77, 80-81]

1.6.4 Variable Temperature Diffuse Reflectance Infrared Fourier Transform Spectroscopy

Variable Temperature Diffuse Reflectance Infrared Fourier Spectroscopy, or VT-DRIFTS, is a specialized reflectance spectroscopic method allowing for real-time monitoring and characterization of temperature induced reactions and structural changes. This technique has been employed in water desorption studies, soil adsorbate and transport studies, to study clay desorption mechanisms, for chemical reaction activation energy determinations, and for numerous mineralogical characterizations.[7-8, 16, 82-92] The working principle of VT-DRIFTS is the same as that of DRIFTS, except that real time changes in the sample are monitored as it undergoes thermal perturbations. The use of specific heating and cooling profiles will be discussed in detail in later sections.

1.7 Hyphenated Systems

Infrared spectroscopy can also be coupled with other analytical systems. Hyphenated analyses allow for additional questions to be asked and answered. For instance, when coupled with thermogravimetric analysis, TGA-IR has been used to characterize the volatile components evolved from a sample during heating.[93-94] Various infrared spectroscopic methods can also be used to qualitatively characterize or quantify components separated via gas and liquid chromatography.[95-99]

These hyphenated systems are used across multiple industrial, academic, and government sectors. No infrared spectroscopic method is so widely used, however, as attenuated total reflectance, largely due to its convenient minimal sample preparation requirements. Despite the abundance of infrared spectroscopic techniques, hyphenated methods, and an ongoing pursuit of novel IR approaches, the introduction of widely applicable sampling methods for routine analyses of liquid, solid, grease, and paste samples has been relatively stagnant since the advent of ATR.[65, 100] That is, until the introduction of a novel sampling technique known as Button-IR.

The Button-IR method presented here is a novel approach to IR sampling. It offers distinct advantages: the sample holder is economical and relatively easy to manufacture, can quickly be adapted for existing IR instruments, is reusable with minimal cleaning, is durable through repeated severe measurement

conditions, is user friendly, and introduces opportunities for neat analysis of samples previously not possible in infrared studies. Case studies presented in this dissertation seek to further elucidate the working principle of the Button-IR approach, demonstrate its ability to get high quality data quicker, and present avenues for use within other fields of study. Additionally, the uniquely suited utility of button sample holders for VT-DRIFTS and mineralogical studies will be highlighted.

Chapter 2: Button-IR Design, Working Principle, and Sampling Considerations

2.1 Introduction

Attenuated Total Reflectance (ATR) is currently the preferred infrared spectroscopic method for analyses of neat samples due to its user friendliness, minimal sample preparation requirement, and quick analysis times.[101-102] Spectral quality, however, is heavily dependent upon sufficient contact between the sample and the ATR crystal. Moreover, due to the wavelength dependent nature of radiation penetration into ATR-IR samples, spectra are not readily comparable to transmission measurements. Another commonly employed infrared technique for scattering samples, DRIFTS, requires sample dilution with non-absorbing diluents to avoid bottoming out of peaks and the appearance of other spectral distortions. This largely prevents neat sample and/or non-scattering sample analysis with this technique. Button-IR offers a solution to some of these pitfalls.

Button-IR, aptly named for the novel sample holder's button-like appearance, utilizes a new sampling accessory for a novel methodological approach to MIR spectroscopic studies. A button consists of a polished stainless-steel backing with a small diameter circle of varying sized wire mesh spot welded to its center. Wire meshes were obtained from TWP Inc. (Berkeley, California). The wire mesh and stainless-steel backing both serve as reflective surfaces and

radiation diffusers, scattering the light over a wide angular distribution, thus diffuse reflection optics are the most suited to collect data. The intensity of the diffused radiation from a button without sample sufficiently provides a single beam spectrum background, therefore eliminating the necessity of non-IR active reference materials such as KBr. Additionally, the reflective nature of the steel mesh and metal backing scatters the infrared beam, sufficiently propagating the radiation throughout inherently low-scattering samples. This means that when samples that have inherently poor scattering properties, such as liquids and greases, are loaded into a button sample holder as a thin layer, diffuse reflection spectra can be obtained due to the scattering provided by the button sample holder itself.[103]

2.1.1 Instrumentation

Infrared spectroscopic measurements described in this dissertation were obtained by using a Mattson Instruments Inc. (Madison, WI) Nova Cygni 120 Fourier transform infrared spectrophotometer (FTIR) with an “Infrared Associates, Inc.” (Cranbury, NJ) Mercury cadmium telluride (MCT) photoconductivity detector. Various detectors are available for FTIR spectroscopy. The MCT detector offers the distinct advantage of high sensitivity due to its high quantum efficiency (ratio of incident photons to converted photons in the conduction band). This was advantageous for VT-DRIFTS studies, where radiation intensity at the detector may be low. MCT detectors must be cryogenically cooled prior to use and have a

detection range spanning most of the MIR spectral region.[104] The studies described here employed a liquid nitrogen cooled detector, which was allowed to settle at 77 K over the course of an hour prior to collecting spectra.

A Harrick Scientific Inc. (Pleasantville, NY) praying mantis diffuse reflection accessory was used for all DRIFTS studies described in this dissertation. The Praying Mantis (PM) diffuse reflection optics in Figure 2.1 consist of a compact ellipsoid shaped set of aluminum coated mirrors that readily fit into most commercial instruments.[105] One of the mirrors focuses radiation on the sample whereas the other mirror collects radiation from the button and the sample. These diffuse reflection optics are specifically oriented to collect as much diffusely scattered radiation as possible while rejecting specular reflectance and thereby providing advantages over the integrating sphere DRIFTS alternative. PM optics provide a small diameter focal point, thus allowing for analysis of samples as small as 3 mm in diameter. They also allow samples to be positioned horizontally rather than vertically, which better facilitates analysis of loose powders, liquids, and pastes. These features were particularly important for analysis of the oil and loose mineral samples described in this dissertation.

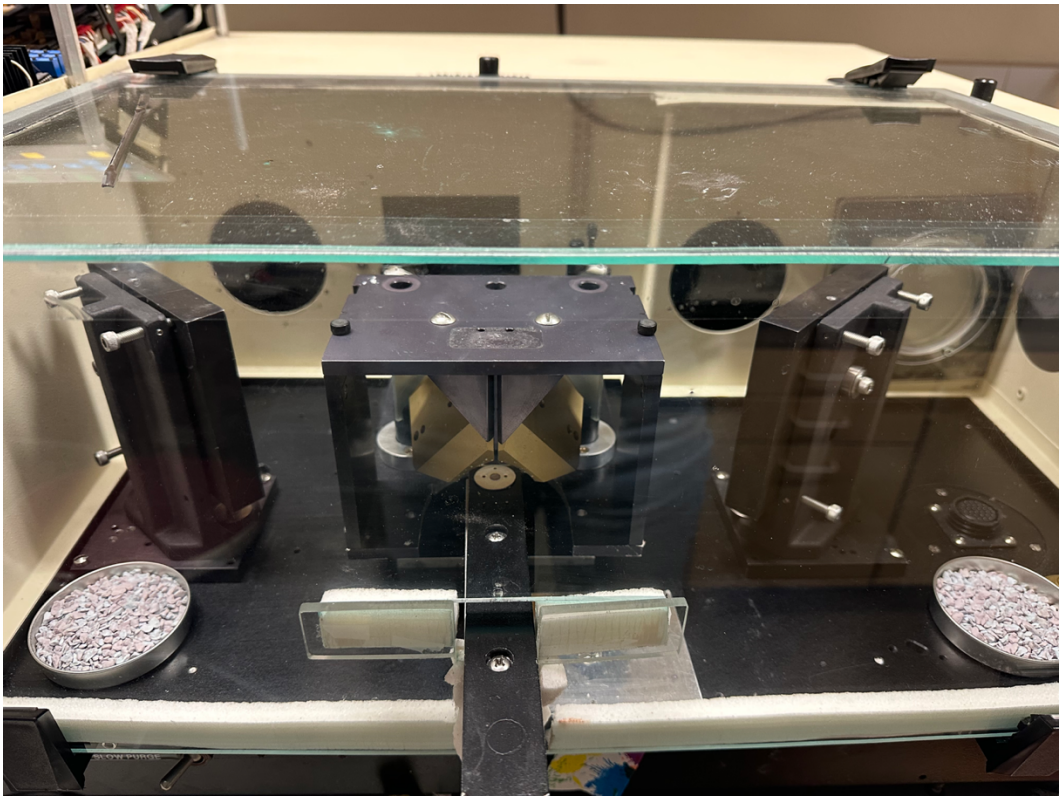

Figure 2.1: Photograph of the Praying Mantis optics. Ellipsoid mirrors are centered over a button sample holder at the end of a sample introduction slide.

2.2 Button Sample Holder

Button sample holders are novel sampling accessories that replace the sample cups used in conventional DRIFTS.

2.2.1 Button Fabrication

Button sample holders (US patent 11,047,796 B2) are fabricated entirely from stainless-steel, making them both durable and easy to clean by using a simple ultrasonic jewelry cleaner and deionized water. The basic construction includes two-components: a 0.75 inch diameter 430 grade stainless-steel disk backing and

a roughly 0.25 inch diameter wire mesh placed at its center. Two models of the button, exposed mesh and recessed mesh versions, offer different sampling properties. As shown in Figure 2.2, the exposed mesh model can have various mesh sizes spot welded to a flat blank whereas the recessed mesh model contains the mesh within a 0.25 inch diameter depression at the center of the backing. The exposed mesh button is useful for abrasion sampling of solids[106], whereas the recessed mesh model provides a reservoir, making it suitable for liquid samples.[107]

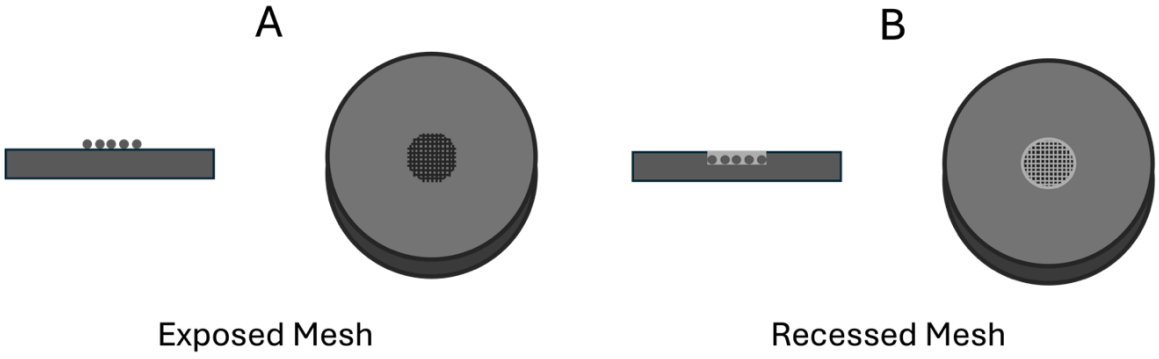

Figure 2.2: Diagrams of the exposed mesh button and the recessed mesh button. The left shows a side view of the exposed mesh button next to a top view. The right shows the same views for a recessed mesh button.

In addition to the exposed and recessed options, incorporating meshes with various wire diameters and weave patterns makes buttons customizable. Based on different available wire diameters, cavity sizes, and weave patterns, some meshes may be better suited for certain sample types than others. As listed in Table 2.1, the 50, 100, and 200 meshes all have plain weave square patterns and

are suitable for solids. The 635 and 2800 meshes with twill and sintered weaves respectively are preferred for low viscosity liquids. The numeric mesh size designation indicates the number of openings per inch.

Mesh (voids/in)	**Wire Diameter**	**Cavity Size**	**Mesh Weave**	**Preferred Samples**
50	0.0090 in 0.2286 mm	0.0110 in 0.2794 mm 279 microns	Plain Weave Square	Solids
100	0.0045 in 0.1143 mm	0.0055 in 0.14 mm 140 microns	Plain Weave Square	Solids
200	0.0016 in 0.04064 mm	0.0034 in 0.08636 mm 86 microns	Plain Weave Square	Solids
635	0.0008 in 0.02032 mm	0.0008 in 0.02032 mm 20 microns	Twill Weave	Liquid
400x 2800	0.0012 in 0.03 mm and 0.00078 in 0.02 mm	1 micron	Sintered	Liquid

Table 2.1: Listing of mesh sizes with wire diameter, cavity size, weave type, and the preferred sample type that each mesh is best suited for.

Mesh wires also allow for particle size selection based on the mesh parameters. Figure 2.3 shows five different meshes. Maximum sample thickness is limited to a depth roughly twice the wire diameter, thus thin layers of neat solids can be analyzed.

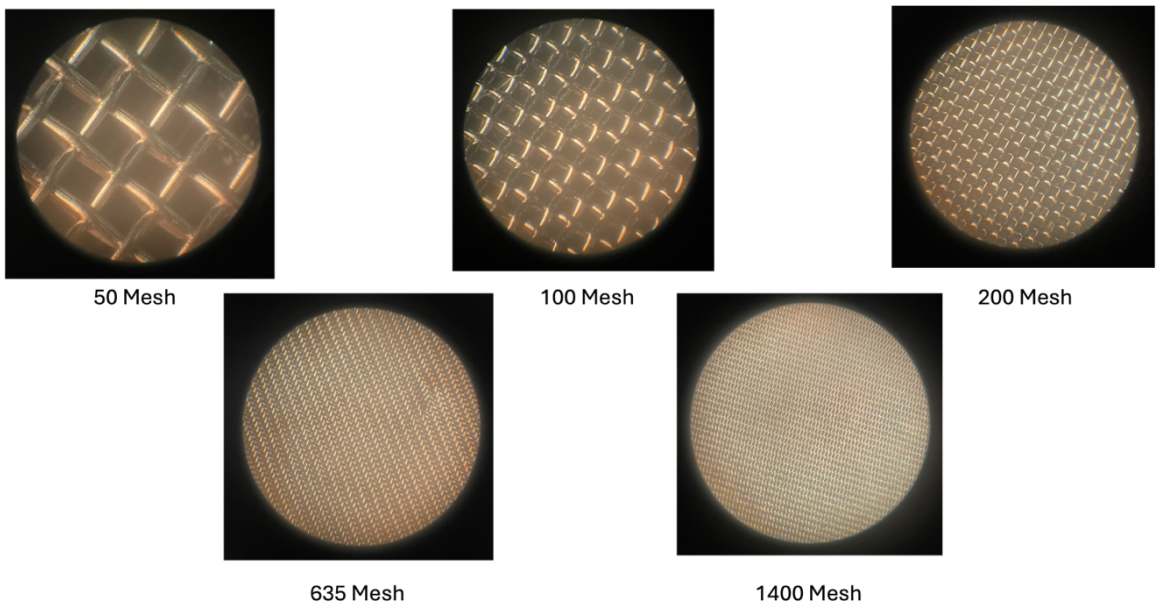

Figure 2.3: Photos of mesh sizes taken under approximately 30X magnification via a microscope (10X) and iPhone zoom (3X) to demonstrate various void sizes and weave patterns.

The small size of button sample holders and customizable design make them an easily adaptable sampling tool. Additionally, voids between mesh wires also serve as tiny wells that efficiently contain sample material, allowing for both stable transport and long-term storage, especially for solid samples.

2.2.2 Button IR Sample Introduction Slides

Three sample introduction slides were designed to reproducibly place the button sample holder at the infrared beam focus of the PM optical system. Sample slides could be quickly inserted and removed from the purged sample chamber via a small slit cut into the plexiglass cover. Sample position in the infrared beam could be fine-tuned by turning an adjustable stop (screw) at the back of the slide groove.

One sample slide design held the button firmly in place by using two alignment pins and a neodymium magnet. The button was fixed in a horizontal orientation with respect to the ellipsoid mirrors, allowing collection of diffusely scattered radiation. A second slide employed the same alignment pin and magnet method to fix the button in place, but it was tilted by 31° from horizontal. This slide was used to selectively collect specularly reflected radiation from samples. The third sample introduction slide was designed to hold the button horizontally to collect diffusely scattered radiation, but the button attachment mechanism was able to be rotated. This slide was employed to investigate the effects of changing the orientation of the button wire mesh on diffuse reflectance infrared spectra. Pictures of the fixed and rotatable diffuse reflectance slides are shown in Figure 2.4.

The fixed slide is shown on the left with a button sample holder installed. The rotatable button slide is shown on the right. The rotating platform has two alignment pins and is set on a scale with ten-degree increment markings. The button

alignment mark is typically oriented towards the front end of the fixed slide. When using the rotatable slide, it can be manually aligned in 10° intervals by using the scale.

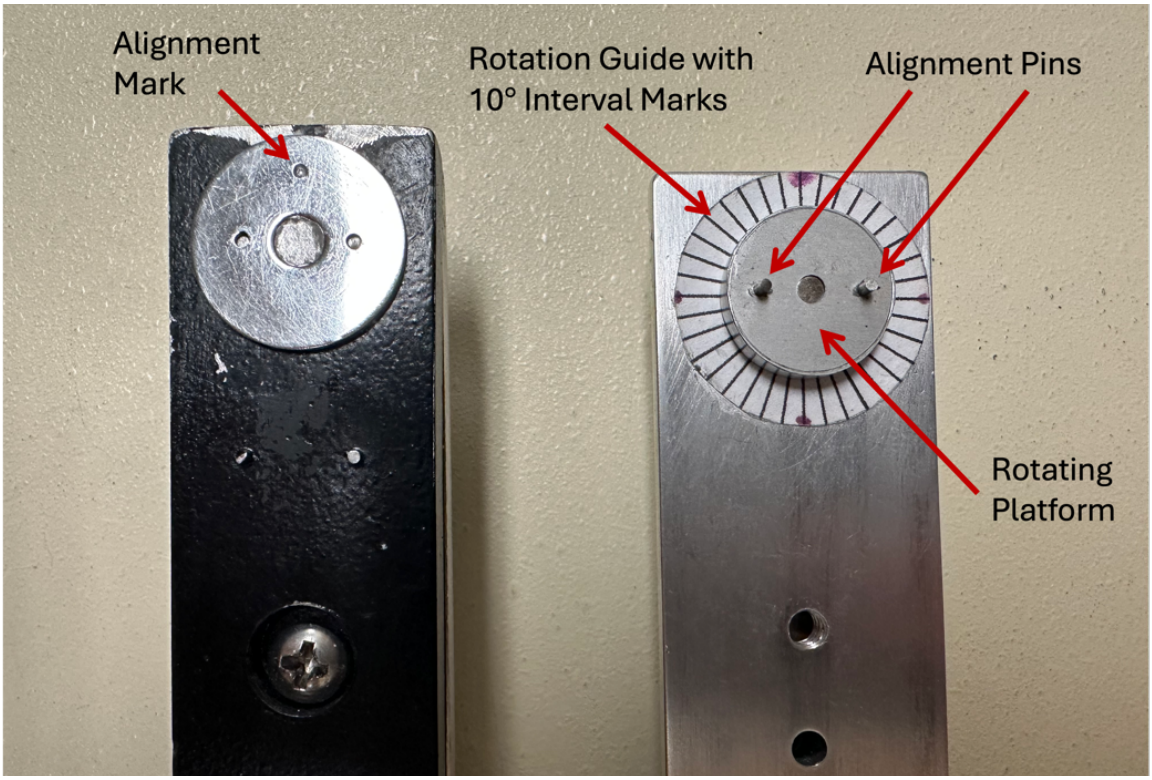

Figure 2.4: Photograph of fixed slider and rotating slider.

2.3 Button-IR VT-DRIFTS Heating Configurations

2.3.1 Quartz Holder VT-DRIFTS Apparatus

When making measurements during VT-DRIFTS analyses it is necessary to account for artifacts caused by sample heating in addition to optical artifacts.[108-110] Traditional VT-DRIFTS sample holder designs isolate samples from the infrared spectrophotometer optics by placing them inside an “environmental chamber”.

Common chamber designs consist of a metal cover containing infrared transparent salt windows that are attached to a metal base containing the sample holder, heater, and purge gas inlet and outlet ports. Environmental chamber bases and covers are typically constructed from stainless-steel. The stainless-steel cover and base, infrared transparent salt windows, and rubber o-ring seals all have different thermal expansion coefficients. Consequently, these components are subjected to different temperature versus time heating profiles, and they expand and contract at different rates, leading to spectral artifacts arising from complex temperature-dependent changes in optical alignment. These changes can distort “real” sample related peaks, making the elucidation of absorbance band properties and temperature-dependent trends more difficult.[109, 111-112]

Fortunately, these artifacts and optical alignment artifacts can be eliminated by simply eliminating the sealed sample chamber. Additionally, elimination of the environmental chamber increases the optical throughput, which improves spectral signal-to-noise ratios. A further increase in optical throughput is gained by replacing the traditional diffuse reflectance sample cup with a button sample holder, which also facilitates spectral measurements of neat samples.[113] Figure 2.5 shows a schematic of the quartz tube hot air button sample heater system. Samples are heated in a button placed on top of the quartz tube by passing 100 mL/min dry air purge gas from the bottom of the quartz tube, around a cartridge heater, and against the bottom of the button. A quick response thermocouple was

placed in contact with the sample surface exposed to infrared radiation to record sample temperatures. Red arrows indicate the direction of the heat transfer from the dry air purge to the bottom of the button, to the sample in contact with the button, and to the button surface, which is in contact with the thermocouple.

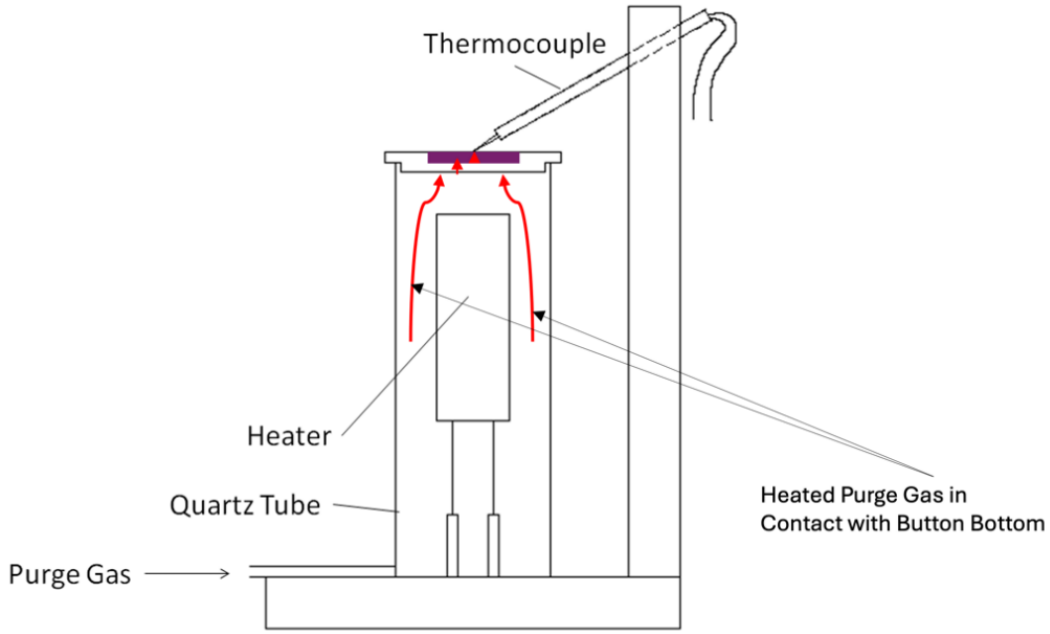

Figure 2.5: Diagram of the variable temperature diffuse reflection infrared spectroscopy apparatus with the button sample holder placed on top of a quartz tube containing a cartridge heater. Red arrows indicate the direction of the heat transfer. The thermocouple is placed in contact with the sample surface.

When using a traditional DRIFTS sample cup, most samples must be mixed with a non-absorbing infrared diluent to avoid bottoming out of peaks and/or the Restrahlen band inversion. The presence of diluent, however, can complicate

infrared spectra through interactions between the sample and diluent.[114-115] For example, Miller et al. (1970) found that percussive grinding of kaolinite with KBr resulted in mechanical dehydroxylation, but as the grinding proceeded, compensatory hydroxylation by atmospheric water occurred.[114] Diluent is not required when a button sample holder is employed. Thus, by using an open sample heating system design and a button sample holder, increased optical throughput and elimination of diluent interactions and temperature-dependent alignment changes enhance measurement sensitivity and minimize spectral artifacts for VT-DRIFTS studies.

2.3.2 Button-IR with Thermoelectric Chip Heating/Cooling

Faster sample heating and cooling was achieved by using a modified button sample holder and a Peltier thermoelectric chip (TEC) for heating and cooling.[116] Figure 2.6 shows the components of the button TEC heating/cooling system.

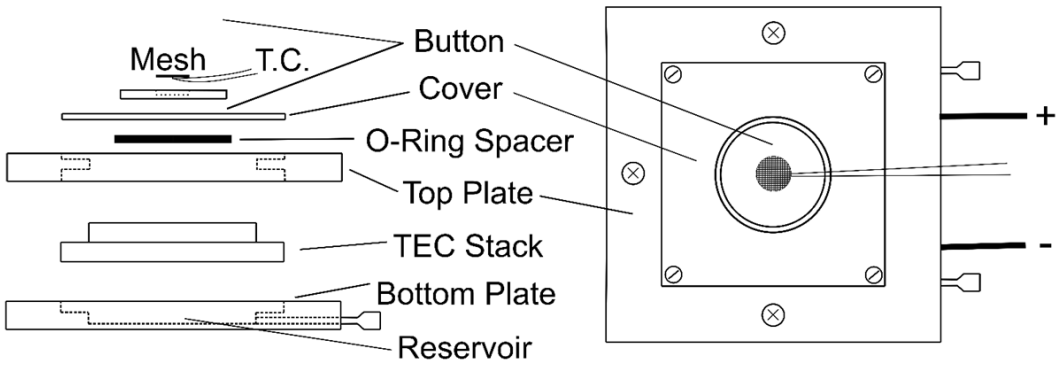

Figure 2.6: TEC button sample holder heater/cooler.

Rapid sample heating and cooling were facilitated by using two thermoelectric chips in a stacked configuration, where one chip served as a heat sink for the other.[117-118] Sample temperatures in this configuration could be adjusted by controlling the heat transferred between the upper TEC and the lower TEC. Both TEC devices were purchased from Analog Technologies, Inc. (San Jose, CA) and could operate between -55 ^{o}C and 200 ^{o}C. The upper TEC (ATE1-127-5ASH) was 30 mm x 30 mm x 3.46 mm thick. The lower TEC (ATE1-127-6ASH) was 40 mm x 40 mm x 4.09 mm thick. A 30 mm x 30 mm x 2 mm (1.8 mL) liquid coolant reservoir was sandwiched between the lower surface of the bottom TEC chip and the aluminum plate bottom. This reservoir was used to remove heat from the system by circulating a 24 ^{o}C 50:50 water/ethylene glycol mixture by using a ThermoFisher Scientific (Waltham, MA) Neslab RTE-4 recirculating chiller. TEC edges were sealed with silicon adhesive and pressure was applied from the top plate to ensure good contact between the two TEC devices.

To improve thermal conductivity between the two thermoelectric chips, a small amount of Arctic Silver 5 (Visalia, CA) thermal paste was applied to the underside of the upper TEC. When clamped together, the Artic Silver 5 spread into a thin layer, providing improved thermal contact between the upper and lower TECs. A 0.75 inch hole in the stainless-steel cover plate above the upper TEC provided an opening to accommodate a modified button, which was in direct contact with the upper TEC. The TEC stack and modified button sample holder

were contained and clamped together within a 60 mm x 60 mm x 11.5 mm aluminum enclosure. These dimensions were small enough to permit the entire unit to be mounted on a slide to facilitate quick introduction and removal from the FTIR via a slot in the Plexiglas purge cover. This not only allowed for fast positioning of the sample at the focus of the PM optics, but also maintained the dry air purge of the FTIR, which would have been lost if the sample compartment were opened.

A specialized button was constructed for use with the TEC VT-DRIFTS heating/cooling apparatus. The bottom of a highly polished 1.5 mm thick aluminum disk was pressed against the top surface of the upper TEC. This disk had a ca. 0.25 inch recess into which the wire mesh was placed. The wire mesh was spot welded to a 0.30 thick stainless-steel backing. An Omega Engineering Inc. (Norwalk, CT) CHAL010 type K thermocouple was spot welded to the opposite side of the backing. This assembly was attached to the bottom of the aluminum disk recess by using high temperature JB Weld (Sulfur Springs, TX) epoxy. While mesh sizes can be variable, a 100 mesh was chosen for this modified button prototype. A picture of the assembled apparatus is shown in Figure 2.7.

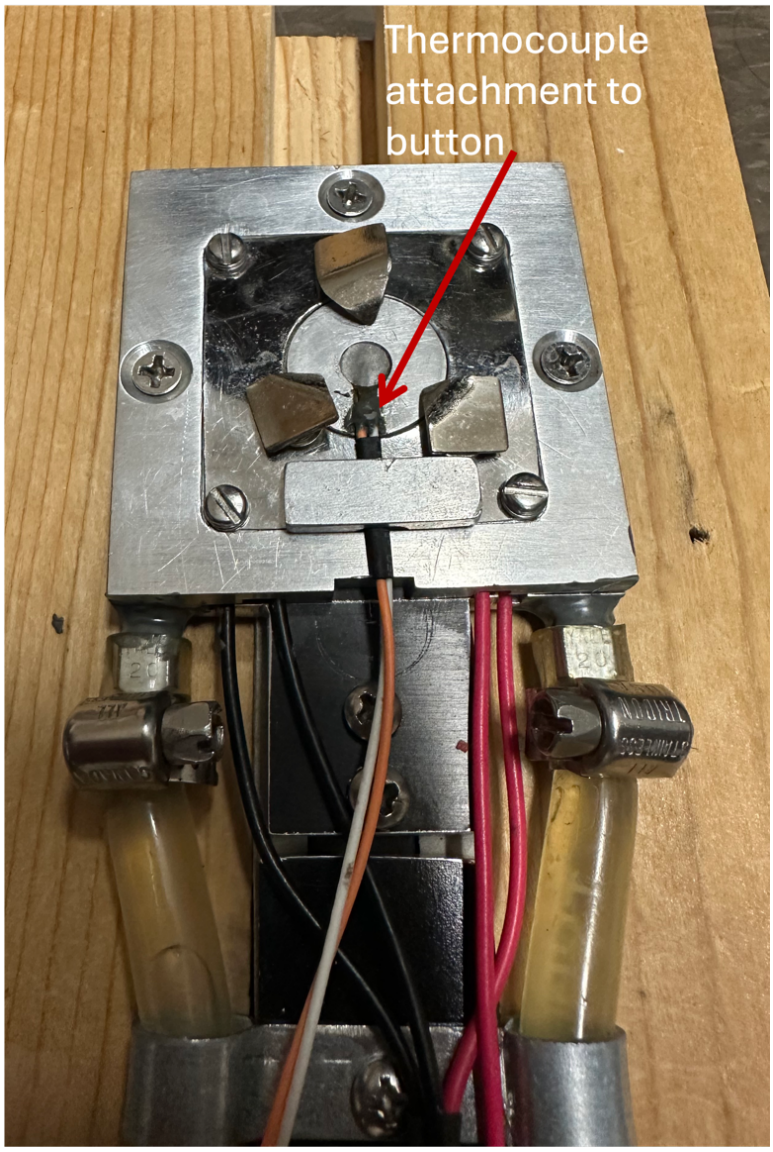

Figure 2.7: Button heating/cooling apparatus with stacked thermoelectric chips. The button sample holder used with this apparatus contained a permanently attached thermocouple.

Button temperatures were largely determined by the temperature of the upper thermoelectric chip and partially influenced by radiant heat from the

spectrophotometer purge gas and incident infrared beam. Permanent attachment of the thermocouple on the bottom of the wire mesh backing facilitated more accurate and reproducible sample temperature readings when compared to the quartz tube heating system (Figure 2.5). The modified button sample holder could be inserted and removed from the top opening in the TEC heating and cooling stack for analyses and cleaning. Unlike regular buttons that do not contain an attached thermocouple, the durability of the modified button was dependent upon the fragility of the attached thermocouple.

Thermal heating and cooling profiles could be applied by controlling the TEC stack electrical power supply. A model ATEC302 temperature controller and FTX700DX H-bridge amplifier from Accuthermo (Fremont, CA) provided DC power (12 V, 5 A max) in parallel to the stacked TECs. Feedback was provided by the voltage derived from the modified button thermocouple. The H-bridge amplifier allowed applied voltage polarity to be reversed, which facilitated both rapid heating and cooling of the sample. Given that the external surfaces of the TEC chips were ceramic, which has a low thermal expansion coefficient, the risk of optical misalignment due to sample height variations during heating and cooling cycles was minimal.

Programs written in the C++ programming language were used to measure sample temperatures while applying customized heating and cooling profiles. These programs were incorporated into Mattson Instruments FTIR macro

programs that were used to acquire spectra so that interferogram data acquisitions and sample temperature measurements could be controlled together. These macro programs were used to generate automated temperature steps, implement isothermal periods, initiate heating and cooling ramps, and to activate interferogram data collections at predetermined times and temperatures. The TEC stack heating and cooling system was able to control isothermal sample temperatures to within ± 0.1 ^{o}C and heating and cooling rates exceeding 2 ^{o}C/s could be sustained between 0 ^{o}C and 150 ^{o}C. As a result, sample temperature could be changed between -40 °C and 150 °C in a matter of seconds. Heating from -20 °C to 150 °C required approximately 30 seconds. Cooling from 150 °C to -20 °C required nearly a minute due to limitations on the rate of heat transfer to the coolant reservoir. A temperature range of -50°C to 200 °C is theoretically attainable with the TEC stack apparatus and chilled coolant recirculator. However, ice formation after sustained periods below 0°C, which affected measured spectra, occurred because some water vapor remained inside the purged FTIR environment. Inherent limitations of the piezoelectric components comprising the thermoelectric chips could result in damage after many heating and cooling cycles.[116] Consequently, sample temperatures were restricted to between -40 °C and 150 °C for the studies described here.

2.4 Working Principle

The button backing and the mesh wires affect how radiation is reflected. Sample properties also affect the directions over which radiation is reflected. Some examples are provided in Figure 2.8.

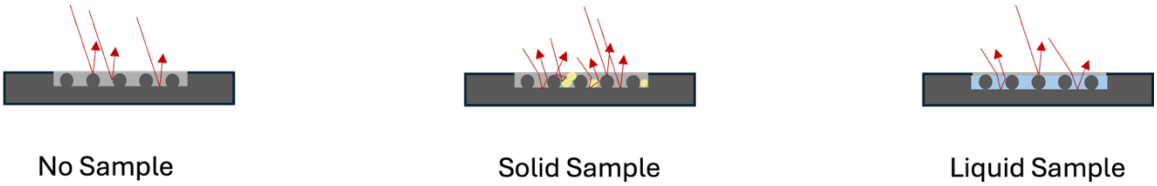

Figure 2.8: (a) Empty, (b) solid, and (c) liquid filled buttons with typical reflections for each case.

After reflection, radiation leaving an empty button surface can be described as variable angle specular reflection, with exit angles determined by the incident radiation angle. The wide range of reflection angles is due to the combined flat and round surfaces provided by the backing and mesh wires respectively. When a solid sample is loaded into the mesh void spaces, some of the radiation that previously reflected off the polished surfaces of the sample holder will pass through sample particles and contribute to diffuse reflection. Reflected radiation is therefore partly diffuse reflection from the solid sample and partly variable angle specular reflection from the sample holder. When non-scattering liquids are loaded into the mesh voids, reflected angles are altered by refraction and therefore dictated by the refractive index of the sample. Reflected radiation angles for liquid samples are therefore partially determined by refraction by and reflection from the sample

holder backing and mesh wires, which is similar to transflectance measurements. It is apparent in Figure 2.9 and Figure 2.10 that the base, mesh wire diameter, type of weave, and sample thickness impact reflectivity.

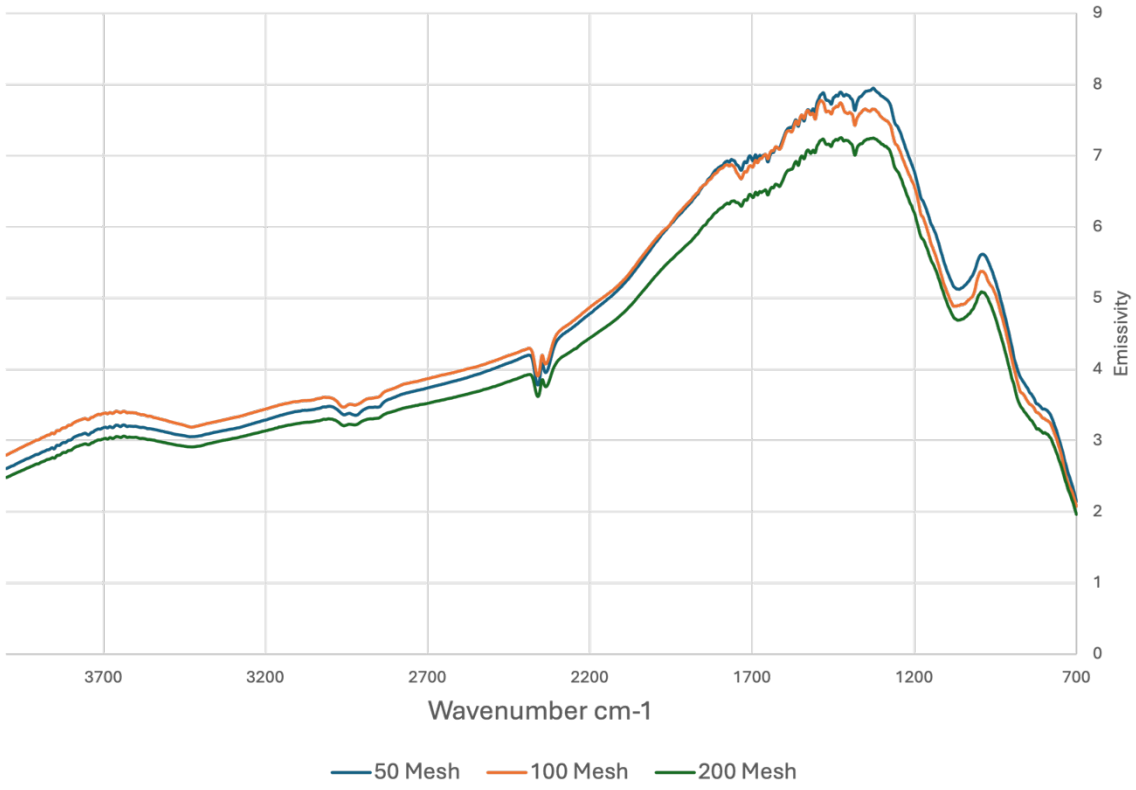

Figure 2.9: Plots of emissivity versus wavenumber for empty buttons with 50, 100, and 200 meshes.

Figure 2.9 shows the diffuse reflectance emissivity from buttons containing 50, 100, 200 meshes. As expected, as the number of wires per square inch increased, so did the diffuse reflectance emissivity. As expected with these plain weave meshes (Table 2.1), larger wire diameters or higher numbers of wires per square inch decreased void volumes and increased diffuse reflectance emissivity.

This is because the polished backing surface accounts for most of the specular reflectance radiation component. Figure 2.10 shows emissivity plots for the 635 (twill weave) and 2800 (sintered) meshes. The diffuse reflectance emissivity for these two meshes were similar.

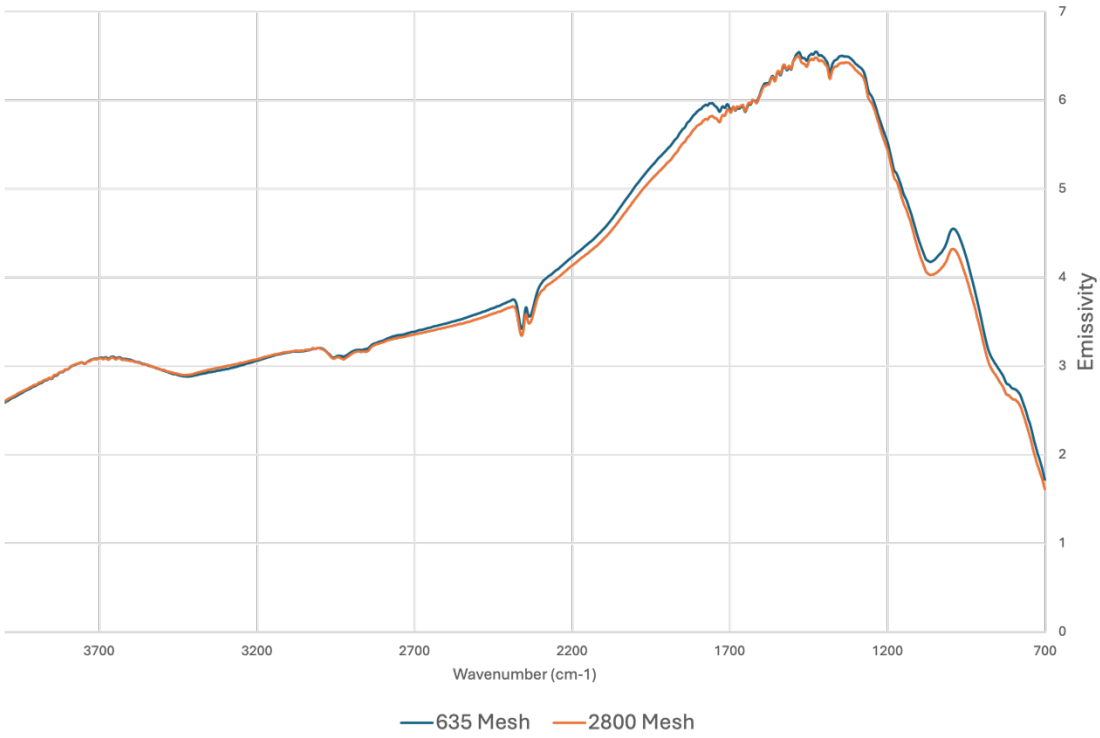

Figure 2.10: Plots of diffuse reflectance emissivity versus wavenumber for empty buttons containing 635 and 2800 wire meshes.

2.5 Sampling Considerations

The implementation of the button sample holder for VT-DRIFTS studies offers a new approach for analysis of liquid and powder samples. Because the mesh provides a means of creating thin sample layers, and therefore short radiation pathlengths, neat samples can be studied by Button-IR VT-DRIFTS.

Because the wire mesh provides a wide reflection angle range necessary for the PM optical system, samples such as: low volatility liquids, oils, greases, and pastes can be subjected to variable temperature analyses. Samples can be analyzed and safely stored within wire mesh void spaces, allowing for re-analysis at a later time. Button sample holder mesh properties dictate the amount of sample required for analyses. Typically, less than 1 mg is needed to completely fill a button sample holder.

2.5.1 Liquid Sample Loading

Buttons can be utilized as a variable path length sample holder for liquids.[119] The reservoir of a recessed button is particularly suited for liquid samples. When loading a liquid sample into a recessed mesh button, the sample depth and radiation distance traveled through the sample increase as larger volumes are added. It was previously shown that absorbance pathlengths for liquids added to recessed mesh buttons varied in a non-linear fashion relative to added sample volume. This was due to the round shapes of mesh wires, which resulted in the metal wires displacing differing amounts of fluid as the mesh was filled from bottom to top. However, it was found that constant pathlengths could be obtained when the same sample volume was dispensed.[107]

Another important factor when choosing which mesh to use for liquid sampling is the potential for baseline drift. When 0.2 μl aliquots of paraffin oil were added with a blunt tip Hamilton 10 μL graduated syringe (Reno, NV, ±1% accuracy)

until the button reservoir was full, less baseline distortion occurred with meshes having more openings/in. (i.e. tighter weaves) as shown in Figure 2.11. The inset plot shows the severe baseline drift above 3520 cm^{-1} for the 100 mesh. This may be due to the interplay of adhesion to the wires and cohesion forces within the sample causing the oil to “crawl” over the surface of the wire through capillary action. The more uniform baselines obtained by using the 635 and 2800 meshes may be due to the smaller void spaces producing less specular reflection from the stainless-steel backing. Also, the tighter weave likely provided a more uniform sample layer and therefore more consistent pathlength due to a more even sample distribution across the wire mesh.

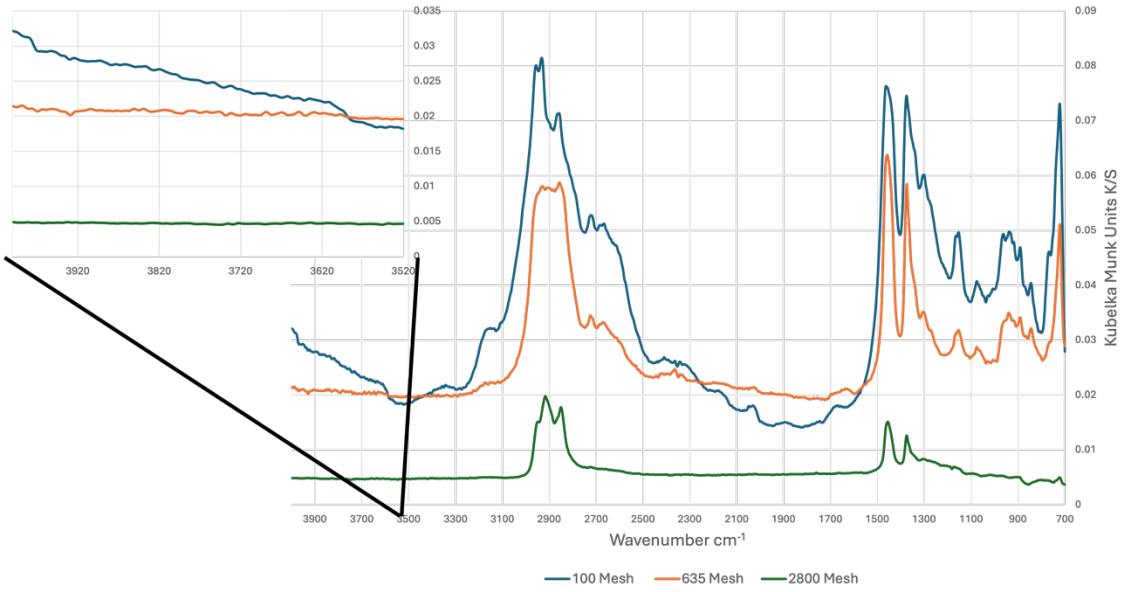

Figure 2.11: Paraffin oil spectra obtained by using half-filled 100, 635, and 2800 mesh buttons. Spectra were obtained at button rotation angles corresponding to maximum emissivity.

2.5.2 Solid Sample Loading

There are some practical sampling considerations to take into account when performing traditional DRIFTS measurements of solid samples. For example, particle sizes should be small and uniform to obtain narrow absorbance bandwidths and better relative band intensity reproducibility. This may necessitate sample grinding prior to analysis. Traditional DRIFTS requires that samples should be prepared as a homogeneous mixture with an alkali salt diluent, containing about 5% sample by weight. Dilution in a non-absorbing diluent and loose sample particle packing ensure maximum IR beam penetration into the sample and greater diffusely scattered radiation without bottoming out of high absorptivity spectral peaks due to thick sample layers.[71] Thus, compared to the button method, traditional DRIFTS measurements requires significantly greater sample preparation and technical sample handling in order to achieve reproducible and meaningful results.

When solid powder samples are loaded into a button mesh, individual particles become trapped within the void spaces between the wires. Void sizes are determined by the mesh size, with the maximum particle size being defined by void cavity width (see Table 2.1). For example, by loading a 100 mesh button with a heterogeneous particle size of powdered sample, particles with diameters of 140 μm or smaller will reach the mesh backing but larger particles will reside on top of the wires and can simply be brushed off the top. Thus, particle size discrimination

can be achieved by thoughtful selection of the button mesh size. For some samples, this sieving ability during sample loading may eliminate the need for sample grinding prior to DRIFTS analysis.

Button-IR also allows for simple preparation of thin layers of neat sample material. This is simply not possible when using traditional DRIFTS sample cup holders. Traditional DRIFTS requires sample dilution for most samples, making analysis of neat samples nearly impossible. DRIFTS would theoretically require a remarkably thin neat sample layer to avoid bottoming out of spectral peaks. Reproducibly creating a sub-millimeter thick layer at the bottom of a DRIFTS sample cup in the presence of air currents, static, and other hindrances associated with modern lab conditions would be exceptionally difficult. With Button-IR, it's as simple as choosing the button with the appropriate size mesh. For example, a thin sample layer could be created by filling the reservoir of a button sample holder with material and then brushing the excess off the top of the wires. This would create a uniform sample layer with a pathlength dependent on the mesh wire diameter.

While analysis of thin layers of neat material are possible by using ATR-IR, this comes with limitations. ATR-IR necessitates uniform contact between the ATR crystal and a relatively smooth layer of sample to obtain high quality spectral data. Ensuring this uniform contact can be difficult when dealing with exceptionally small sample sizes and uneven surfaces. Furthermore, pathlengths in ATR-IR measurements are not constant and depend on the refractive indices of the ATR

crystal and the sample, which are both wavelength dependent. The button sample holder allows for variable radiation pathlengths that are tunable through mesh size choice, button orientation, and sample fill level. Furthermore, the greater effective pathlengths resulting from different reflections from wire surfaces makes it possible to detect low absorbing species while sub-millimeter layer thicknesses prevent bottoming out of the high absorbing peaks in the same spectra. The ATR-IR technique would require two measurements (with different crystals) to obtain similar information. Button-IR with a TEC stack allows for direct variable temperature studies of the same sample across a broad temperature range without optical alignment issues produced by heating the whole sample chamber, which is not possible by traditional DRIFTS.

The best button sample holder results for neat samples typically result from loading thin layers. Often, sample material with typical particle diameters of a few microns occupies the mesh void spaces on the backing surface without extending to the top of the mesh. When the mesh is not completely filled, the best results are obtained when the layer thickness is uniform. This is illustrated in Figure 2.12, which shows the effects of adding a solid sample to a mesh in small increments. Blue spectra represent 10 scrapes, green represent 50 scrapes, and orange represent 110 scrapes. Solid lines represent spectra before baseline correction. Dotted lines represent spectra after baseline correction. Abrasion of turquoise samples removed approximately 2-3 μg per scrape. Turquoise samples were

provided through collaboration with the Pailes Lab from the Anthropology Department at the University of Oklahoma. As more sample was added, more void space was filled with sample and the layer became thicker, resulting in greater baseline drift due to increased diffuse scattering by the sample.[40]

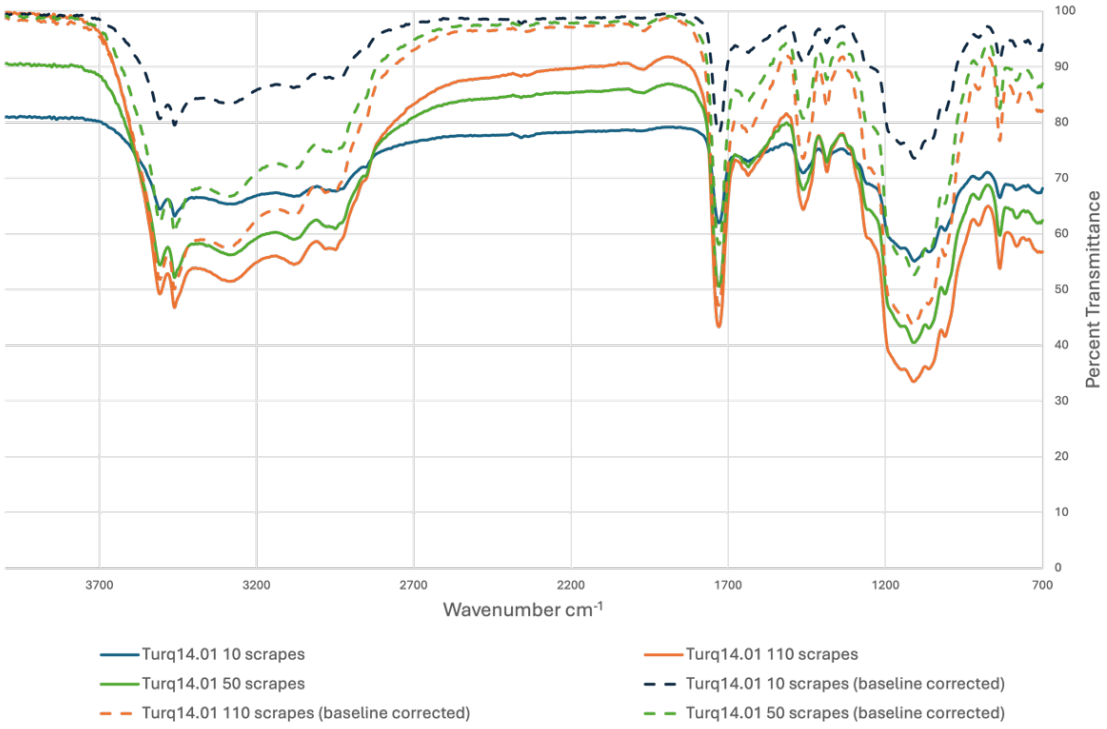

Figure 2.12: Turquoise sample baseline drift as a function of added material using the abrasion sample collection method.

Drifting baselines can be corrected by using software provided by the FTIR manufacturer. This is typically achieved by subtracting straight lines passing through selected wavenumbers corresponding to the infrared spectrum baseline. However, the best approach is to load samples as thin layers because this

procedure tends to produce fewer baseline deviations, which reduces the need for baseline correction.

Using neat sample thin layers for analyses eliminates the need for sample dilution, which is common with traditional DRIFTS measurements. This saves time and effort and is particularly advantageous for highly absorbing samples, such as carbon black (Figure 2.13).

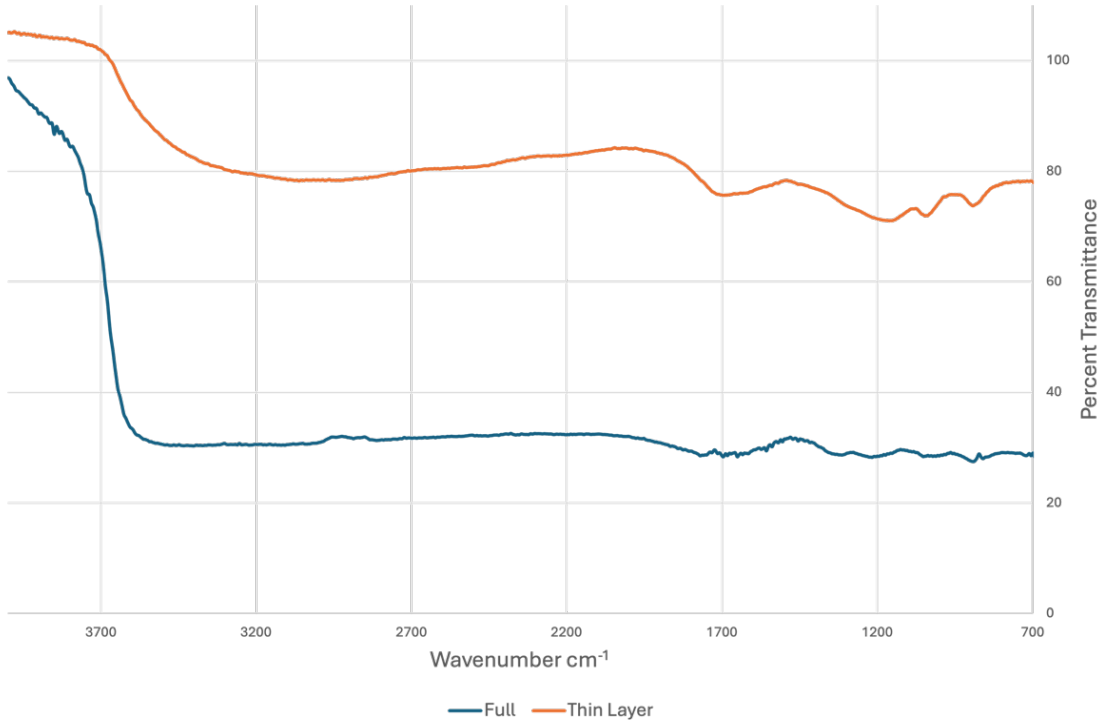

Figure 2.13: Full button versus thin layer spectra of carbon black. The blue spectrum was obtained with a 100 mesh button filled to the top of the wires with carbon black. The orange spectrum was obtained by placing a thin layer of particles in the button.

Interestingly, when filled to the top of the wire mesh with this challenging sample, the infrared spectra did not “bottom out” in the traditional sense (i.e. 0% transmittance at the detector). This was likely due to some continued reflectance from the wires visible at the top of the sample. Nonetheless, discreet spectral information was lost, and some peaks began to invert, further proving the need for a thin layer. The thin layer spectra, represented in orange, demonstrate the return of distinctive peaks like the carboxylic acid peak around 1710 cm^{-1}.[120]

2.5.3 Abrasion Sample Loading

The neat sampling capabilities and particle size selectivity provided by the exposed mesh button allow for material to be added to the mesh voids by rubbing the wire mesh across a sample surface. This method of sample loading requires no preparation steps. This abrasion sample loading technique was employed to obtain the treated turquoise sample spectra shown in Figure 2.14.

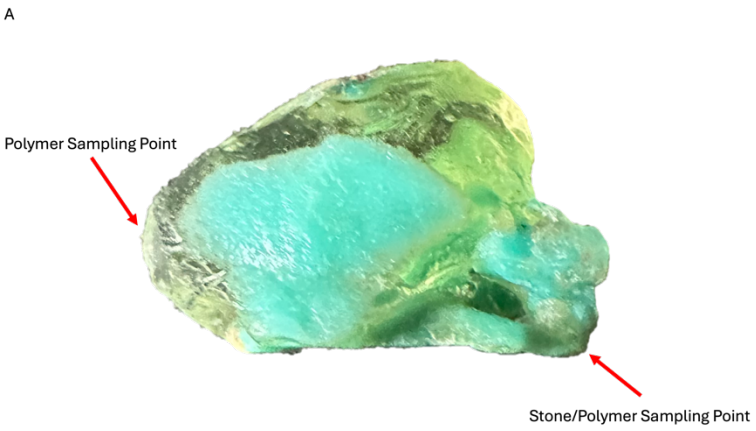

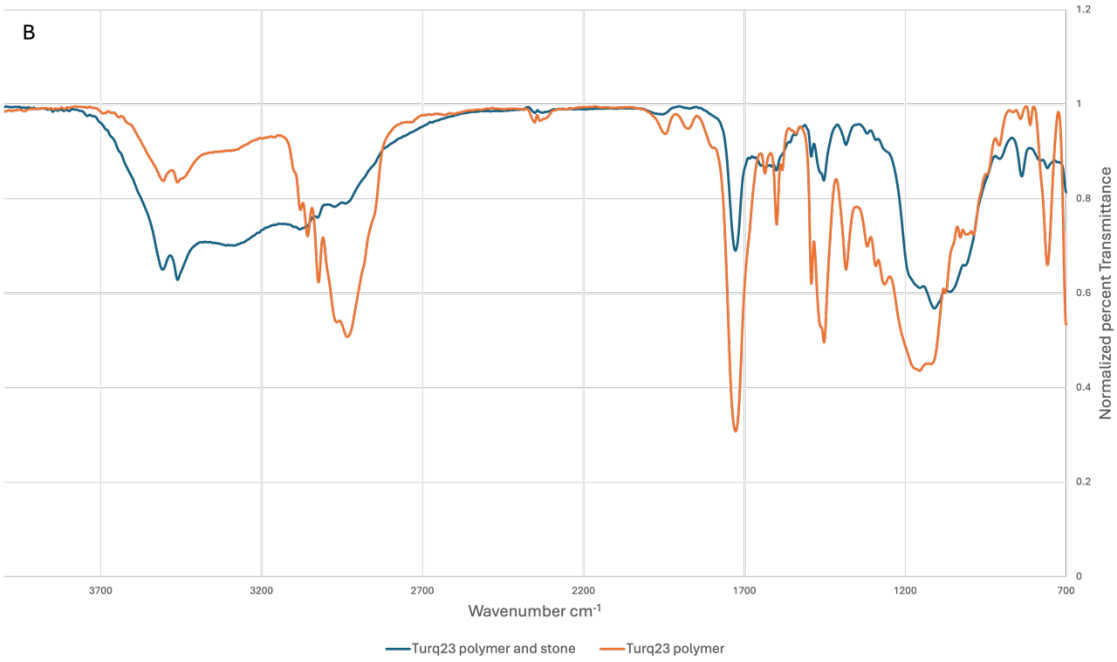

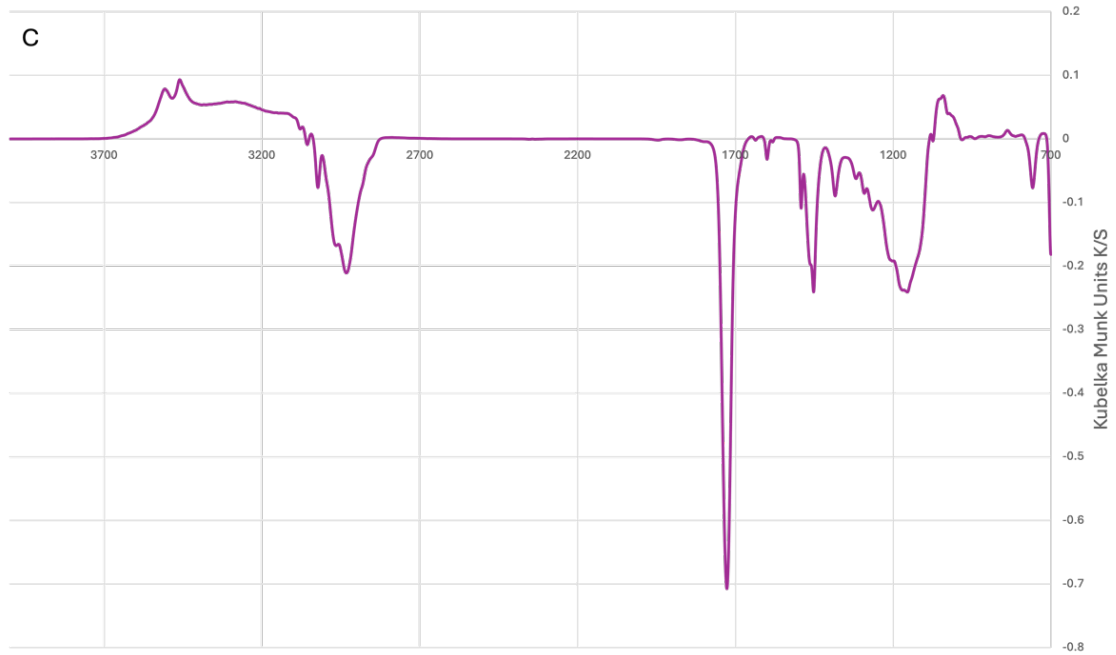

Figure 2.14: (A) Photograph of sampling locations. (B) Spectra of stabilized turquoise sampled at the polymer coating and at a location that appears to be

both polymer and turquoise. (C) Difference spectrum obtained by subtracting the polymer scrape spectra from the polymer and stone spectra.

The samples for Figure 2.14(A) spectra were obtained from the designated locations shown in Figure 2.14(B). The carbonyl stretching peak around ~1730 cm^{-1} is characteristic of the polymer impregnation of the turquoise sample. This band along with those at ~1600 cm^{-1} and ~1453 cm^{-1} (CH_3 bending), and in the 2800-3100 cm^{-1} (C-H stretching) range suggests that this turquoise may have been treated with Norland Optical Adhesive 650 as well as other plasticizers. Peaks at ~3503 cm^{-1} (Al-O-H stretching in aluminum phosphates), 3460 cm^{-1}, 3270 cm^{-1}, 3085 cm^{-1} (H_2O, OH), and the broad overlapping bands in the 1000-1150 cm^{-1} (PO_4^{3-} stretching) region were attributed to the turquoise mineral.[121-124] As expected, these peaks were above the x-axis when subtracting the spectrum corresponding to the point A sample location from the point B sample location spectrum, thus demonstrating that qualitative identification of unknown material is possible by using the abrasion sampling method.[125]

Abrasion sampling is quick and minimally destructive. The mesh simultaneously removes and traps small quantities (ca. μg) of solid material. This sampling method could be used for fast infrared analysis and the removed sample could then be stored indefinitely on the stainless-steel button surfaces. These sample containing buttons could be manipulated, transported, and undergo repeated infrared measurements or other non-destructive analyses without

significantly disturbing them. This neat sampling approach facilitated by the button sample holder results in spectrum signal-to-noise ratios that are comparable to results obtained for a ~20 fold sample dilution by traditional DRIFTS. The abrasion sample loading technique is more convenient than using ATR to obtain spectra because sample preparation steps, such as scraping off material and grinding to a fine powder, are unnecessary.[126]

The simplicity and rapidity of the abrasion sample collection method makes it particularly attractive for characterization of materials that cannot be significantly marred or fully ground to a powder and must remain under controlled conditions, such as preserved archaeological artifacts. A one-time abrasive sampling of these pieces can be stored and repeatedly analyzed indefinitely. Abrasion sampling has the potential to make available new artifact sets to chemical analyses that would otherwise not be possible due to cultural integrity and analyte alteration concerns. For example, intact ceramic vessels are prized artifacts contained in museum collections that are rarely made available for chemical analyses. These vessels may offer significant insight into the past, but current analytical, sample preparation, and sample collection techniques would damage these artifacts.[127]

2.6 Button Sample Holder Orientation

Early button sample holder prototypes consisted of 0.75 inch diameter stainless-steel disks with a roughly 0.25 inch diameter mesh that was spot welded at the center. While these prototypes provided reasonable DRIFTS spectra, early

studies revealed that infrared spectra were dependent on the orientation of the mesh weave pattern with respect to the incident radiation.[16-17, 91, 128]

2.6.1 Method

Inconsistent weave pattern orientations were due to the difficulty of reproducibly spot welding the mesh with the same orientation. Still, reproducible spectra were obtained by aligning the button sample holder with the incident radiation beam in the same manner each time. An alignment reference point indentation was added to the button design to ensure consistent mesh orientations. Alignment pins on the sample introduction slide were required to maintain the mesh orientation for repeated measurements (Figure 2.15). Button backings were made from 430 grade stainless-steel to use a magnet to hold the sample holder firmly to the sample introduction slide and to eliminate variations in pitch and yaw, thus keeping the button stable and level while inside the FTIR.



Figure 2.15: Button orientation marker evolution: The first button prototype started out with no alignment markers. Once spectral changes due to button orientation were noted, an alignment mark was added as in the middle button. This alignment

mark was a small indentation at one edge of the button. The alignment pin holes in the button on the right were added to further enhance alignment reproducibility.

The underlying principles for solid sample measurements with the button sample holder differ from those pertaining to liquids. Because the pathlength through a layer of irregularly shaped particles is not constant, Beer's Law does not apply. Instead, conversion of reflectance spectra into the Kubelka-Munk format is necessary to obtain band intensities that are roughly proportional to concentration.[129] Given that both the sample particles and wires of the mesh are reflecting the radiation collected by the PM optics, it is important to better understand how different mesh orientations may impact measured spectra.

Reflected radiation from non-scattering homogenous liquid samples in Button-IR arise from reflections from of mesh wires and from the backing after refraction through the liquid. Button-IR infrared spectra for liquid samples resemble those measured by using a transmission cell, however, differences in band widths and relative intensities are apparent.[119] Given the difference in the paths by which radiation reaches the detector in Button-IR of liquids versus Transmission-IR, it is important to note the effect of mesh properties, such as wire diameter, weave pattern, and number of wires exposed to incident radiation, on the angular distribution of the radiation emerging from the sample. It was previously noted that pathlength could be adjusted by changing the sample volume added[119] and that the structure of the wires woven over each other in a plain or

sintered pattern exhibit somewhat different sample depths for incident radiation at the base of mesh void spaces versus compared to the edge of the wires (Figure 2.16). The average pathlength is indicative of all possible depths and reflections of radiation that pass into the sample. Rotational investigations were initiated out of an interest in determining if the rotation angle of the mesh could be used to fine tune the infrared radiation pathlength.

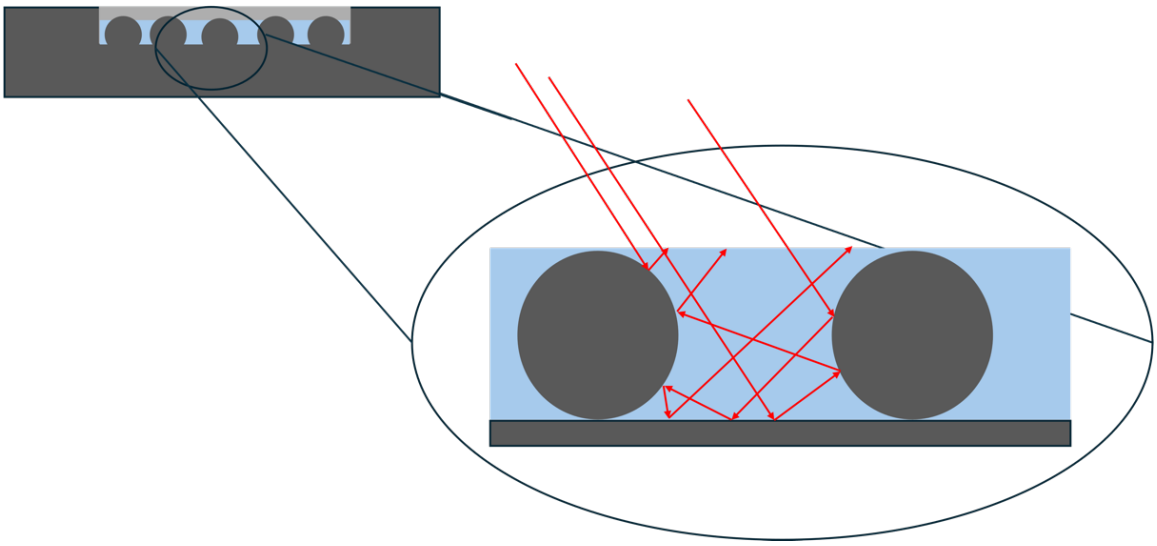

Figure 2.16: Profile view of button cavity demonstrating different sample depths (i.e. different total pathlengths) due to wire curvature.

2.6.1 Button Rotation Studies

To investigate the impact of changing the mesh orientation on spectrum quality and determine if pathlengths could be fine-tuned by adjusting the mesh orientation, infrared spectra were obtained with a button sample holder while systematically changing the mesh orientation with respect to the incident radiation

beam. Single beam spectra for empty buttons with 50, 100, 200, 635, and 2800 meshes were collected at 10° increments over a complete 360° rotation. These yielded patterns containing four maxima and minima for 50, 100, and 635 meshes; and 2 maxima and minima for the 200 and 2800 meshes (Figure 2.17). Photos of mesh orientation relative to incident beam and the maxima/minima single beam diffusion patterns for each mesh can be found in Appendix A.

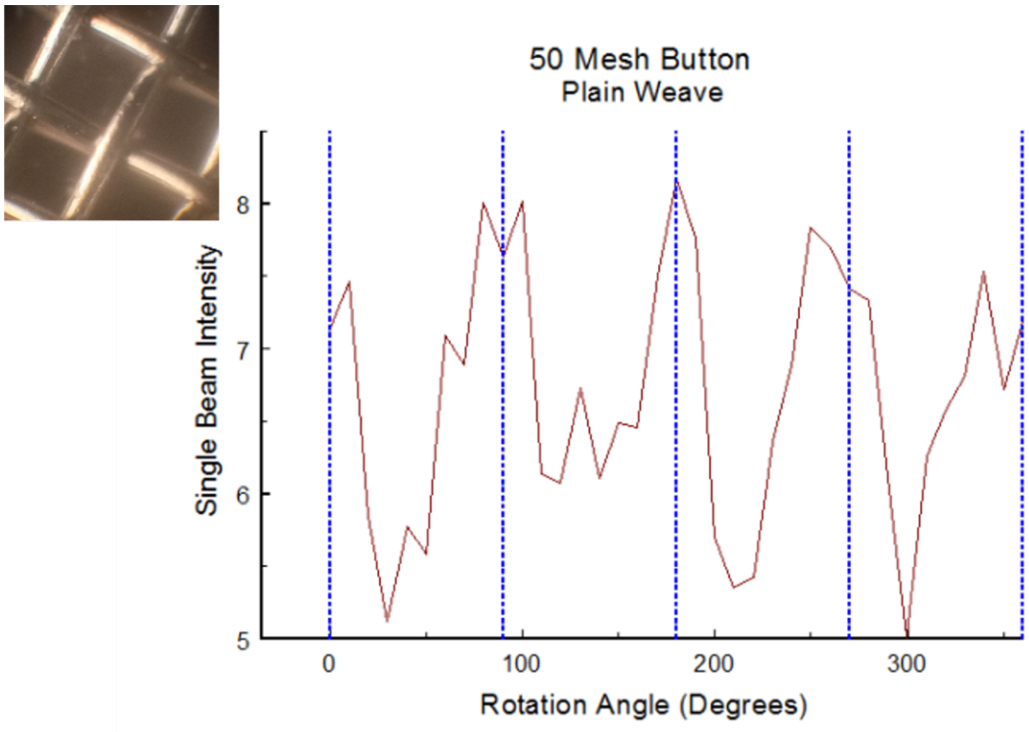

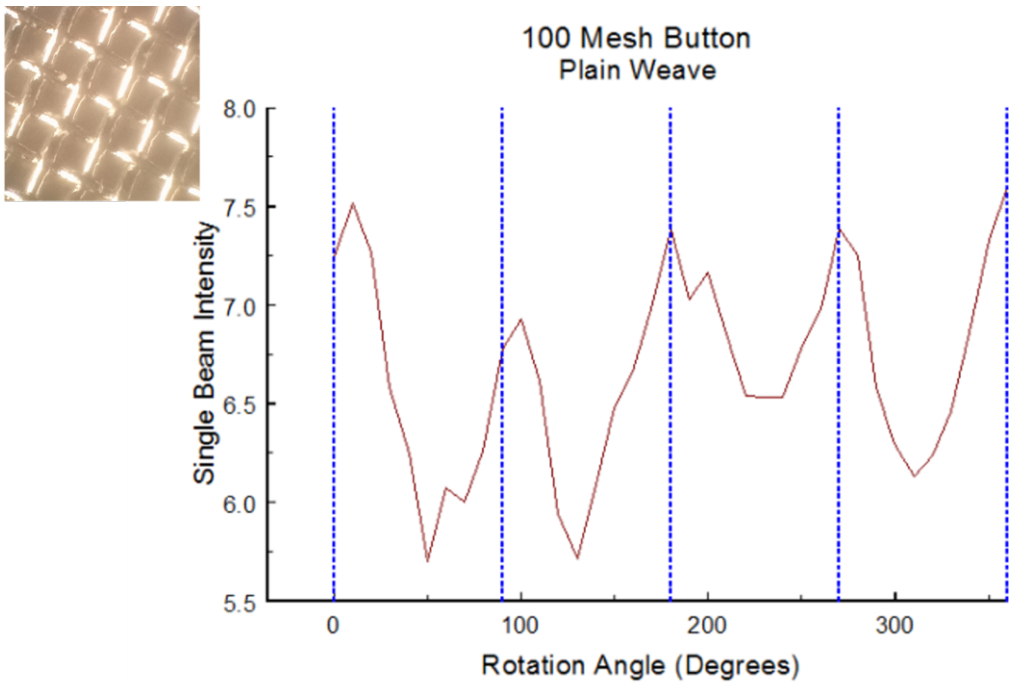
100 Mesh Button
Plain Weave
Single Beam Intensity
8.0
7.5
7.0
6.5
6.0
5.5
0
100
200
300
Rotation Angle (Degrees)

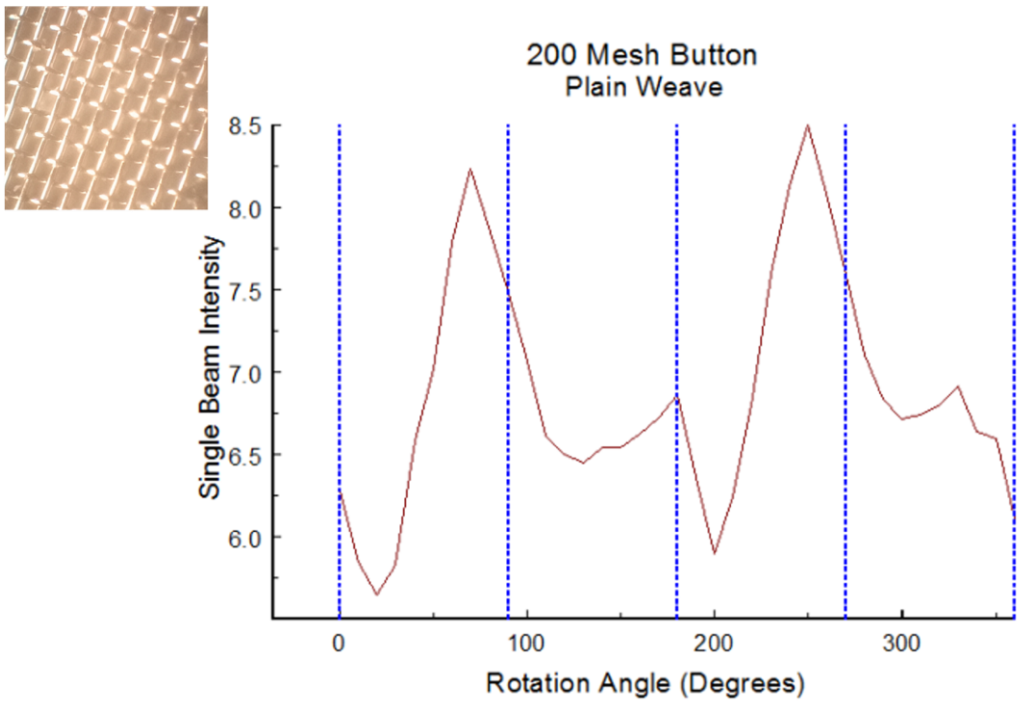
200 Mesh Button
Plain Weave
Single Beam Intensity
8.5
8.0
7.5
7.0
6.5
6.0
0
100
200
300
Rotation Angle (Degrees)

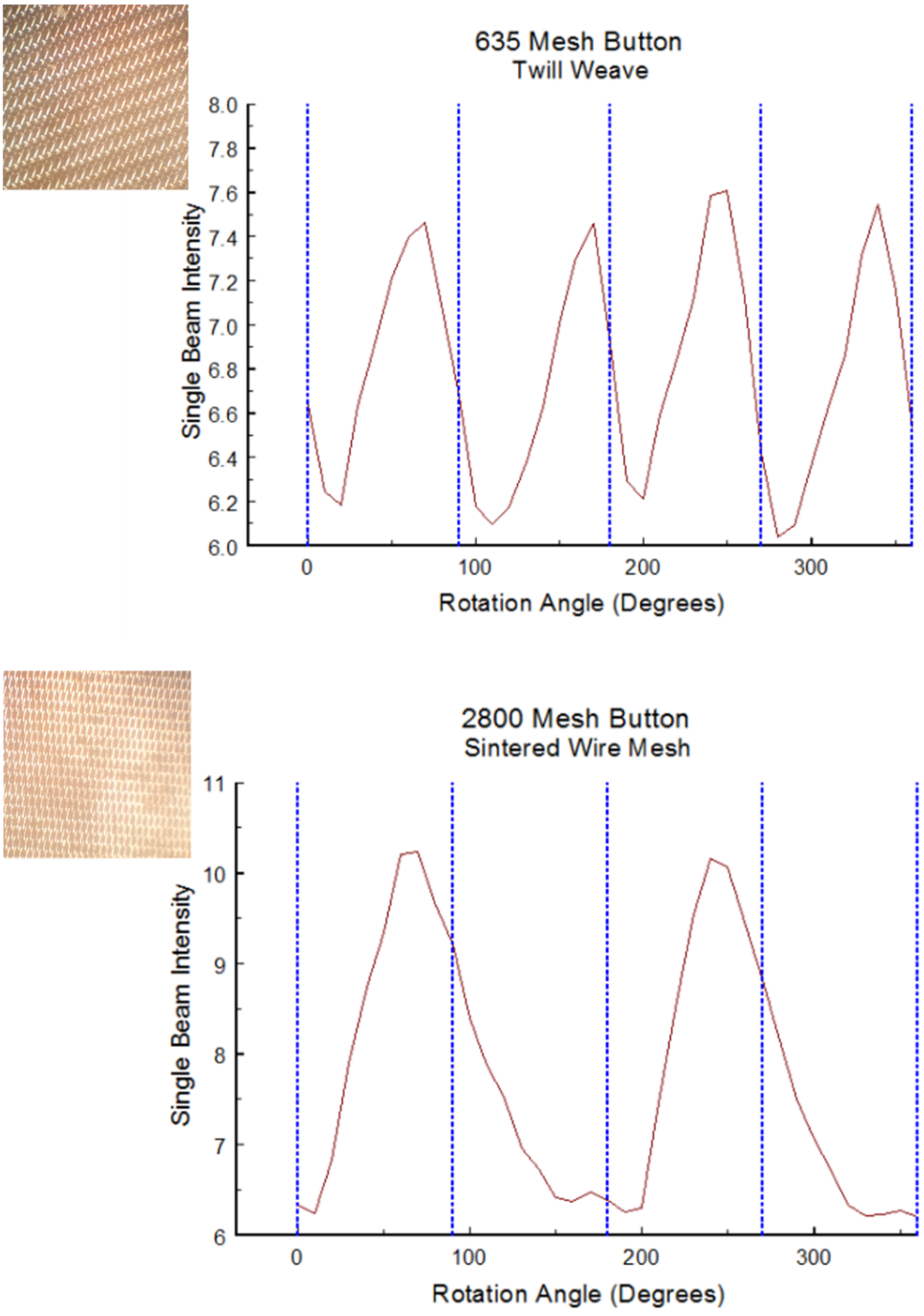

Figure 2.17: Plots of single beam intensity versus rotation angle for individual meshes (50, 100, 200, 635, 2800)

This investigation determined that spectral quality did not change significantly when the button orientation angle with respect to incident radiation was varied. However, the best reproducibility would be expected for buttons with mesh patterns orientated to correspond with maxima or minima in the rotation plots. In these regions, the single beam intensity varies the least with slight changes in rotation angle.

2.7 Summary

Ultimately, the button sample holder used for the infrared spectroscopy measurements described in this dissertation was easy to use and required minimal sample handling. It provides many of the same benefits as ATR-IR, but without the pitfalls of the crystals, which may be scratched and must be thoroughly cleaned between sample measurements. Also, the ATR-IR pathlength dependence on sample and ATR crystal refractive indices does not occur with Button-IR measurements. The button stainless-steel backing and mesh are durable and are easily cleaned, making them suitable for nearly indefinite periods of use without need for replacement. The button sample holder can be used to analyze neat samples of solids, liquids, greases, oils, and pastes, and samples can be loaded onto the sample holder by rubbing it against the surface of the material for which an infrared spectrum is desired.

Chapter 3: A High Sensitivity Variable Temperature Diffuse Reflectance Infrared Fourier Transform Spectroscopy Investigation of Temperature Dependent Structure Changes in Kaolinite

3.1 Background

A button sample holder was employed for infrared spectroscopy thermal analysis studies of kaolinite clay. Results obtained while monitoring solid-state temperature-dependent changes in this extensively studied mineral were used to assess the reproducibility and sensitivity of the button VT-DRIFTS method. By eliminating the sealed sample chamber and employing a button sample holder, spectral artifacts were minimized, and measurement optical throughput was enhanced compared to other experimental designs.

3.1.1 Introduction

Variable temperature diffuse reflection infrared Fourier transform spectroscopy (VT-DRIFTS) can be used to study temperature-dependent structural changes in solid materials.[108-110, 130-146] To obtain accurate VT-DRIFTS measurements, it is necessary to account for artifacts caused by sample heating in addition to factors that must be considered when making isothermal measurements (Chapter 2). When the open sample heating system design

employing a button sample holder shown in Figure 3.1 was used for VT-DRIFTS, the increased optical throughput, lack of diluent interactions, and elimination of temperature-dependent alignment changes enhanced measurement sensitivity and minimized spectral artifacts.

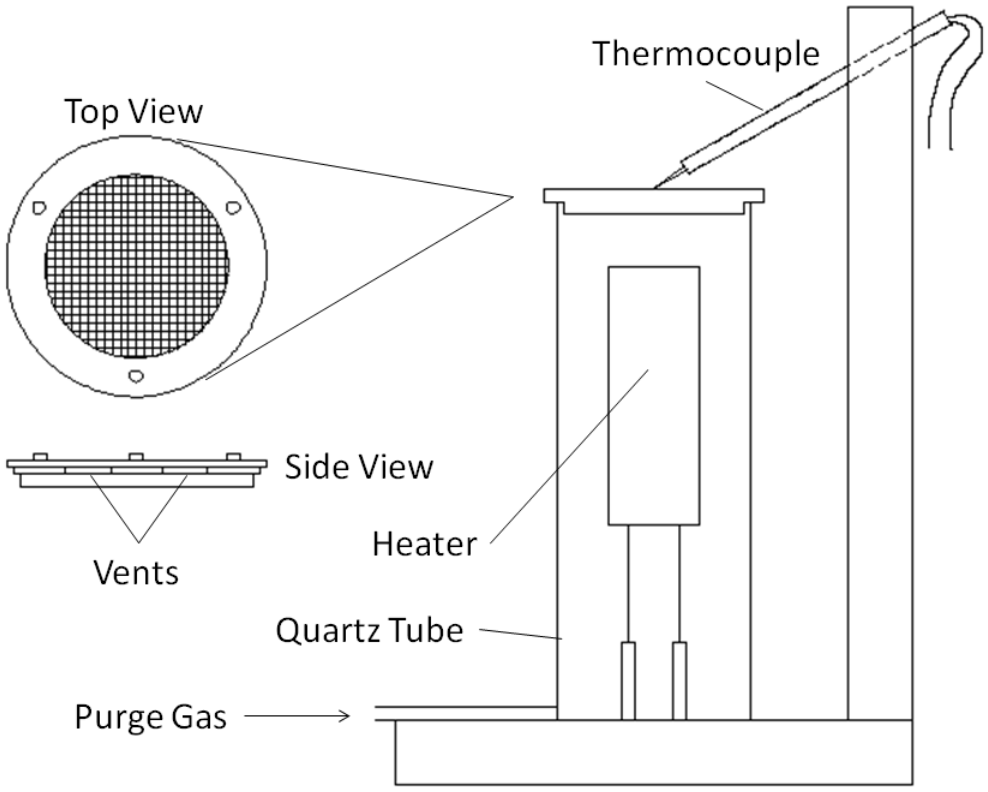

Figure 3.1: Diagram of the variable temperature diffuse reflection infrared spectroscopy apparatus with button sample holder.

3.1.2 Kaolinite

The apparatus used in this study incorporated a button sample holder and exposed heated samples to spectrophotometer purge by eliminating the sealed

environmental chamber used in traditional VT-DRIFTS analyses. The performance of this system was evaluated by applying it to monitor the temperature-dependent structural changes that occur when heating kaolinite. This material was selected to assess the new VT-DRIFTS system because its temperature-dependent structural changes are well known.[147] Vibrational spectroscopy has previously been employed to assign absorbance bands and to elucidate kaolinite structural properties.[147-161] Experimental and computational studies have determined that kaolinite ($Al_2Si_2O_5(OH)_4$) is a 1:1 dioctahedral mineral member of the silicate mineral class. It is a layered silicate clay mineral, meaning that it rarely exists as large defined crystals in nature, but rather as thin plates stacked into compact clay masses.[7] It is formed through the chemical weathering of feldspars and other aluminum silicate minerals in hot and moist environments. Indeed, ancient climates can be geologically tracked by the relative proportions of kaolinite (weathered in hot/moist climates), illite (colder climates), smectite (drier climates), and other minerals in the soil.[40]

The kaolinite crystalline structure (Figure 3.2) consists of one tetrahedral (*T*) silicate sheet (SiO_4) linked via shared oxygen atoms to an octahedral (*O*) alumina (AlO_6) sheet. In order to maintain overall charge neutrality, every third octahedral site is empty, with the others containing Al^{3+} ions.[157, 162] Kaolinite contains two types of hydroxyl groups. “Inner hydroxyls” are found between *TO*

sheets and facilitate hydrogen bonding between unit cells, whereas “inner surface hydroxyls” extend from alumina sheet exteriors.[157, 159, 161, 163]

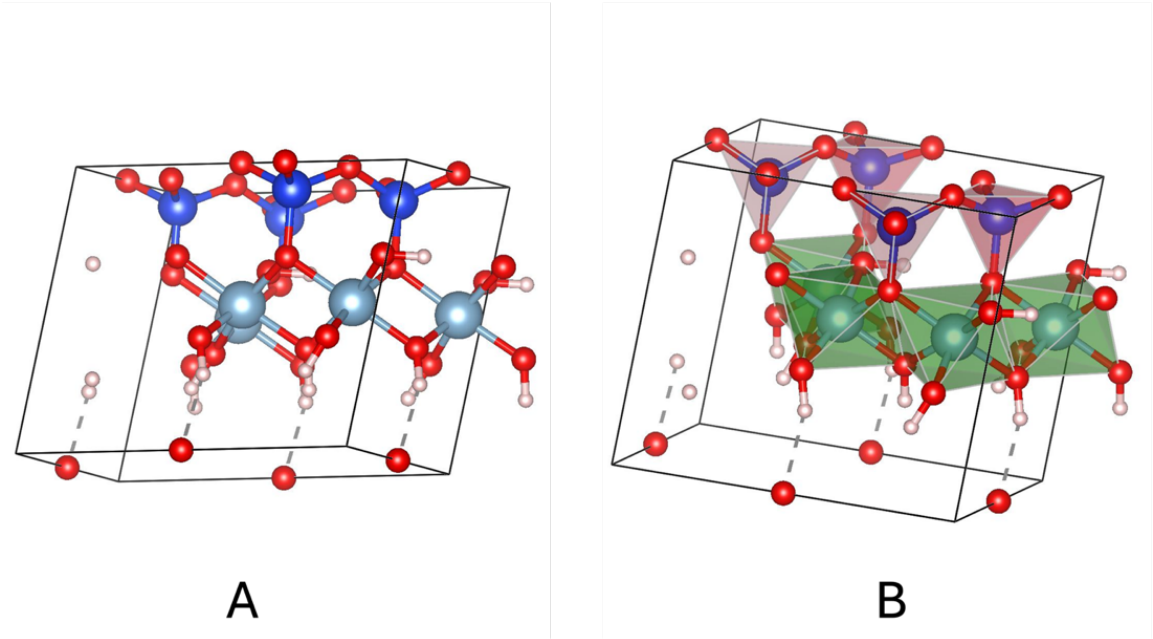

Figure 3.2: Kaolinite Structure (a) Ball and stick (b) Crystal faces. Red balls represent oxygen atoms. Dark blue balls represent silicon atoms. Light blue balls represent aluminum atoms. White balls represent hydrogen atoms. The octahedral layer is highlighted with green crystal faces. The tetrahedral layer is highlighted with red crystal faces. Crystal structure from Bish (1993).[164] Structural modelling was accomplished by using the VESTA software.[165]

When heated above 450 ^{o}C, the kaolinite lattice irreversibly loses hydroxyl groups bonded to the octahedral sheet.[166-167] Between 550 and 750 ^{o}C, kaolinite is converted to metakaolinite. Near 900 ^{o}C, the structure changes to mullite.[168-169]

Consequently, infrared spectra obtained above 600 °C exhibit a notable absence of hydroxyl stretching vibrations.[167, 170-171] Below 150 °C, infrared spectral changes reflect loss of adsorbed water and subtle temperature-dependent reversible structure changes. In this work, these changes were monitored, and the underlying processes were characterized by using a new VT-DRIFTS apparatus. Emphasis was placed on evaluating the reproducibility and sensitivity of the technique as well as the ability to distinguish between reversible and irreversible changes.

3.2 Experimental

Powdered kaolinite from Twigg County, Georgia was purchased from Ward's Natural Science (Rochester, NY). Diffuse reflection infrared spectra were obtained by using a stainless-steel "button" sample holder to analyze thin layers of neat powder.[113] Sample heating was accomplished by using the apparatus shown in Figure 3.1, which was previously employed to monitor changes in NaA, CaA, and NaY zeolites during thermal dehydration.[172-174] About 1 mg of kaolinite powder was loaded into a 6 x 6 mm (0.25" x 0.25") square opening in a 100 mesh button, which was mounted on top of a quartz tube. Dry air purge gas flowing at 100 mL/min entered the bottom of the quartz tube and flowed around a cartridge heater, transferring heated air to the bottom of the button. The button sample holder consisted of a thin stainless-steel disk to which a stainless-steel wire mesh was welded. This sample holder was attached to an alignment ring by three screws. The alignment ring outer diameter was slightly smaller than the inner

diameter of the quartz tube. The three attaching screws passed through stainless-steel washers placed between the alignment ring and button to create gaps, which served as vents for heated air to escape after the alignment ring was inserted into the quartz tube. This prevented pressure increases within the tube and improved heated gas flow rate stability. Sample temperatures were measured by using a K-type thermocouple pressed to the wire mesh button front surface. The thin layer powder sample was positioned at the focal point of a Harrick Scientific Inc. (Pleasantville, NY) praying mantis diffuse reflection accessory.[105] The sample heating profile was generated by using a Eurotherm Controls Inc. (Reston, VA) model 818p temperature controller.

A Mattson Instruments Inc. (Madison, WI) Nova Cygni 120 Fourier transform infrared spectrophotometer (FTIR) with an MCT detector was used for infrared spectroscopy measurements. Spectra were obtained over the 4000-700 cm^{-1} range by signal averaging 175 scans at 8 cm^{-1} resolution for both sample and background single beam measurements. This spectral resolution was sufficient to accurately represent small changes in the broad kaolinite bands and afforded greater spectral signal-to-noise ratio compared to higher resolution measurements.[175] Infrared spectra were obtained at 1.07 min intervals while the sample was heated from ambient temperature to 150 ^{o}C at a rate of 2.0 ^{o}C/min. Spectrum collection continued at this rate during a 5 min isothermal period at 150 ^{o}C and then throughout cooling (2.0 ^{o}C/min) back to near ambient temperature.

While heating and cooling the sample, successive infrared spectra were acquired at 2.14 °C intervals.

Thermogravimetry measurements were made with a DuPont Instruments (Wilmington, DE) 951 Thermogravimetric Analyzer (TGA). About 10 mg of neat kaolinite powder was heated by using a 2 °C/min temperature ramp from ambient temperature to 200 °C with a dry air purge rate of 100 ml/min.

3.3 Results and Discussion

The components of the apparatus shown in Figure 3.1 were selected to minimize vertical thermal expansion when heating samples, which can affect infrared spectrum baselines and absorbance band shapes.[146] The quartz tube and metal button reached the highest temperatures during VT-DRIFTS measurements. Thus, the thermal expansions of these components were the primary contributors to vertical sample position variations. Quartz was selected instead of stainless-steel for the heater tube material because its thermal expansion coefficient is 23.6 times lower than that for stainless-steel, resulting in much smaller sample height increases during heating. The stainless-steel button 0.3 mm backing thickness facilitated efficient heat transfer from the heated purge gas, through the button, and to the sample with minimal vertical thermal expansion. The K-type thermocouple wires placed in contact with the top of the sample were extended about 6 mm from the end of the 1.6 mm (1/16") diameter ceramic insulator to

minimize infrared source radiation blocking. Sample heating from the FTIR infrared radiation source resulted in a typical ambient sample temperature of about 30 ^{o}C.

The heating profile applied to the homogenized neat kaolinite sample during VT-DRIFTS measurements consisted of two isothermal periods and heating and cooling ramps. The initial one-minute isothermal period at ambient temperature was followed by a heating ramp to 150 ^{o}C at a rate of 2 ^{o}C/min temperature increase. The second isothermal period was held at 150 ^{o}C for five-minutes. The cooling ramp back down to near ambient temperature was then initiated at a rate of 2 ^{o}C/min. This symmetrical heating and cooling temperature profile was used to distinguish between reversible and irreversible temperature-dependent changes in different hydroxyl groups and overall kaolinite structure. For reversible kaolinite structure variations, changes to spectral bands observed during heating were reversed during cooling. Irreversible changes were not observable in the ambient temperature spectra after the sample went through the heating and cooling profile.

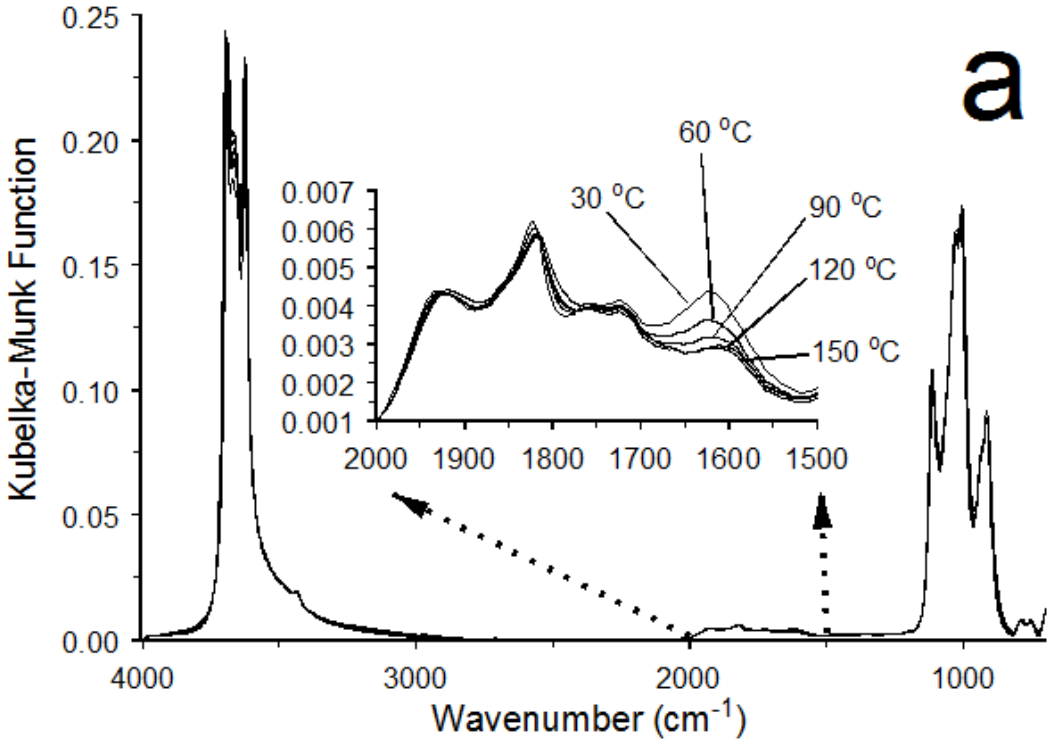
a
Kubelka-Munk Function
Wavenumber (cm-1)
30 °C
60 °C
90 °C
120 °C
150 °C

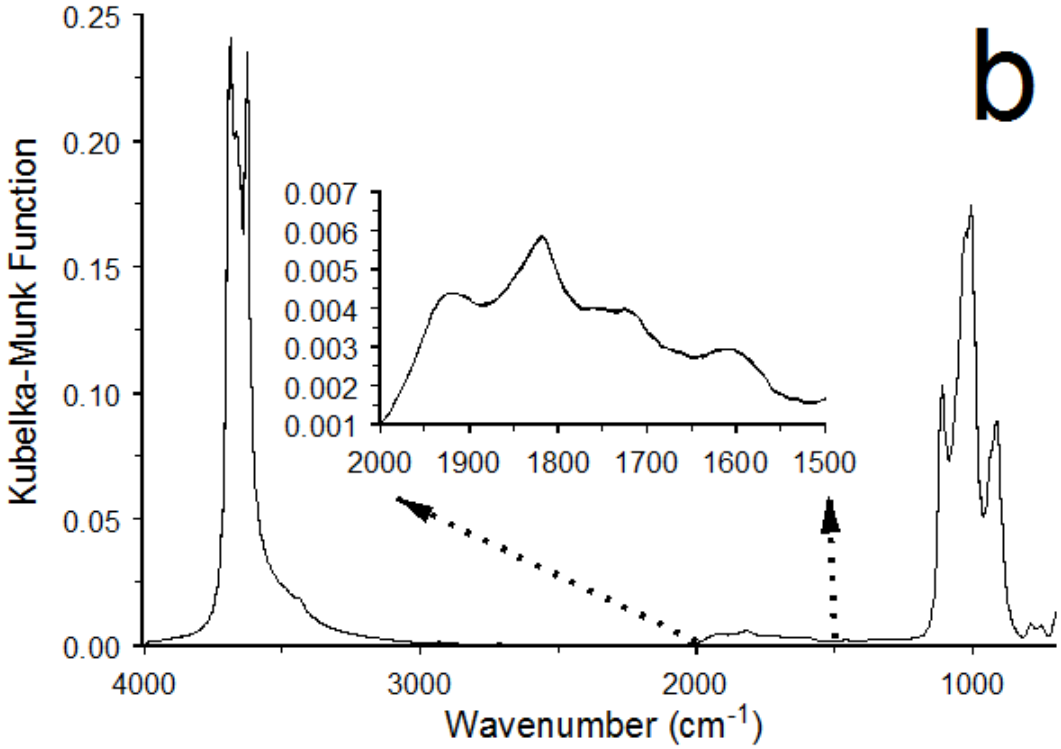
b
Kubelka-Munk Function
Wavenumber (cm-1)

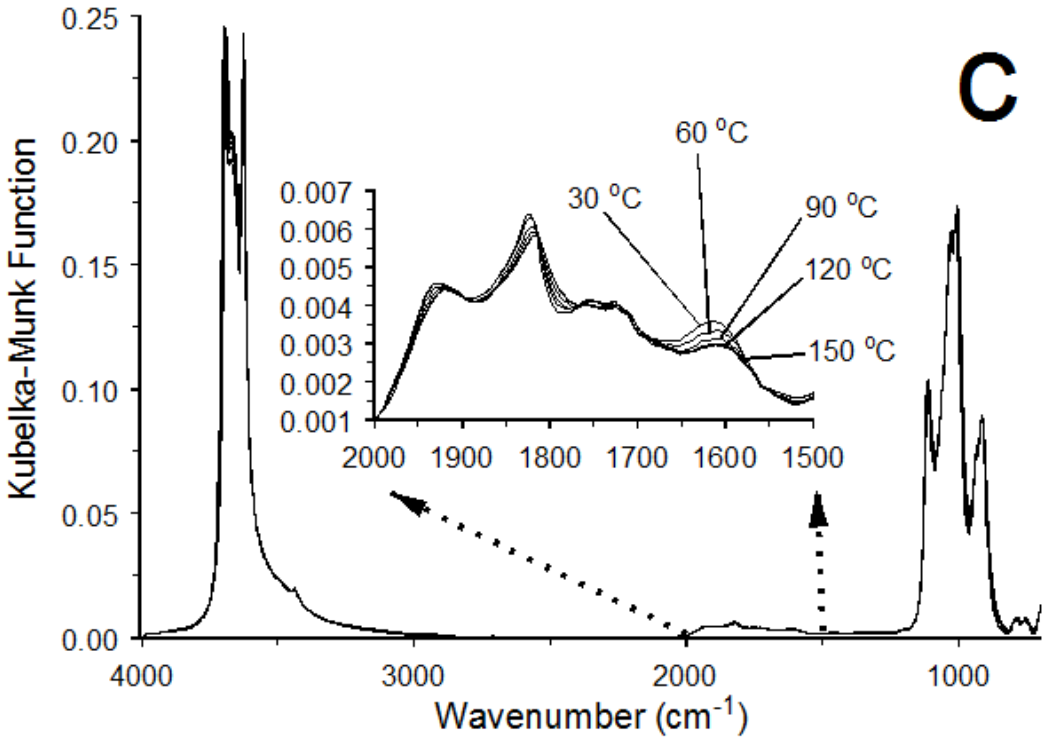

Figure 3.3: (a) Overlay of infrared spectra measured while heating. (b) Overlay of five infrared spectra measured at 150 °C. (c) Overlay of infrared spectra measured while cooling.

VT-DRIFTS infrared spectra acquired at 30 °C sample temperature increments while heating to 150 °C are overlaid in Figure 3.3a. Slight changes in overlapping spectra are evident, with greater variability in the O-H stretching vibration bands (> 3500 cm^{-1}) compared to the fingerprint region (800-1200 cm^{-1}). The magnified 1500-2000 cm^{-1} region reveals a decrease in intensity near 1620 cm^{-1} with increasing temperature, representing a decrease in the H-O-H bending vibration band intensity caused by the loss of adsorbed water. Compared to Figure 3.3a, little variability is evident in Figure 3.3b, which depicts an overlay of the five

consecutively measured infrared spectra obtained during the 150 ^{o}C isothermal period. These five spectra are indistinguishable on the displayed scale, even within the magnified 1500-2000 cm^{-1} region, which represents a 35x ordinate scale expansion compared to the full spectrum plots. This confirms that the kaolinite structure was invariant during the 150 ^{o}C isothermal temperature period. The fact that reproducible spectra were obtained during this portion of the heating profile also confirms that constant sample temperatures were maintained during these measurements. Figure 3.3c, which shows overlaid VT-DRIFTS spectra obtained at 30 ^{o}C temperature increments during sample cooling, is qualitatively similar to Figure 3.3a, except that the 1620 cm^{-1} band did not fully regain its initial intensity after cooling. Results shown in Figure 3.3 suggest that most of the kaolinite structural changes caused by sample heating were reversible, except for adsorbed water loss, which was mostly irreversible.

The inset plots in Figure 3.3 reveal small temperature-dependent intensity changes near 1620 cm^{-1}, assigned to loss of H-O-H bending vibrations due to water evaporation. Figure 3.4 shows the 1560-1660 cm^{-1} integrated area versus time plot for this band derived from VT-DRIFTS spectra. The dash line depicts measured sample temperatures as a function of elapsed time. The straight lines between 0 and 40 min and 70 and 120 min represent linear regressions for the integrated area versus time plots over those periods. The decreasing band area began to level off near 40 min, when the sample temperature was about 109 ^{o}C.

Between 0 and 40 min, the best fit line equation, which represents measurement sensitivity, was: $y = -0.0026 x + 0.37$ ($R^2 = 0.97$), where y is integrated band area and x is time (min). During sample cooling, the integrated area increased slightly, but did not return to its initial value. The best fit line equation between 70 and 120 min was: $y = 0.0006 x + 0.22$ ($R^2 = 0.91$). The lack of complete reversibility evident in Figure 3.4 was expected due to the low water content of the dry air spectrophotometer purge gas. Thermogravimetric analysis of the kaolinite revealed that it contained about 1.5% (w/w) water. The plot in Figure 3.4 confirms that measurement sensitivity was sufficient to reveal the expected trends in the water bending vibration band area as a function of temperature. Given that the amount of sample placed in the button sample holder was at most 1 mg and that the incident infrared beam focal point diameter was approximately 3 mm[175], the total water mass loss contributing to changes in acquired VT-DRIFTS spectra can be estimated to be about 3 µg. Therefore, on average, successive VT-DRIFTS spectra collected over the 0-40 min elapsed time reflected a water loss of about 75 ng for each 2 °C increase in sample temperature. Similarly, spectra collected between 70 and 120 min reflected average gains of about 19 ng per each 2 °C decrease in sample temperature.

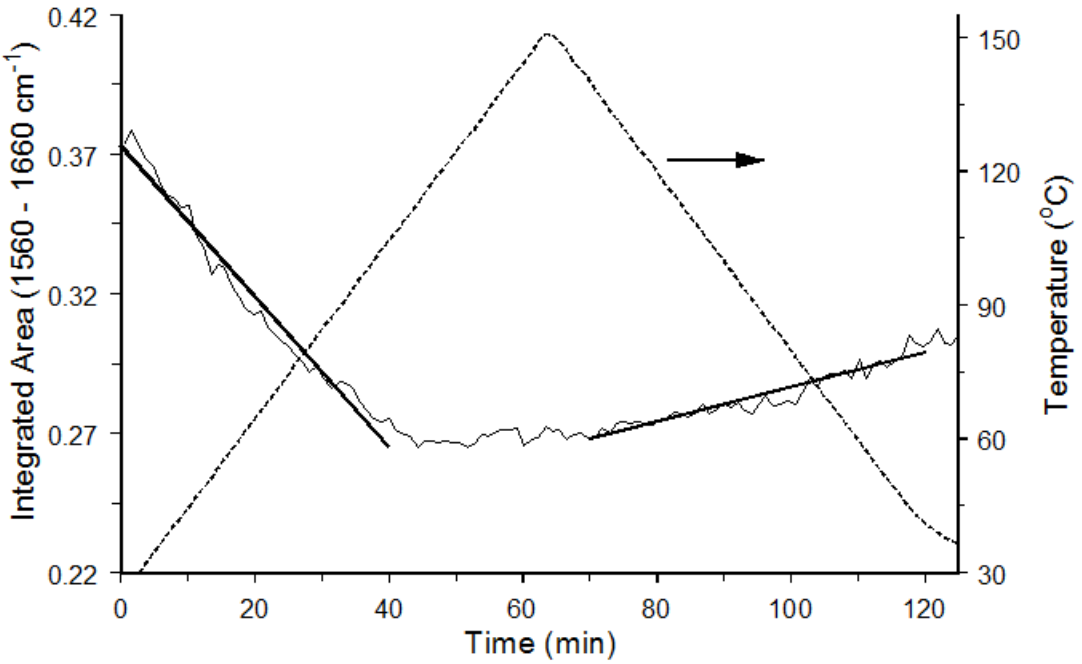

Figure 3.4: Integrated absorbance for the adsorbed water H-O-H bending vibration band (solid line) and sample temperature (dash line) as a function of time. Straight lines denote linear regression best fit lines.

The overall infrared spectrum changes that occurred while heating the kaolinite sample and isothermal successive scan reproducibility are represented in Figure 3.5. In the upper portion, three successively measured spectra obtained near the ambient temperature of 30 °C and three successively measured spectra obtained near the heated isothermal temperature of 150 °C are shown for the O-H stretching vibration (3725-3600 cm^{-1}) and bulk mineral vibration (1150-900 cm^{-1}) spectral regions. With the exception of the band near 3620 cm^{-1}, bands in 150 °C spectra are shifted to lower wavenumbers compared to the 30 °C spectra. Solid

lines are overlays of the final three spectra obtained during sample cooling. Temperatures during these measurements averaged 33.3 ^{o}C with a standard deviation of ± 0.4 ^{o}C. Dash lines represent three spectra obtained during the 150 ^{o}C isothermal period. The average temperature for these measurements was 150.1 ^{o}C, with a standard deviation of ± 0.8 ^{o}C. The solid and dash lines at the bottom of Figure 3.5 indicate the variability of successively measured spectrum intensities, represented by plots of relative standard deviation (RSD) as a function of wavenumber. Because RSD values were small, the six spectra in the upper portion of Figure 3.5 appear as only two plots. In general, RSD values were slightly greater at 150 ^{o}C compared to those at 30 ^{o}C. RSD values never exceeded 1.0 % at either temperature and were below 0.5 % over most of the spectral range shown. This compares favorably with the scan-to-scan reproducibility of the instrument at ambient temperature (i.e. without heating), which was characterized by RSD values ranging between 0.1 and 0.2 % under the same data collection conditions.

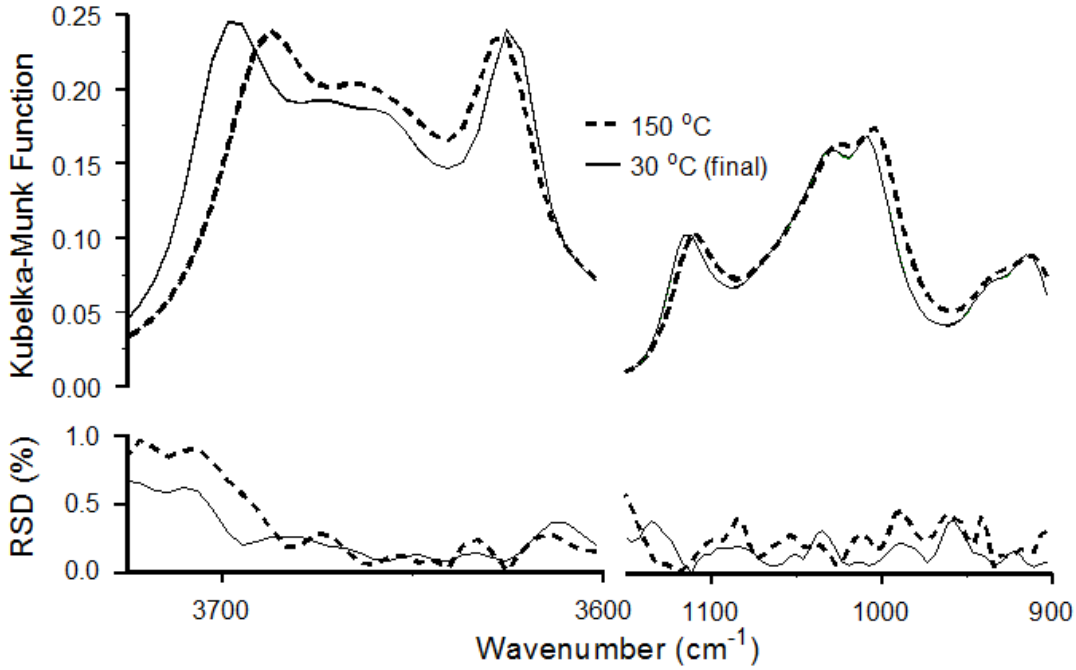

Figure 3.5: Top: DRIFTS spectra for kaolinite measured at 30 and 150 °C. Bottom: Relative standard deviations of measured intensities for three successively acquired spectra as a function of wavenumber.

Hydrogen bonding and electrostatic interactions between water, hydroxyl groups, and bridging oxygens are responsible for many of kaolinite's physical properties. When heated above 100 °C, kaolinite loses weakly bonded molecular water. Reduction in basal spacing due to heating increases hydroxyl group-oxygen interactions between sheets, resulting in systematic shifts in hydroxyl stretching band wavenumbers.[158] Difference spectra, obtained by subtracting spectra obtained at two temperatures, reveal subtle changes that are not readily apparent in the measured spectra. For example, Figure 3.6a shows the ambient temperature

O-H stretching vibration region of kaolinite (top) and a series of difference spectra (bottom) representing changes that occurred during heating (down arrow) and cooling (up arrow). Solid lines represent the results of subtracting the initial ambient temperature spectrum from spectra obtained at 30 °C increasing temperature increments, whereas dashed lines were obtained by subtracting the 150 °C spectrum from spectra obtained during cooling at 30 °C intervals. For reference, vertical lines denote band maxima locations in the initial ambient temperature spectrum. The four hydroxyl stretching vibration band locations agree with those reported in several previous studies.[150, 157, 176-177]

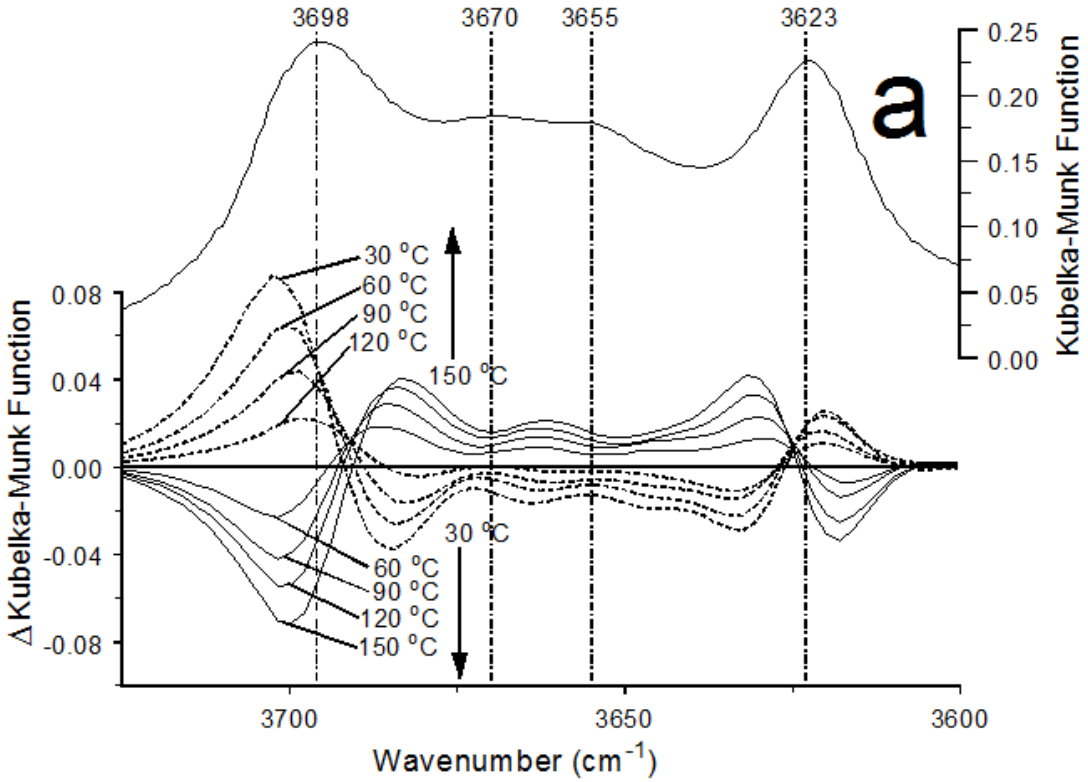

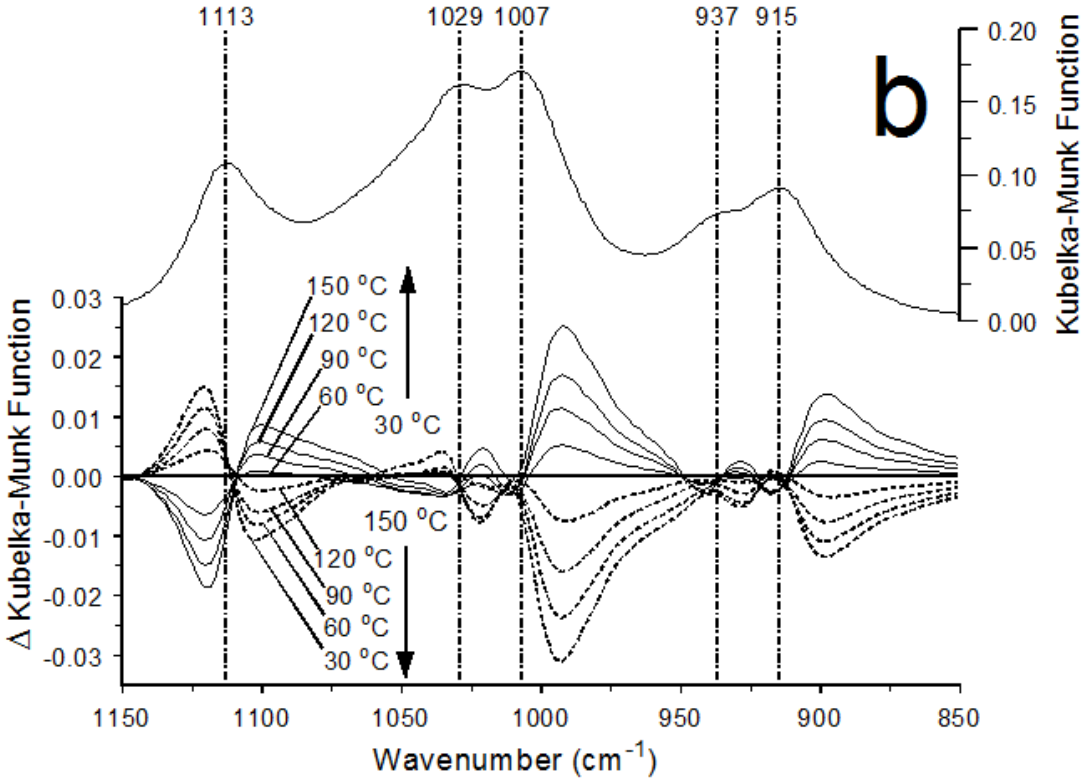

Figure 3.6: (Top) VT-DRIFTS spectra obtained at 30 °C and (Bottom) difference spectra for (a) O-H stretching vibrations and (b) framework vibrations.

Temperature labels at the base of the up and down arrows denote the reference temperatures for spectrum subtractions. Individual difference spectrum labels identify the other spectrum used for subtraction. For example, the 60 °C solid line difference spectrum was obtained by subtracting the initially measured 30 °C spectrum from the spectrum obtained at 60 °C during sample heating and the 120 °C dash line was obtained by subtracting the 150 °C spectrum from the spectrum measured at 120 °C while the sample was cooling. For each difference spectrum, positive features denote gain of intensity whereas negative features

reflect intensity loss over the temperature increment associated with subtracted spectra. When heated, kaolinite structural changes resulted in a shift of the 3698 cm^{-1} band to lower wavenumber and a shift of the 3623 cm^{-1} band to higher wavenumber (Figure 3.5). This is consistent with a previous study that employed Raman microprobe measurements to monitor kaolinite as a function of temperature.[158] Frost et al. reported a blue shift of the inner hydroxyl band and a red shift of the inner surface hydroxyl band.[158] Figure 6a solid line difference spectra exhibit negative intensities above 3690 cm^{-1} and smaller positive features below 3690 cm^{-1}. The relative areas of the positive and negative residuals differ because the overall integrated area for this band decreased when the sample was heated. In contrast, the 3623 cm^{-1} band integrated area increased slightly with heating, as indicated by a somewhat greater gain in intensity above 3625 cm^{-1} compared to the intensity lost at lower wavenumbers. In general, the solid and dash line difference spectra are nearly mirror images, but close inspection reveals some slight variations. For example, although the difference spectrum maximum absorbance change for the 3698 cm^{-1} band shifted from 3702 to 3700 cm^{-1} during sample heating (solid lines), maxima began at 3696 cm^{-1} and ended at 3702 cm^{-1} during cooling. Similar trends with shifts in the opposite direction were exhibited by the 3623 cm^{-1} band. These trends result from variations in hydroxyl group local environments and are likely caused by temperature-dependent changes in hydrogen bonding between hydroxyl functionalities and neighboring framework

oxygens. Intensities for the heavily overlapping 3670 and 3655 cm^{-1} bands increased slightly due to heating. The approximately mirror image dash line difference spectrum features for these bands indicate that these changes were effectively reversed by sample cooling.

Inner hydroxyls (3623 cm^{-1}) are located between the silica and alumina sheets.[157] Thermal expansion increases distances between inner hydroxyls and neighboring apical oxygens. This decreases hydrogen bonding strengths, resulting in shorter hydroxyl O-H bonds, causing the stretching vibration band to shift to higher wavenumber. Inner surface hydroxyls are located on the outside of the octahedral alumina sheets. This configuration results in weak hydrogen bonding with siloxane sheet oxygens and more freedom of movement of the hydroxyl groups, resulting in higher O-H stretching vibration band wavenumbers compared to inner hydroxyls.[155, 177] When heated, alumina and siloxane sheets move closer together, strengthening hydrogen bond interactions for inner-surface hydroxyl groups and lengthening their O-H bonds.[158] Tosoni et al. proposed that shorter distances between alumina and siloxane sheets result in more linear O-H—O hydrogen bond angles, causing the observed red shifts of the inner surface hydroxyl O-H stretching vibration bands.[159]

Figure 3.6b shows difference spectra spanning the 1150-850 cm^{-1} range, which includes Si-O-Si stretching and Al-O-H bending vibrations. The band at 1113 cm^{-1} has been assigned to Si-O-Si symmetrical stretching of equatorial bonds

whereas the 1029 and 1007 cm^{-1} bands have been assigned to anti-symmetric stretching motions.[178] The 937 cm^{-1} band is associated with Al-OH bending of inner surface hydroxyls whereas the 915 cm^{-1} band is attributed to the Al-OH bending vibration of inner hydroxyls.[177] Solid line difference spectra represent changes that occurred while heating the sample and the dash lines represent subsequent cooling changes. Like Figure 3.6a, these plots are nearly symmetrical about the horizontal axis, which is consistent with thermally reversible changes. The magnitudes and shapes of difference spectra bands reveal subtle details regarding temperature-dependent local environment changes for these functionalities. The Si-O-Si stretching vibration bands all exhibited red shifts with increasing temperatures. Interestingly, the 1113 cm^{-1} band positive difference spectrum component was broader than the negative component. This indicates that the Si-O-Si functionalities affected by heating adopted a less uniform structure compared to their initial ambient temperature configurations. Compared to the 1113 cm^{-1} band, the 1029 cm^{-1} band change was minimal, but the 1007 cm^{-1} band changes were significantly larger. These differences reflect variations in the dipole moment changes associated with the different vibration modes. Difference spectra show that temperature-dependent intensity changes near the 937 cm^{-1} Al-OH bending vibration band were smaller and confined to a narrower wavenumber range than the Si-O-Si vibrations. Similarly, very little intensity decrease was detected near the 915 cm^{-1} band, but a significant, broad intensity increase at lower

wavenumbers was observed. The shapes of positive difference spectra bands below 915 cm^{-1} resemble those for the Si-O-Si stretching vibrations, and they are most likely associated with a red shift and intensity increase for Si-O-Si framework vibrations that were located near the Al-OH bending vibration bands at ambient temperature.[147, 156]

Figure 3.7a shows the temperature-dependent shifting of the 3698 cm^{-1} (at ambient temperature) band. The band center wavenumber shifted lower by about 8 cm^{-1} when the sample reached 150 ^{o}C, then returned to about the same wavenumber after cooling. This symmetrical temperature profile is consistent with a reversible change for the hydroxyl functionalities responsible for this vibration. The Figure 3.6a plots indicate that band intensity was lost above 3690 cm^{-1} and gained below 3690 cm^{-1} when the kaolinite sample was heated.

Band area as a function of temperature plots shown in Figure 3.7b were obtained by integrating VT-DRIFTS spectra over the indicated wavenumber regions, which corresponded to the positive and negative residuals in difference spectra. Intensity loss and gain profiles were not well correlated. Intensity loss above 3690 cm^{-1} exhibited a steeper decline whereas the intensity gain was more gradual. The fact that these plots were not mirror images suggests that the hydroxyl groups affected by heating adopted more diverse orientations compared to their ambient temperature configurations.

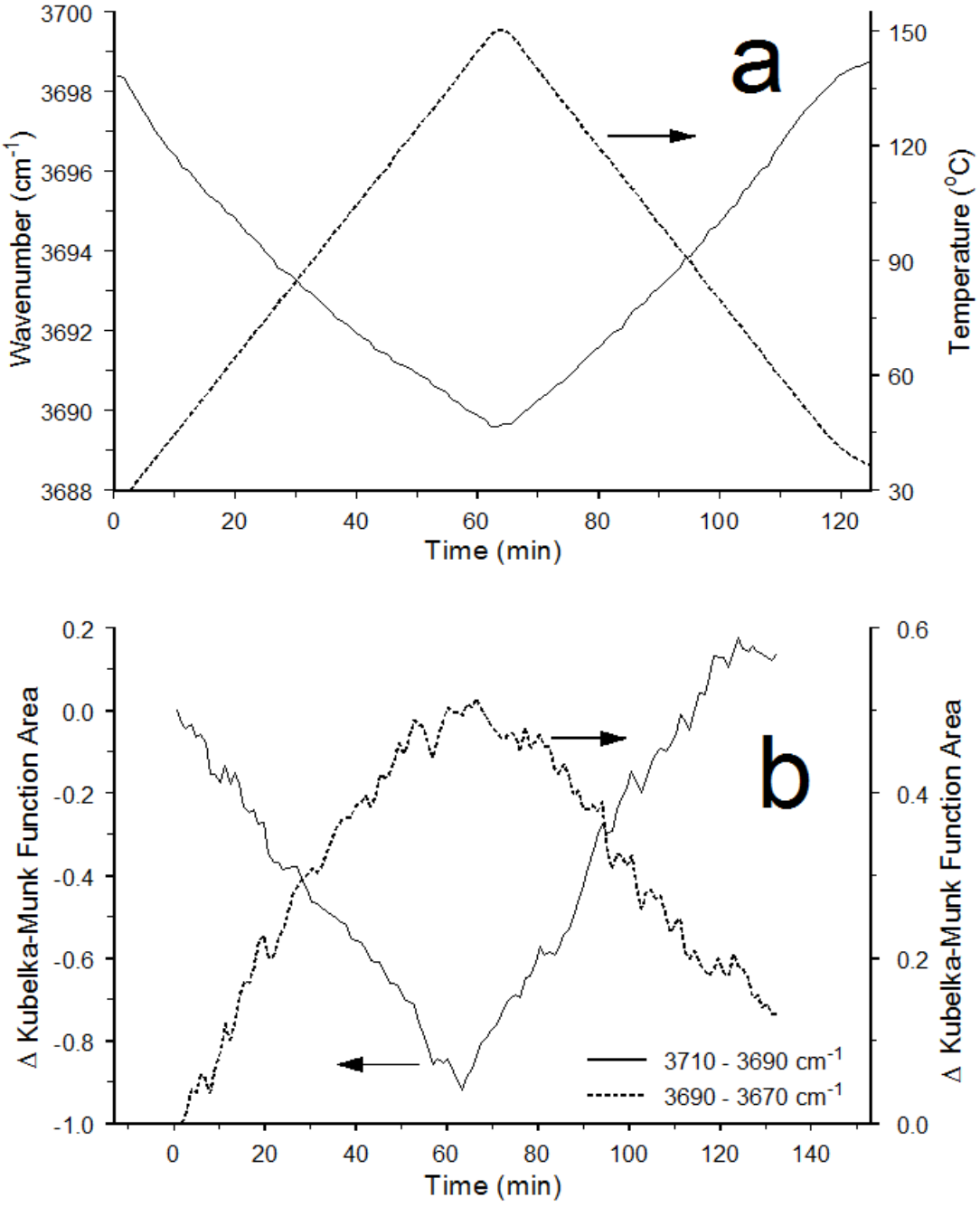

Figure 3.7: (a) VT-DRIFTS Band maximum location and (b) integrated band area variations as a function of time for the 3698 cm^{-1} (at 30 °C) O-H stretching vibration. Sample temperatures are denoted by the dash line in (a).

Figure 3.8 shows temperature-dependent band center shifting and integrated band area changes for the 3623 cm^{-1} vibration band. The band center wavenumber increased by about 3 cm^{-1} with heating, but only shifted back 2 cm^{-1} after sample cooling (Figure 3.8a). Figure 3.8b shows that band area changes were less than for the 3698 cm^{-1} band (Figure 3.7b). In contrast to the 3698 cm^{-1} band, the 3623 cm^{-1} integrated band area increased with sample heating. Clearly, structural changes causing the band shift for this hydroxyl functionality were significantly different from those responsible for the 3698 cm^{-1} band changes. This was expected because the 3623 cm^{-1} band is associated with inner hydroxyls whereas the 3698 cm^{-1} band represents inner surface hydroxyls, which occupy significantly different local environments.

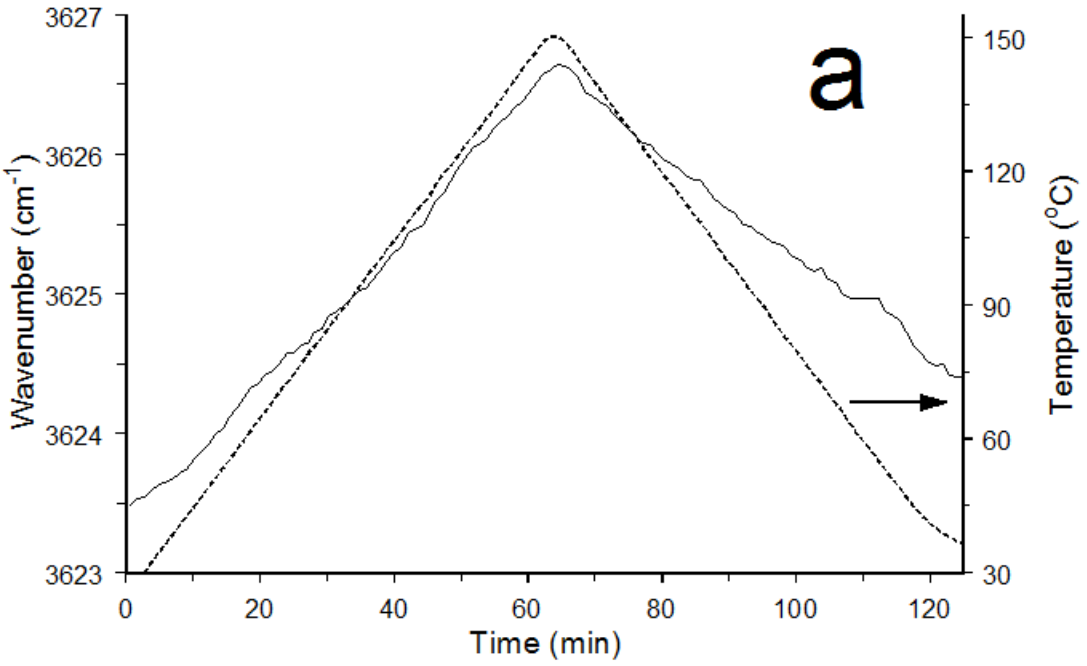

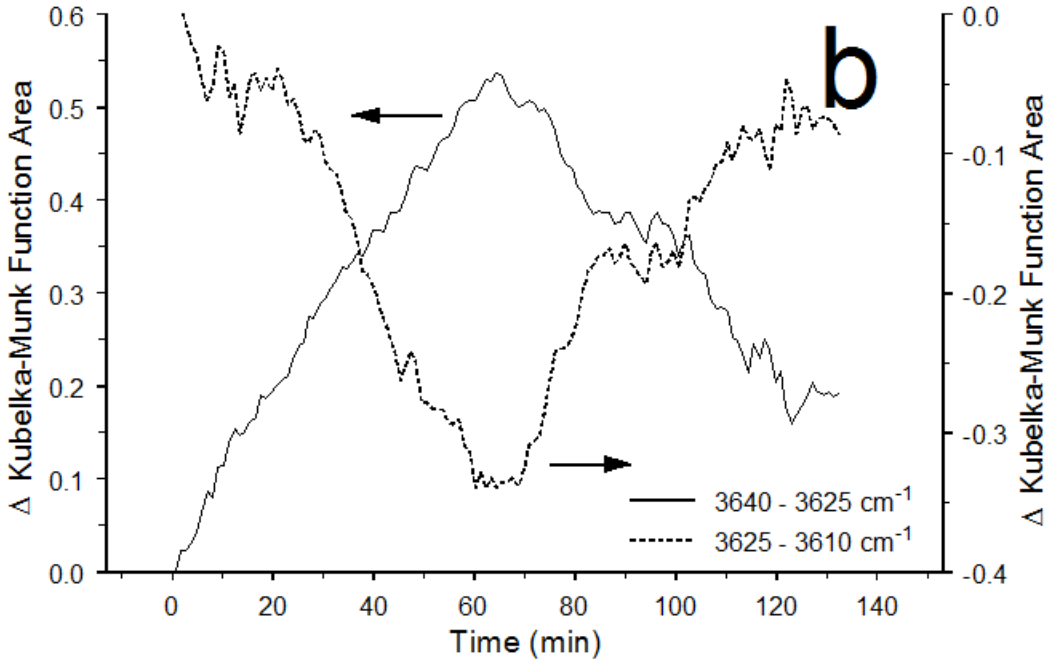

Figure 3.8: (a) VT-DRIFTS Band maximum location and (b) integrated band area variations as a function of time for the 3623 cm^{-1} (at 30 ^{o}C) O-H stretching vibration. Sample temperatures are denoted by the dash line in (a).

Results described here are consistent with previous vibrational spectroscopy kaolinite studies, which primarily focused on the hydroxyl stretching and bending vibration bands. In addition to the previously published temperature-dependent trends in band locations, intensities, and widths of hydroxyl group vibrations, the VT-DRIFTS method introduced here provides detailed, high signal-to-noise ratio difference spectra revealing complex band shape changes with temperature. As shown in Figure 3.6, the new method also provides information regarding framework vibration band shape variations. Although framework difference spectrum features have similar shapes, they vary significantly in

intensity. The temperature-dependent band shifting and broadening evident in Figure 3.6 was caused by subtle changes in kaolinite unit cell configurations caused by heating. By using a sample heating profile that includes controlled temperature increase and decrease, the reversibility of temperature-dependent changes was assessed. For example, a small quantity of adsorbed water (< 1 % w/w) during sample cooling (Figure 3.4) and annealing differences for hydroxyl groups in different locations (Figures 3.7 and 3.8) were detected.

Unlike the results described here, previous DRIFTS kaolinite studies were obtained by using diluted samples. For example, Drits, et al. employed a 5% w/w mixture of kaolinite in KBr for infrared spectroscopic measurements of the clay heated to various temperatures.[167] Unfortunately, infrared transparent salts can interact with kaolinite, affecting vibration frequencies and therefore providing questionable measurement accuracies. For example, Miller et al. found that grinding kaolinite with KBr drastically altered the intensities of the O-H stretching vibration bands.[179] They attributed these intensity shifts to prototropy, in which basal hydroxyl protons were more strongly attracted to apical oxygens than to their neighboring basal oxygen during the early stages of grinding.[179] They later noted that increasing the grinding pressure and time in the presence of KBr altered the relative ratios of the O-H stretching vibration peak intensities.[180] Thus, in addition to providing improved sensitivity, the VT-DRIFTS technique described here likely

provides greater measurement accuracy by virtue of the fact that sample dilution in an infrared transparent salt was not required.

3.4. Conclusions

The design shown in Figure 3.1 offers significantly higher optical throughput when compared to commercially available environmental chamber designs. The ability to analyze neat samples with this increased optical throughput provides greater sensitivity and lower detection limits compared to other designs. The main tradeoff for these improvements is the temperature range. Sample heating was limited to 150 ^{o}C to avoid oxidation of the stainless-steel sample holder. The button sample holder used for the studies described here has been employed for numerous other studies over a period of several years without showing signs of oxidation. The 150 ^{o}C temperature limit was sufficient to facilitate previous zeolite dehydration studies.[172-174] Because heating occurs in CO_2-free dry air spectrophotometer purge, easily oxidized samples may not be suitable for studies because of the presence of atmospheric oxygen.

VT-DRIFTS spectra obtained during kaolinite heating from ambient temperature to 150 ^{o}C reveal small reversible structural changes that are consistent with previously published studies. Although band intensity associated with the O-H stretching vibration of adsorbed water was obscured by intense kaolinite hydroxyl group vibrations, the H-O-H bending vibration, which can be unequivocally attributed to water, could be used to selectively monitor clay thermal

dehydration and subsequent re-hydration processes with a sensitivity sufficient to detect nanogram mass changes between successively acquired spectra. Difference spectrum residuals provided information regarding simultaneous band shifting and broadening caused by temperature-dependent unit cell variations. Comparing residuals calculated from spectra obtained during sample heating with those obtained while cooling provided a means for assessing the reversibility of these structural changes. For kaolinite silica sheet vibration bands, these small changes were found to be reversible, resulting in a high degree of symmetry between positive and negative residual trends. In contrast, positive and negative residuals for inner and inner surface hydroxyl group stretching vibration band shapes were somewhat different, likely due to different annealing processes during sample cooling.

The scan-to-scan reproducibility afforded by the button VT-DRIFTS method facilitates detection of subtle temperature-dependent sample structure changes – both reversible and irreversible. When spectra of the same sample at the same temperature are overlaid, these minute temperature-dependent structural changes are often imperceivable. However, by using the button VT-DRIFTS system, real-time sample structural changes that occur over small temperatures can be detected. Scan-to-scan relative standard deviations for isothermal measurements at 30 and 150 ^{o}C were found to be less than 1.0 % and were slightly higher than those for ambient temperature reproducibility. These highly reproducible

measurements enable a more accurate elucidation of temperature-dependent sample structure changes. Infrared spectrum band location and shape variations provide information regarding sample structure changes at an atomic level. An improved interpretation of temperature-dependent kaolinite structure changes may be obtained by comparing VT-DRIFTS measurements with predicted changes derived from computational modeling of fundamental vibration modes based on anticipated structure variations. Nonetheless, the improved VT-DRIFTS sensitivity and reproducibility demonstrated here should enable detailed analyses of other minerals and solid-state samples.

Chapter 4: Diffuse Reflectance Infrared Studies of Minerals

4.1 Introduction

Infrared spectroscopy is one of many analysis tools used to characterize minerals.[181] This non-destructive method is employed to characterize bulk samples and confirm the presence of specific mineral types in heterogeneous mixtures.[182-184] This is accomplished by identifying infrared spectrum vibration bands that are characteristic of the functional groups possessed by mineral constituents. For example, by using alkali salt pellets of sediments and transmission spectroscopy, Craddock et al. found that quantitative mineral assays based on functional group infrared spectroscopy could rival and exceed the performance of X-ray diffraction analyses.[185]

Qualitative and quantitative infrared spectroscopy analyses can be difficult due to the complexity of the measured spectra. An infrared spectrum contains information regarding all infrared active sample vibrations within the wavenumber range scanned. Unfortunately, although spectra typically contain information related to a wide range of sample properties, functional group specific vibration bands often overlap, making them difficult to isolate and quantify. In addition, spectrum variabilities introduced by the inability to prepare samples with the same absorption and reflection properties diminish the accuracy and precision of analyses based on calibration curves.[181] These issues are circumvented when sample perturbation analysis techniques are employed. In these methodologies,

perturbation is applied that alters the sample properties. The resulting structure changes cause characteristic infrared spectrum band variations. These variations are revealed by subtracting a reference spectrum obtained before the sample was perturbed. Spectrum features that do not change cancel in the subtraction result, leaving only those vibration bands that were affected by the perturbation. Because the same sample is employed to obtain the infrared spectra measured before and after the perturbation, spectral artifacts related to inconsistent sample loadings are avoided.

Infrared spectra typically contain highly overlapping absorbance bands representing various sample vibrations and their linear combinations. Often, specific arrangements of atoms within a molecule (i.e., functional groups) are responsible for most of the dipole moment fluctuations that occur during infrared active vibrations. Sample perturbations can alter molecular bond lengths and angles, resulting in vibration band shape changes. Temperature change is a commonly employed sample perturbation approach that facilitates energy transfers between the sample and its environment. Previous variable temperature infrared spectroscopy studies have been carried out by using a variety of different spectroscopic methodologies. For example, while uniformly heating thin films and pellets, transmission spectroscopy measurements have been used to obtain temperature-dependent infrared spectra.[186-187] Infrared spectra for reflective solid samples were acquired as a function of temperature by using reflectance

spectroscopy measurements.[144] Variable temperature attenuated total reflectance (ATR) infrared spectroscopy measurements have been made by adjusting the temperature of the high refractive index ATR crystal. This is usually accomplished by placing the crystal in contact with a heating/cooling block.[188-189]

Recently, variable temperature infrared spectroscopy studies were demonstrated by using diffuse reflection and a button sample holder.[190] Figure 4.1 shows a photograph of two button sample holders. The conventional button (left) consists of a stainless-steel base to which stainless-steel wire mesh is welded.[113] The wire mesh contains small cavities into which samples can be loaded. Thin layers of powders consisting of irregularly shaped particles are placed into these cavities. The powder effectively scatters infrared radiation, necessitating the use of diffuse reflection infrared spectroscopy for analyses. The small size, flat bottom, and high thermal conductivity of the button sample holder make it compatible with sample heating and cooling by using flat-surface piezoelectric (thermoelectric) chips. The right button in Figure 4.1 was modified to provide sample temperature measurements by placing a thermocouple beneath the wire mesh. [74, 116, 191] When the modified button was placed on top of stacked thermoelectric chips, sample heating and cooling rates exceeding 2 °C/s were achieved over a 0–150 °C temperature range, and isothermal temperatures could be maintained to within ±0.1 °C.[74, 116, 191]

Diffuse reflection infrared Fourier transform spectroscopy (DRIFTS) is applicable to materials that scatter infrared radiation. It is well suited for mid-infrared spectroscopic analyses of mineral powders.[105, 192] In addition to the scattering coefficient, diffuse reflectivity is determined by wavelength-dependent sample absorptivity and the cumulative distance that infrared radiation passes through the irregularly shaped particles.[193-195] When absorptivity is too high, near-zero reflectance is recorded. The resulting "bottomed-out" reflectance spectrum bands provide no useful sample information. Wavelength regions of high absorptivity may also exhibit the Reststrahlen effect,[196-197] wherein band shape distortions appear near absorbance maxima. Diluting sample powders with non-absorbing alkali salts can minimize these spectral artifacts. The diluent isolates particles and reduces the amount of sample material exposed to radiation. Alternatively, average radiation path lengths can be reduced by employing a button sample holder and thin powder layers.[113] With this approach, spectrum artifacts caused by interactions between the sample and diluent are avoided. This is particularly advantageous for temperature perturbation studies because the addition of a diluent to a sample can significantly alter the thermal properties under scrutiny.

The International Mineralogical Association (IMA) recognizes over 6000 different minerals that are found throughout the Earth's lithosphere and mantle.[198] Minerals are defined as "naturally occurring homogenous solids with definite

chemical compositions and a highly ordered atomic arrangement typically formed through inorganic processes." This chapter describes applications of a unique button sample holder apparatus for mineral studies by temperature perturbation infrared spectroscopy. Examples of using the variable temperature infrared spectroscopy apparatus are described for the following: a crystalline mineral (α-quartz), three minerals that contain removable water bound by different interactions (silica gel, montmorillonite clay, gypsum), and two low-rank coals containing different quantities of organic constituents.

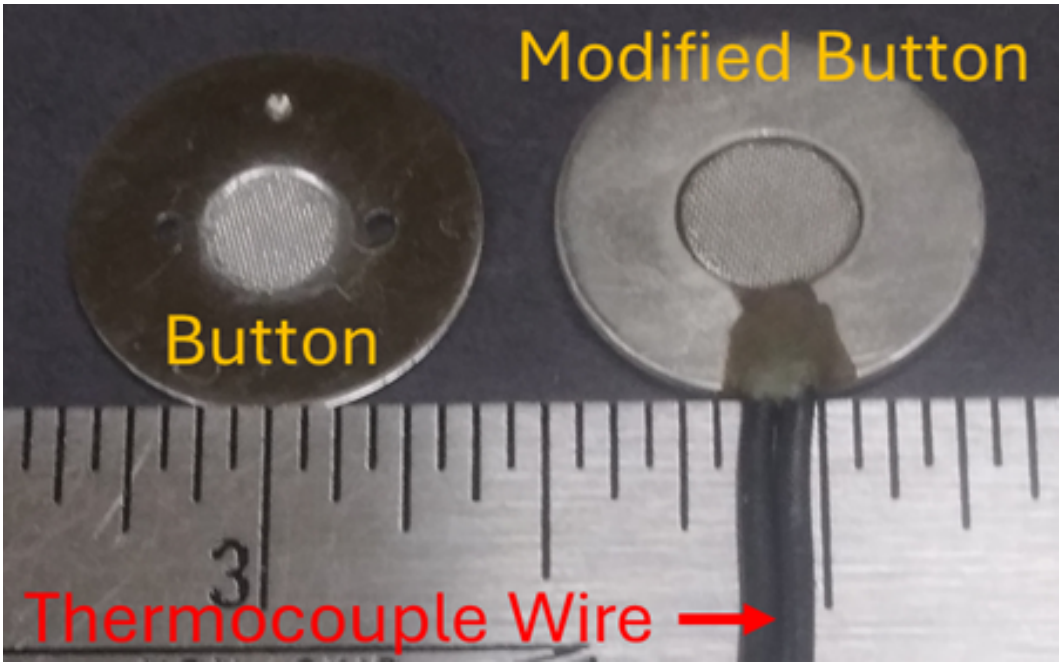

Figure 4.1: Photograph of a conventional button (left) and the modified button (right).

4.2 Apparatus

A button consists of a 0.75 in (19 mm) diameter stainless-steel backing with stainless-steel wire mesh spot welded to the well indentation at its center (Figure 4.1). Thin layers of powdered samples are formed within the void spaces of the wire mesh by applying a small amount of sample to the mesh and brushing off the surface particles. The flat polished bottom of the high-thermal-conductivity metal button facilitates precise temperature control when it is mounted on a Peltier thermoelectric device. The modified button incorporating an attached thermocouple (Figure 4.1 right) was employed for the variable temperature infrared spectroscopy measurements discussed here. Figure 4.2 shows the modified button mounted on the Peltier thermoelectric stack heating and cooling apparatus. The construction and performance of this apparatus are described in detail in Chapter 2.[199-200] Rapid heating and cooling rates were achieved by using two stacked thermoelectric chips (TECs), which were tightly encased inside the metal housing shown in Figure 4.2.[117-118] Sample temperatures were adjusted by controlling the heat transferred between the upper and lower TECs.

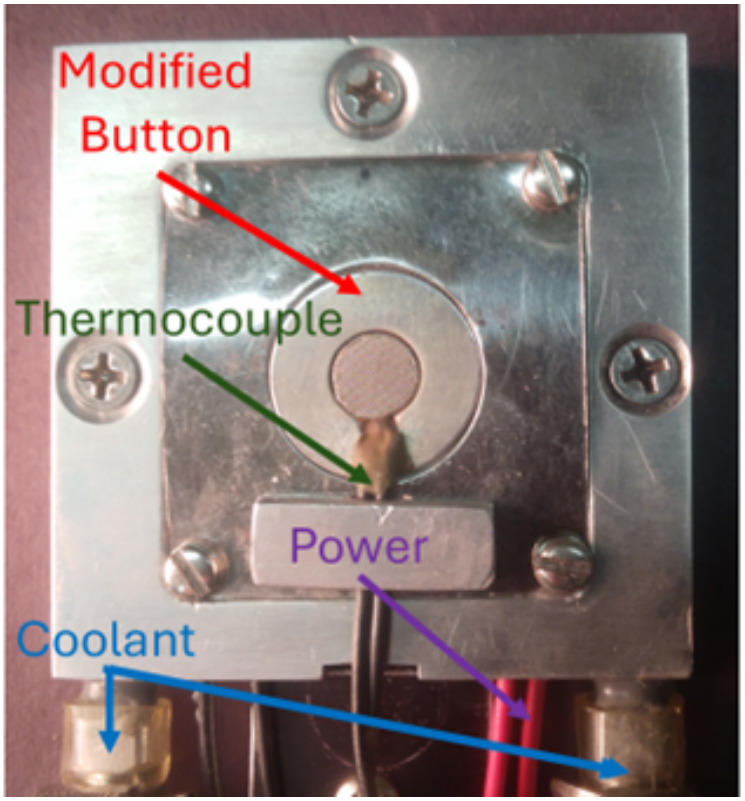

Figure 4.2: Top view of the sample heating/cooling apparatus.

A Mattson Instruments Inc. (Madison, WI, USA) Nova Cygni 120 Fourier transform infrared spectrophotometer (FTIR) and a Harrick Scientific Inc. (Pleasantville, NY, USA) praying mantis diffuse reflection accessory[105] were used for variable temperature diffuse reflection infrared spectroscopy (VT-DRIFTS) measurements. Spectra were measured under a dry air instrument purge that provided a 0.16 kPa p(H_2O) humidity environment. Spectra were obtained over the 4000–650 cm^{-1} range at 8 cm^{-1} resolution by signal averaging 64 interferograms, requiring about 30 seconds, for both sample and background single beam measurements. Background spectra were obtained with the empty modified button

prior to sample loading. Although measurements were made at 8 cm^{-1} resolution, interferogram zero filling prior to processing yielded a 0.97 cm^{-1} spectrum digitization interval. This was found to provide reproducible infrared band shapes and yielded a superior signal-to-noise ratio compared to measurements made at 4 cm^{-1} resolution.[175] Reflectance spectrum baseline offsets and slopes were removed by using macro programs to apply the same correction methodologies to all of the spectra acquired during the VT-DRIFTS analyses.[109] Spectra were converted to a form that was proportional to the analyte concentration by using the Kubelka–Munk transformation.[129]

4.3 Temperature versus Time Profiles

The precise sample temperature control and rapid heating and cooling afforded by the apparatus in Figure 2 facilitated the application of different temperature versus time programs during temperature perturbation analyses (Figure 4.3). The plot in Figure 4.3a shows a linear sample heating ramp immediately followed by an optional linear cooling ramp. Infrared spectra are continuously collected while the sample temperature is constantly changing. This profile is useful for accurately determining the temperatures at which specific sample changes occur. Each spectrum is measured over a sample temperature range determined by the heating/cooling rates and the number of signal-averaged interferograms acquired for each spectrum. Typically, sample temperatures are increased or decreased at 1–2 °C/min while repeatedly signal averaging

interferograms for 30 seconds per spectrum acquisition. When 2 °C/min sample heating and cooling rates are employed, successively measured infrared spectra are acquired at 1 °C intervals.

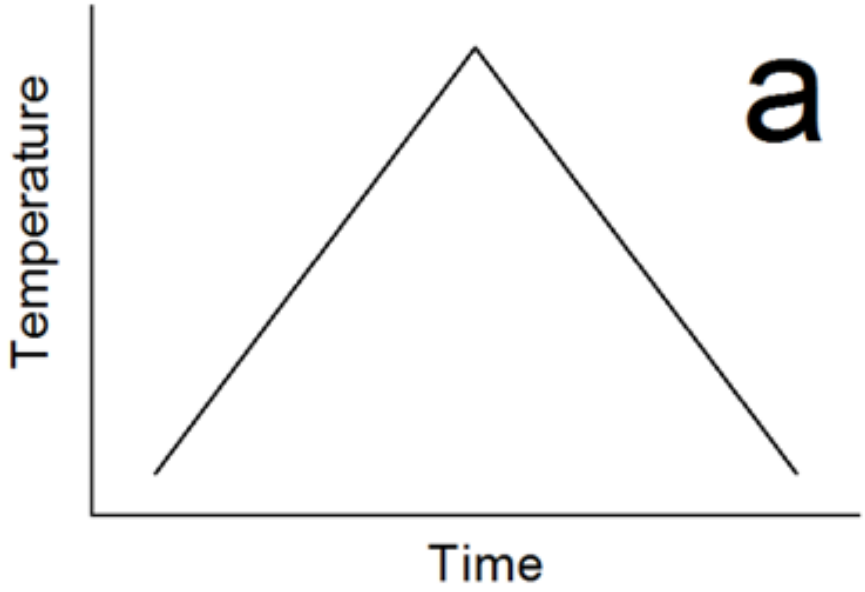

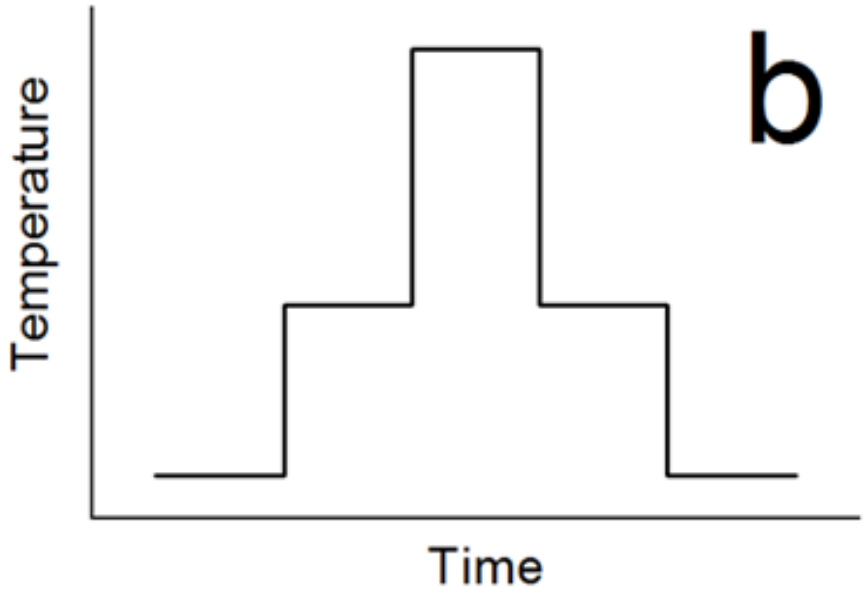

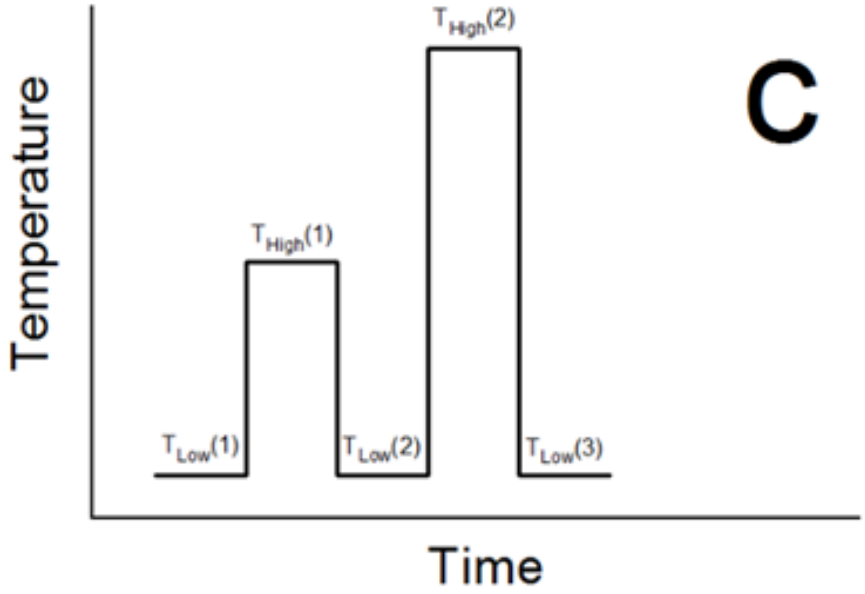

Figure 4.3: (a) Linear heating/cooling ramp, (b) stair-step, and (c) step-up/down temperature programs.

Figure 4.3b shows a “stair-step” temperature program. Like the linear ramp shown in Figure 4.3a, heating and cooling segments can be applied to the sample in a single temperature program. This program is employed when isothermal spectrum measurements are required. Rapid heating (or cooling) is employed between isothermal interferogram collection periods to quickly adjust the sample temperature to the next isothermal step. High heating and cooling rates are used to maximize the fraction of the total analysis time devoted to spectrum measurements. An optional isothermal delay can be inserted prior to spectrum measurements after each step temperature increase (or decrease if cooling). Unlike the linear ramp temperature program, spectra are acquired at constant

sample temperatures. This sample heating profile is useful for acquiring spectra at pre-selected temperatures. Customized programs with small temperature increments spread over multiple temperature ranges can be programmed. By using this approach, spectrum measurements can be restricted to select sample temperature ranges, providing a means to "target" only those temperature range(s) that are of particular interest. Compared to the linear ramp program, the stair-step profile can significantly reduce the total time required for temperature-dependent spectral measurements as well as quickly evaluating whether further thermal studies are warranted.

Figure 4.3c illustrates a "step-up/down" temperature versus time program. Sample temperatures are returned to the starting temperature after each heating step. Information regarding the reversibility of vibration band intensity changes caused by sample heating can be derived from the infrared spectra acquired by using this program.[201-202] As shown in Figure 4.3c, a $T_{Low}(n)$ spectrum is measured prior to each step temperature increase, and a $T_{Low}(n+1)$ spectrum is obtained after cooling the sample from the $T_{High}(n)$ temperature. Reversible changes are defined as those detected in spectra acquired at $T_{High}(n)$ that disappear in the subsequently measured $T_{Low}(n+1)$ spectrum, whereas irreversible changes persist in the $T_{Low}(n+1)$ spectrum. The $T_{Low}(n+1)$ spectrum will differ from the $T_{Low}(n)$ spectrum if irreversible sample changes occurred while heating the sample. Thus, a $T_{Low}(n+1) - T_{Low}(n)$ spectrum subtraction reveals irreversible changes. Because

infrared spectrum features associated with irreversible sample changes are present in both the $T_{Low}(n+1)$ and $T_{High}(n)$ spectra, they cancel in the $T_{High}(n) - T_{Low}(n+1)$ subtraction, leaving only reversible spectrum changes. It should be noted that the "reversible" and "irreversible" classifications depend on the spectrum measurement conditions. For example, negative difference spectrum features representing water loss would be classified as irreversible if samples were heated under vacuum because the water vapor released from the sample by heating would be continuously removed. However, when infrared spectrum measurements are made in an atmospheric environment with humidity, water may re-adsorb on dehydrated samples as they cool. In this case, water loss by heating would be classified as "reversible" because the intensity for the infrared spectrum bands associated with the lost water would return after cooling the sample. The relative amount of reversible water loss would depend on the sample cooling rate and the ambient humidity.

4.4 Sample Mineral Thermal Properties

Minerals have traditionally been identified, characterized, and quantified using X-ray Diffraction (XRD). This technique, however, can be time consuming and is largely limited to minerals with high crystallinity.[164, 203-204] Infrared spectroscopy is an alternative analytical technique that allows for investigation of minerals.[205-206] Indeed, infrared spectroscopy has been successfully applied to mineral identification, elucidation of complex clay mineral structures,[207]

paleoenvironmental reconstruction studies,[208-209] gemology research,[125] and the honing of technological mineral processing.[210] Button-IR further expands the possibilities of infrared spectroscopic study of minerals.

4.4.1 Silica

Silica gel (CAS: 112926-00-8) and α-quartz (CAS: 14808-60-7) powders were obtained from Sigma-Aldrich (St Louis, MO, USA). The silica gel was Davisil grade 634 and was 99% pure with a 74–149 μm particle size distribution, 60 Å pore diameters, and a 480 $m^2\ g^{-1}$ surface area. All chemicals were used as received without additional purification. Received powders were ground until uniform particles with low micron diameters were obtained. Sample powders were placed on the modified button wire mesh with a spatula and manipulated into the voids using an artist brush to form thin layers at the base of the mesh.

Silicon is ubiquitous throughout the environment, making up approximately 27.7% of the earth's crust.[211] Found in rocks, sand, and clays, it is primarily bound as silicon dioxide (SiO_2) due to reactions with atmospheric oxygen.[212] Silica can be crystalline, such as quartz, or non-crystalline in structures like silica gel or diatomaceous earth. The silica form is largely determined by the temperature and pressure conditions it is formed under. This means, that while they often appear physically similar when pure, solid and white at room temperature, their properties and structures are not the same.

Quartz is a common form of crystalline SiO_2 that can be obtained with high purity.[213] It exists in two forms: alpha- which is trigonal in formula unit structure and stable up to 573℃, and beta- which is hexagonal in structure and stable above 573℃. Alpha-quartz (α-quartz), examined in this study, belongs to the hexagonal crystal family, the trigonal crystal system, and the hexagonal lattice system. It is classified as a tectosilicate, a mineral type in which silicate tetrahedra (SiO_4) formula units are interconnected with each other forming a rigid and repeating structure. Alpha quartz has a trigonal motif meaning that three silicate tetrahedrons make up the basic structural building block.

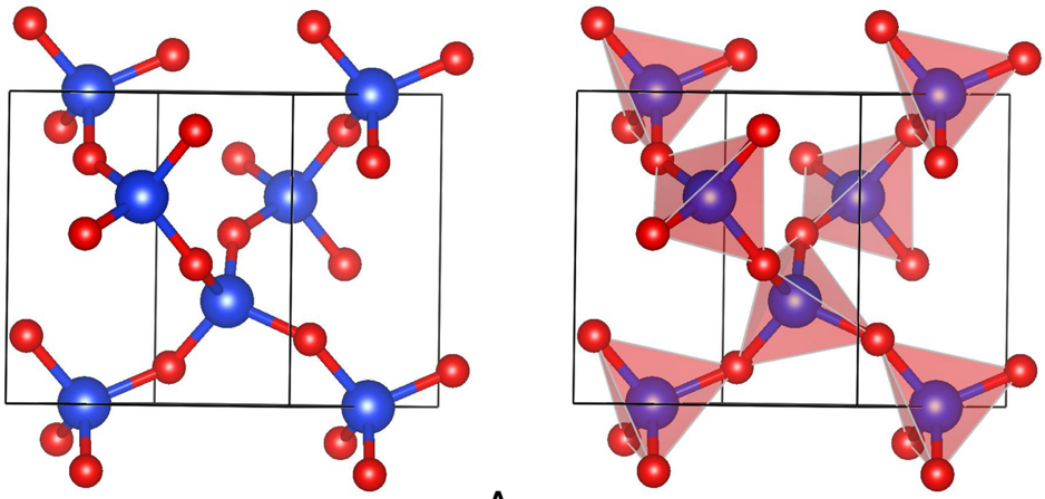

A

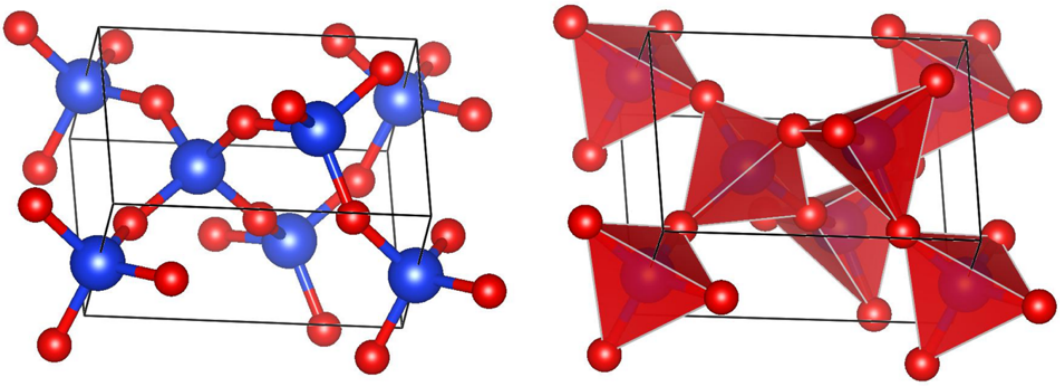

B

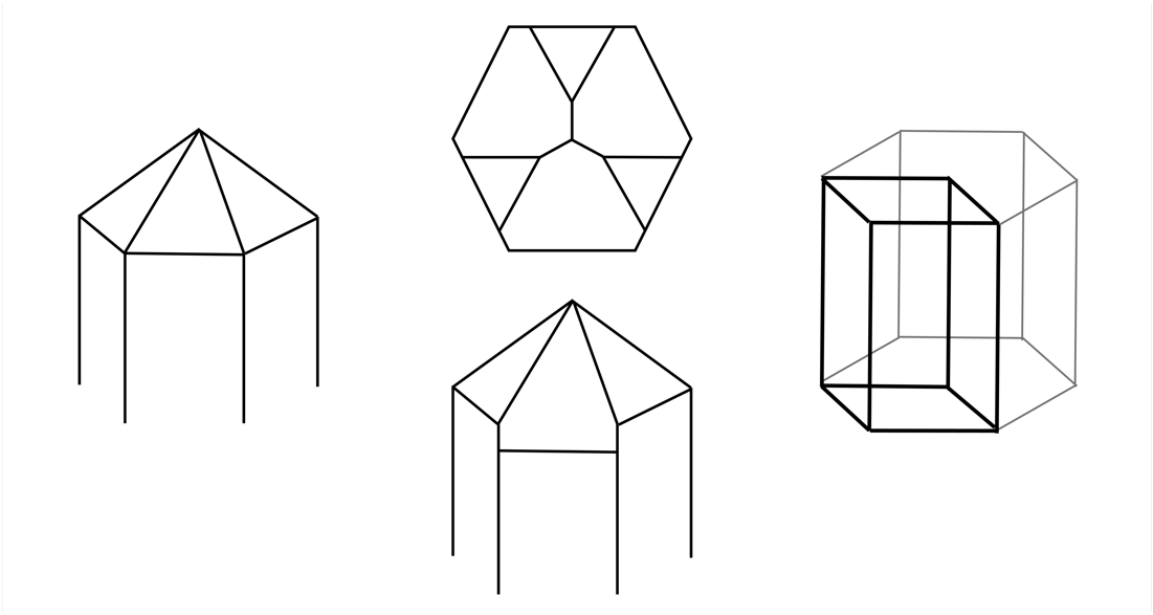

Figure 4.4: (a) α-quartz structure crystal lattice model from Rosa et al.[214] (b) X-ray diffraction determined crystal structure from Glinnemann et al.[215] Structural modelling was accomplished by using the VESTA software.[165] (c) Left - profile depiction of an ideal hexagonal prismatic crystal. Middle – Realistic view from top of α-quartz pyramid (top) with offset prismatic faces (bottom). Right – hexagonal unit cell of α-quartz.

The silicon oxygen bonds in quartz are polar and covalent, thus neither element can move freely within the crystal, and there are no interstitial cations. This macromolecular structure is shown in Figure 4.4. Figure 4.4a and Figure 4.4b show a unit cell of silicate tetrahedra (SiO_4) and the interconnection pattern of the silicate tetrahedra units in α-quartz, where O^{2-} are shared between tetrahedra. Lattice parameters in Figure 4.4a were derived through computation models. Lattice parameters in Figure 4.4b were observed via X-ray diffraction. The Si-O-Si bond forms an angle of 144° resulting in a complex structure overall.[216] Oxygen atoms on the surface of the crystal are often bonded to hydrogens.

Figure 4.4C is a rendering of the macro structure of α-quartz crystal. α-quartz is part of the hexagonal family with a hexagonal crystal unit cell but crystallizes in a way to produce trigonal symmetry. The image on the left shows the typical depiction of a hexagonal crystal – the quintessential prismatic crystal shape that first comes to mind for the hexagonal crystal family. In reality, however, α-quartz is not a perfect hexagonal crystal. When closely examined from the top as in the middle-top diagram, it becomes apparent that the pyramid portion is not a perfect hexagon. It has two sets of roughly triangular faces and offset prismatic sides (middle-bottom). The diagram on the right is a hexagonal lattice. In α-quartz the slightly distorted hexagonal lattice has three-fold rotational symmetry (trigonal crystal system) whereas β-quartz has six-fold symmetry.

Silica gel is a precipitated amorphous (i.e. less crystallinity) silica formed by reactions between water and quartz.[217] It is commonly used in chromatography columns, bioactive glasses, carbon sequestration, catalysis, and as a commercial desiccant.[218-220] The hydrated silica gel three-dimensional structure consists of polymerized hydrated silicon dioxide units ($mSiO_2 \cdot nH_2O$). Silica gel is typically hard and translucent to white in color. It has a higher porosity and is softer than its crystalline counterpart quartz.[221] Water can penetrate the sponge-like structure and reside within the interconnected unevenly sized pore spaces.

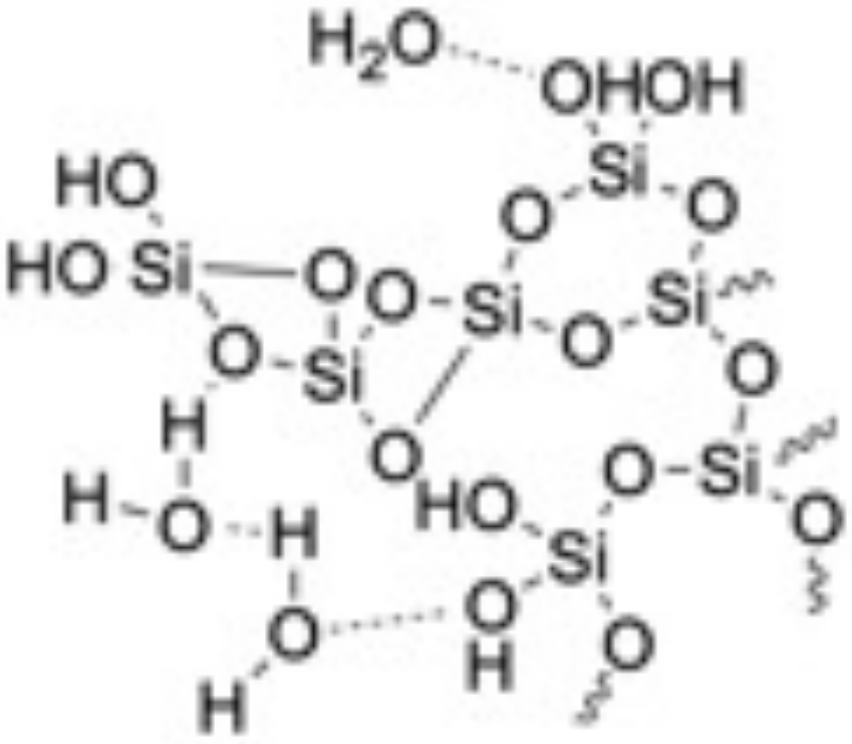

Figure 4.5: Representation of amorphous silica gel containing hydrogen bonded water molecules.

Hydrogen bonds between silica gel surface hydroxyl groups and oxygen atoms in water molecules (Figure 4.5) make silica gel an efficient desiccant. Silica gel is typically classified in one of three colloquial categories based on what is present in its pores: aquagel, xerogel, and aerogel. Aquagel pores are filled with water, xerogels often used in commercial desiccant packets have had water removed from its pores via evaporation, and the solvent in aerogel pores was removed by supercritical extraction.[221] Its efficient dehydration and rehydration make it an effective and reusable desiccant and filtration packing.

Figure 4.6a shows an overlay of α-quartz (red) and silica gel (blue) infrared spectra obtained by using the sample temperature perturbation apparatus described here. These spectra were obtained at room temperature and were normalized by scaling the most intense band to 100%. The intense band above 1000 cm^{-1} in each spectrum is assigned to asymmetric Si-O-Si stretching vibrations, whereas lower intensity bands near 800 cm^{-1} result from symmetric Si-O-Si stretching vibrations. The silica gel infrared spectrum contains a broad band above 3000 cm^{-1} associated with O-H stretching vibrations. This band can be attributed to Si-OH functionalities and adsorbed water, which are far less abundant in α-quartz. The more uniform Si-O-Si bonds within the α-quartz structure results in narrower wavenumber ranges for the corresponding infrared spectrum vibration bands. The α-quartz Si-O-Si vibration bands are therefore sharper than the corresponding silica gel bands. Figure 4.6b shows infrared spectra obtained at 150

°C for the same two silica samples. The α-quartz 150 °C spectrum appears to be nearly identical to the room temperature spectrum in Figure 4.6a, whereas the silica gel spectrum contains less intensity above 3000 cm^{-1} due to partial sample dehydration.

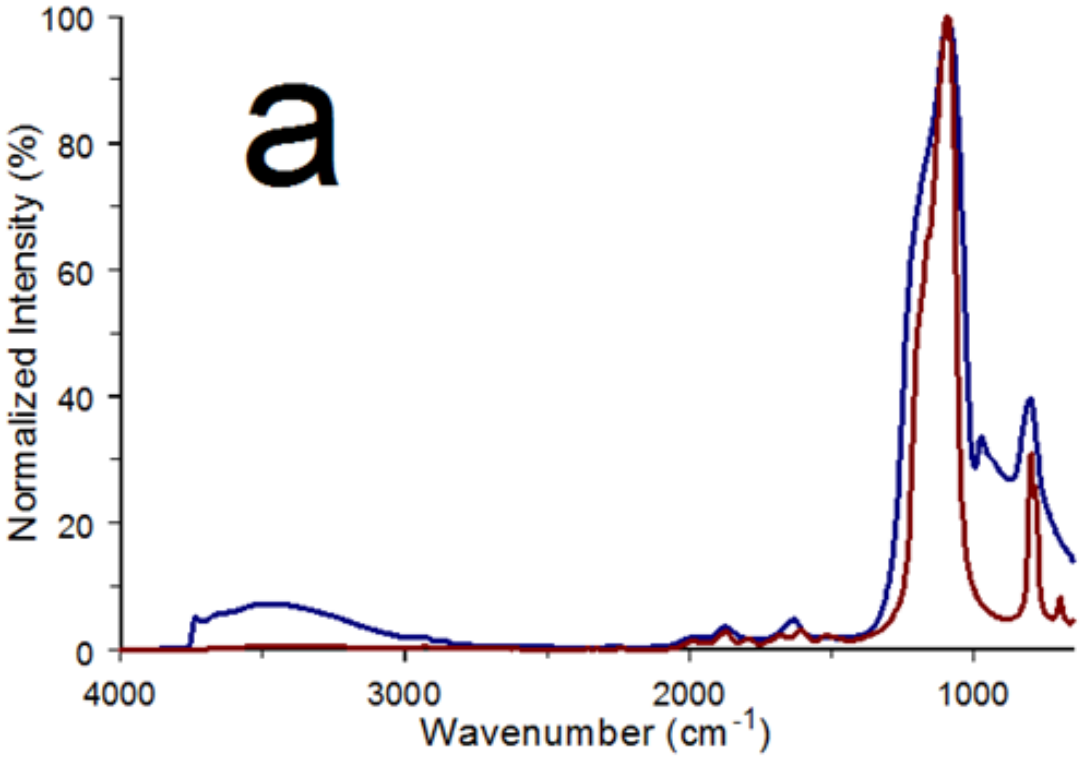

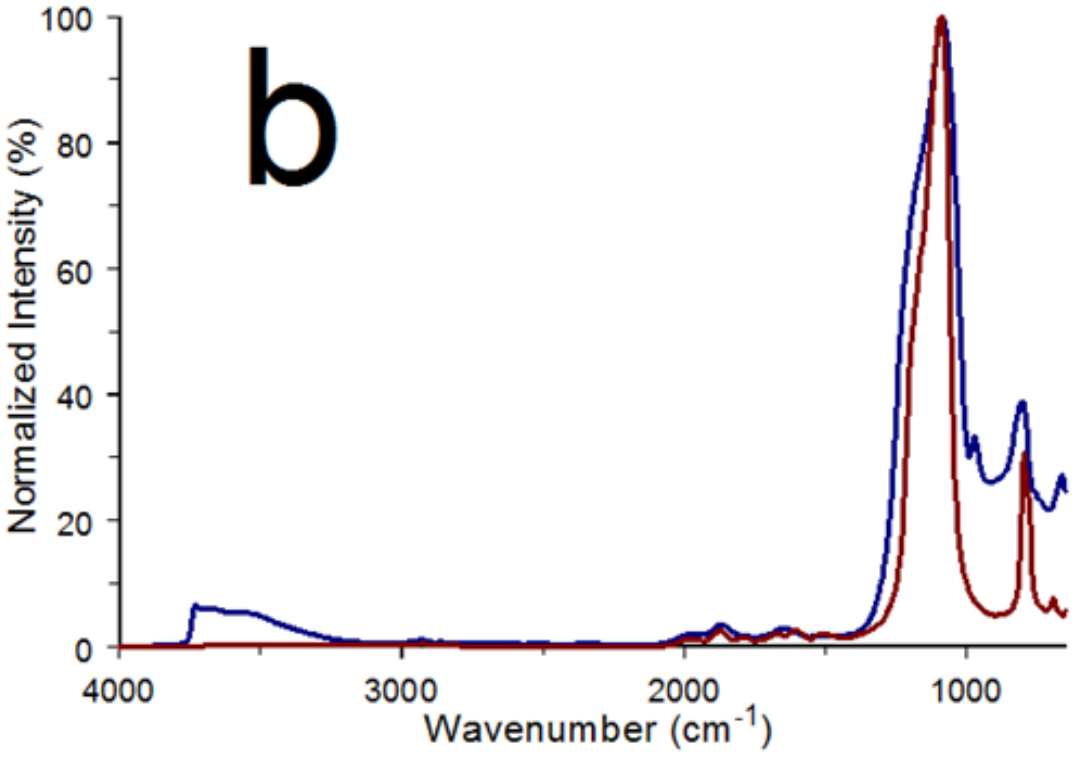

Figure 4.6: Infrared spectra for α-quartz (red) and silica gel (blue) (a) before heating and (b) at 150 °C.

By using a step-up/down temperature program, the spectral changes in the 150 °C spectrum that were reversed upon cooling were differentiated from those attributed to irreversible sample variations. The step-up/down temperature program consisted of 10 °C step increments beginning at 30 °C. Sample temperatures were returned to 30 °C after each step temperature increase. Although the 30 and 150 °C α-quartz infrared spectra in Figure 4.6 appear to be identical, small differences were revealed when these spectra were subtracted. Figure 4.7 shows that the subtraction results reveal reversible (green) and

irreversible (black) changes. The largest reversible intensity increase occurred at 1056 cm^{-1}, and the largest reversible intensity loss was detected at 1208 cm^{-1}. The negative reversible (green) band between 3500 and 3000 cm^{-1} is indicative of a small amount of water loss, resulting in a change of less than 0.25%. Reversible changes represented at most 6% intensity variations and were much larger than the irreversible changes. The sharp reversible change peaks below 1500 cm^{-1} were caused by variations in Si-O-Si stretching vibrations. The shapes of the difference spectrum residuals between 1500 and 700 cm^{-1} suggest that several overlapping Si-O-Si vibration bands were impacted when the sample was heated. The magnitudes of these changes were temperature dependent. Figure 4.8 shows variations in the 1056 and 1208 cm^{-1} intensities as a function of step temperature. Solid lines depict intensity changes in spectra acquired at each step temperature, whereas dashed lines denote intensities after subsequent cooling to the T_{Low} (30 °C) temperature. Figure 4.8 shows that intensity changes at 1056 cm^{-1} (circles) and 1208 cm^{-1} (triangles) were in opposite directions and approximately linear with respect to the step temperature. The dashed line plots indicate that intensities at these wavenumbers returned to their initial 30 °C spectrum levels after cooling. Thus, the plot trends in Figure 4.8 confirm that these temperature-dependent infrared spectrum changes were reversed after the sample perturbation was removed.

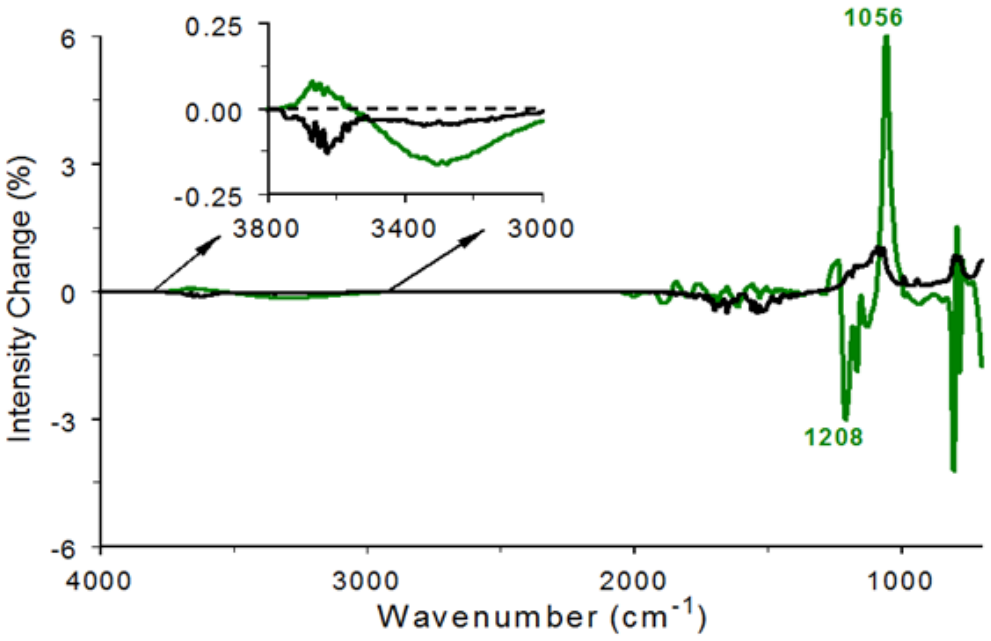

Figure 4.7: Reversible (green) and irreversible (black) spectrum changes resulting from heating α-quartz to 150 °C.

The silica gel infrared spectrum changes in Figure 4.6 are largely associated with loss of intensity above 3000 cm^{-1} due to sample dehydration. The reversible (green) and irreversible (black) changes to the silica gel spectrum are shown in Figure 4.9. Both curves exhibit broad negative bands above 3000 cm^{-1} that are indicative of water loss. The shapes of these broad bands differ, and the reversible band area exceeds the irreversible band area. Small positive peaks near 3700 cm^{-1} result from Si-OH functionalities that have lost hydrogen bonding interactions due to water removal, which caused the Si-OH vibration band to shift to higher wavenumbers. Below 2000 cm^{-1}, reversible spectrum changes were mostly positive, and irreversible intensity changes were mostly negative. Both

curves exhibited negative intensities near 1630 cm^{-1}, which corresponded to the H-O-H bending vibration. This indicates that both reversible and irreversible water losses were detected in the 0.16 kPa p(H_2O) dry air purge environment.

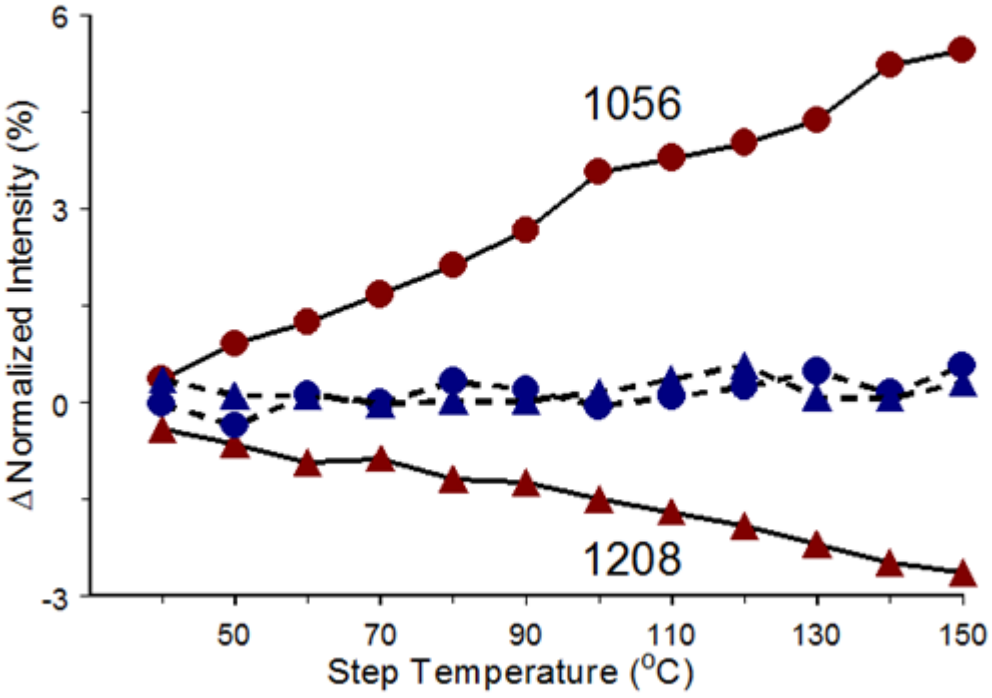

Figure 4.8: Intensity versus step temperature (red) trends at 1208 cm^{-1} (triangles) and 1056 cm^{-1} (circles). Dashed lines denote intensities after cooling (blue) back to 30 °C.

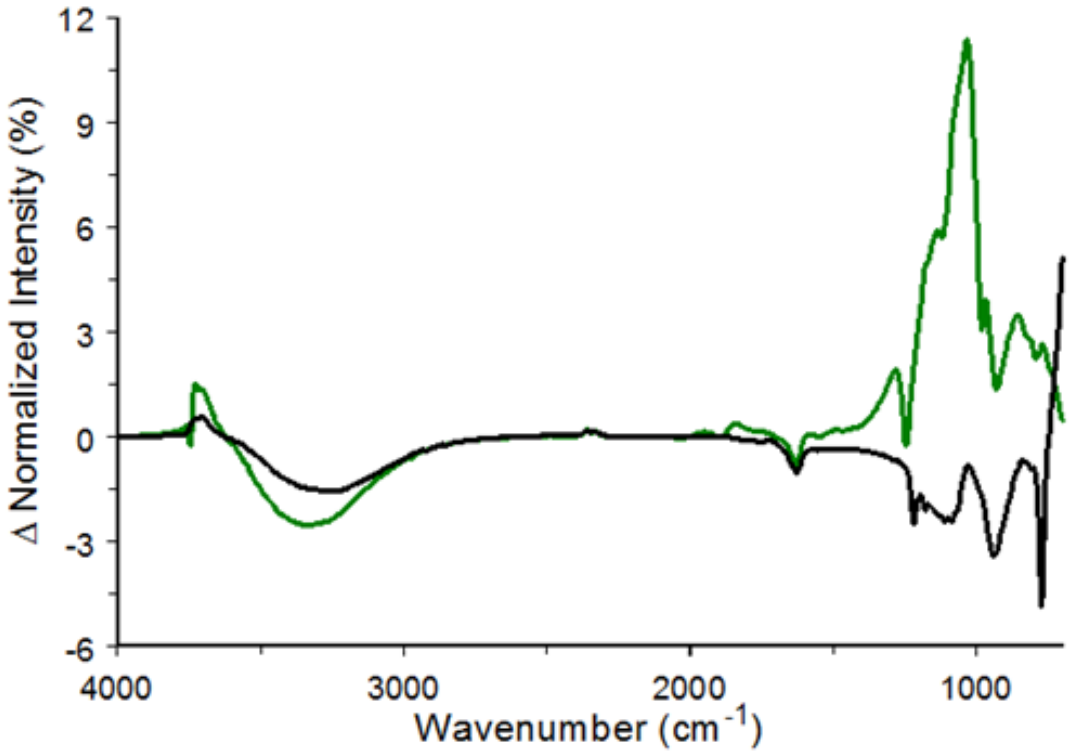

Figure 4.9: Reversible (green) and irreversible (black) spectrum changes resulting from heating silica gel from 30 to 150 °C.

Figure 4.10 shows the H-O-H bending vibration band area (1700–1600 cm^{-1}) as a function of temperature. Areas were normalized by dividing them by the initial 30 °C area. The dashed line in Figure 4.10 is a plot of the sample temperatures measured during the 2 °C/min heating and cooling ramps. The exponential decrease in the bending vibration band area during sample heating reflects the temperature-dependence of sample dehydration mechanisms. About 45% of the initial band area remained after heating the sample to 150 °C. Some of the water lost by heating to 150 °C was regained by the sample during cooling,

resulting in an intensity increase after 60 min. Because the H-O-H bending vibration band area only returned to 80% of its initial value, about 20% of the water originally contained in the sample was irreversibly lost under these experimental conditions.

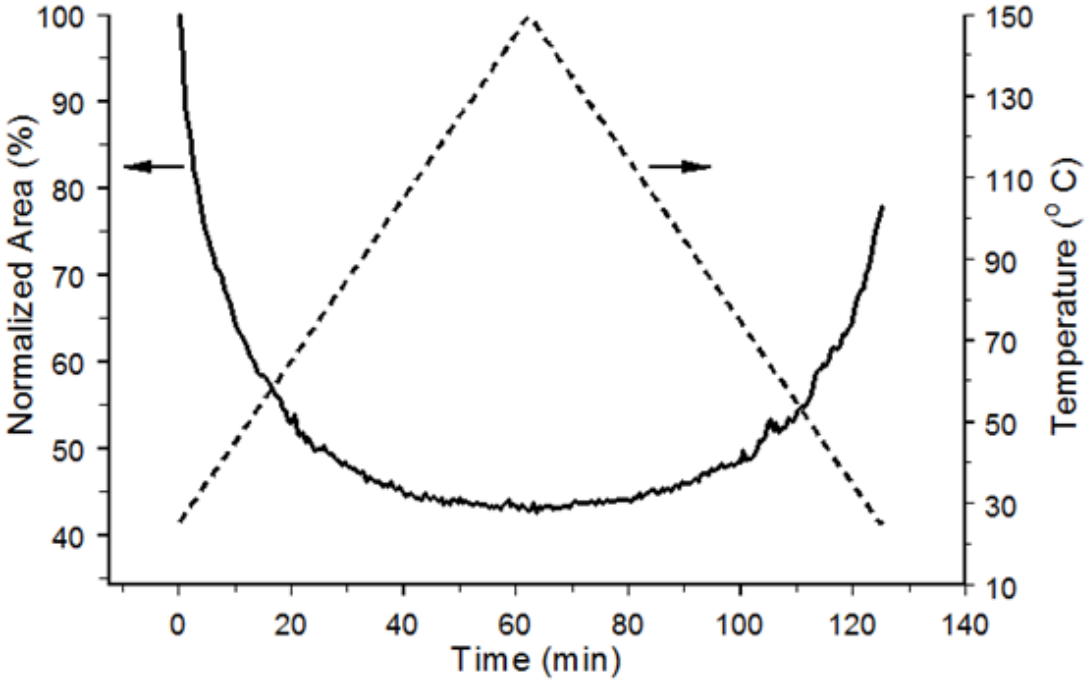

Figure 4.10: Integrated band area between 1700 and 1600 cm^{-1} (solid line) and sample temperature (dashed line) for silica gel plotted as a function of time.

4.4.2 Montmorillonite Clay

Montmorillonite (K-10) (CAS: 1318-93-0) was obtained from Sigma-Aldrich (St Louis, MO, USA). The K-10 clay was characterized by a 269 $m^2\ g^{-1}$ surface area, 0.8 meq g^{-1} cation exchange capacity, and its elemental composition has

been reported elsewhere.[222] The montmorillonite clay consisted of fine particles and was loaded into button meshes as received. Montmorillonite clays enriched with K^+ and Ca^{2+} interlayer cations were prepared by following previously described ion exchange procedures.[223]

Clays are common soil constituents. Like silica gel, clays absorb and hold water in their pores. Montmorillonite is a member of the smectite 2:1 three layered sheet silicate category. One octahedral aluminum-oxygen-hydroxyl layer is sandwiched between two negatively charged SiO_4 tetrahedral sheets.[224] This structure is shown in Figure 4.11.

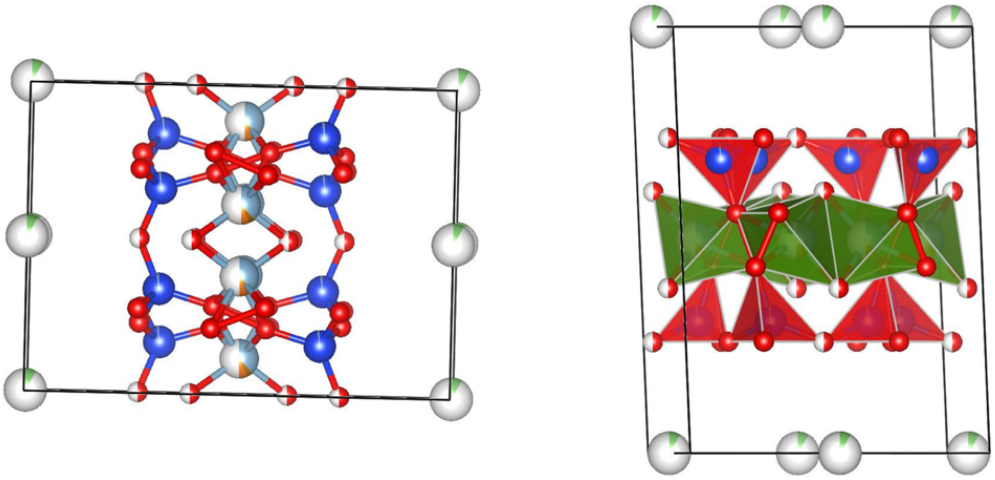

Figure 4.11: Schematic of montmorillonite structure from Gournis et al.[225] Structural modelling was accomplished by using the VESTA software.[165]

Interlayer cations, such as Al, Mg and Fe balance out the negative sheet charges and influence montmorillonite clay characteristics. In particular, they determine the quantity of water retained by the clay.[226] The interlayer water content

is also a function of ambient humidity because montmorillonite can absorb water from the surrounding air. Ultimately, the nature of the interlayer cation and atmospheric humidity determine the basal spacing, which is the distance between inorganic oxide sheets. Typical basal spacings for dehydrated montmorillonite clays are about one nm. After exposure to water, montmorillonite clay basal spacings increase in discrete steps that roughly correspond to water monolayers.[224, 227]

Montmorillonite infrared spectra were similar to the silica gel spectrum in Figure 4.6a. Overlapping high-intensity bands near 1050 cm^{-1} correspond to inorganic oxide vibrations. Spectra also contain broad bands due to O-H stretching vibrations.[130] The O-H stretching vibration band includes contributions from inorganic oxide hydroxyl groups and interlayer water.[228] Vibrations of inorganic oxide Al-OH functionalities occur over the 3750–3550 cm^{-1} range and maximize near 3630 cm^{-1}.[228] Interlayer water molecule stretching and bending vibrations are affected by interactions with other water molecules, cations, and inorganic oxide surfaces. These interactions are responsible for broad bands that extend from 3700 to about 2500 cm^{-1}.

Figure 4.12 shows room temperature infrared spectra of montmorillonite clays enriched in K^+ (red) and Ca^{2+} (blue). These spectra are similar except for the O-H stretching and H-O-H bending vibration band intensities. Because the clay with Ca^{2+} interlayer ions contained more water, the O-H stretching and H-O-H

bending vibration bands had greater intensity. These clays were subjected to a temperature program consisting of heating at 2 °C/min from 30 to 150 °C followed by cooling back to 30 °C at 2 °C/min.

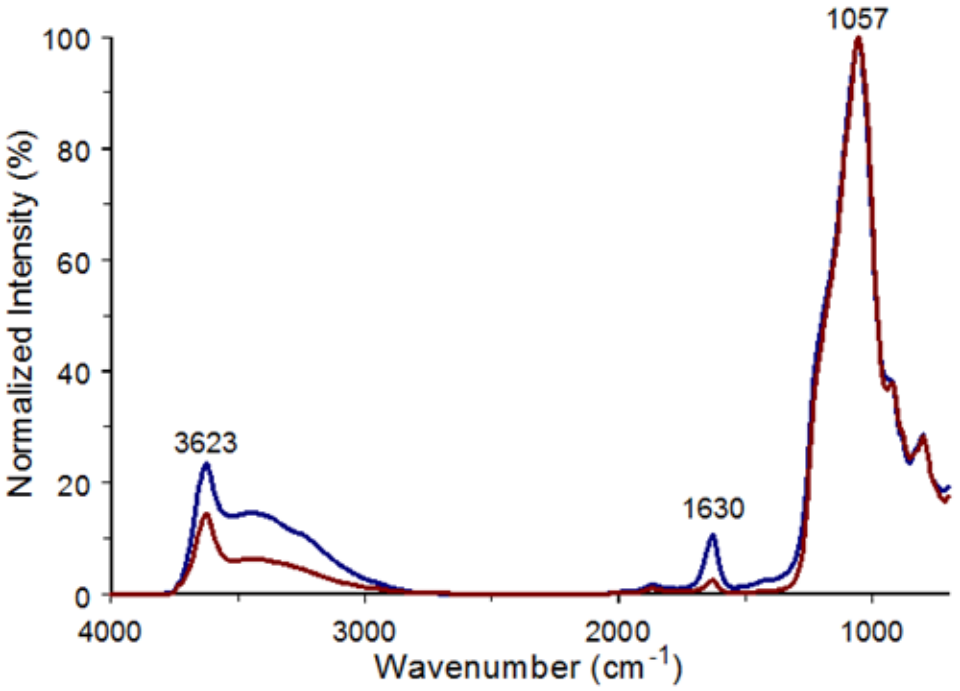

Figure 4.12: Infrared spectra for montmorillonite clays enriched in K^+ (red) and Ca^{2+} (blue).

Irreversible spectrum changes associated with this heating and cooling program were revealed by subtracting the initial 30 °C spectrum from the spectrum acquired after cooling from 150 °C to 30 °C. The results of these spectral subtractions are shown in Figure 4.13 for the K^+ (red) and Ca^{2+} (blue) montmorillonite clays. As expected, intensity losses for bands attributed to O-H stretching and H-O-H bending vibrations were greater for the clay containing Ca^{2+}

ions. Subtraction residuals for the two clays differ below 1600 cm^{-1}. The K^+ clay exhibited mostly intensity losses, whereas intensity increased for the Ca^{2+}-enriched clay. The O-H stretching vibration band included Si-OH and Al-OH contributions in addition to water molecule stretching vibrations. Thus, the temperature dependence of this band does not accurately represent water loss trends during dehydration. Alternatively, the H-O-H bending vibration band near 1630 cm^{-1} can be uniquely attributed to water bending vibrations.

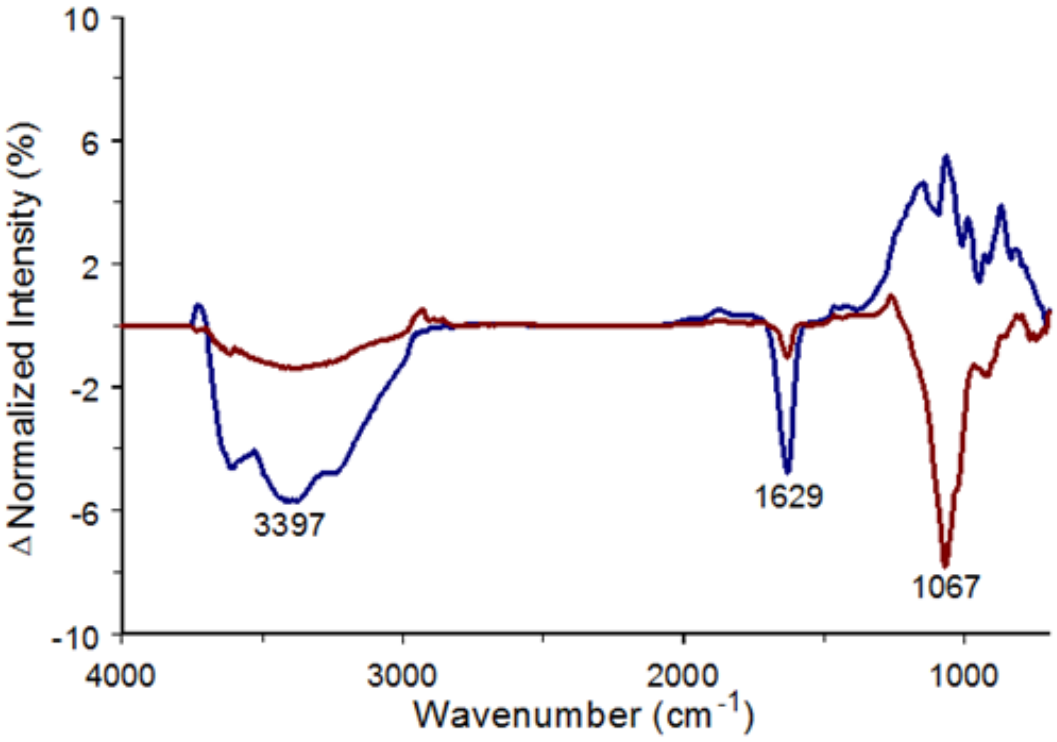

Figure 4.13: Irreversible spectrum changes resulting from heating to 150 °C for the K^+ (red) and Ca^{2+} (blue) enriched montmorillonite samples.

Figure 4.14 shows plots of 1700–1600 cm^{-1} normalized band areas as a function of time for the K^+ (red) and Ca^{2+} (blue) clays. The dashed line shows measured sample temperatures as a function of time. The two band area plots have different profiles. Initially, the water content diminished more rapidly for the K^+-enriched clay when the sample was heated. The K^+ clay band area dropped to a minimum of 18%, whereas the Ca^{2+} clay band area was reduced to 10% at 150 °C. After cooling from 150 to 30 °C, the K^+ clay band area increased to about 50% of its initial area, and the Ca^{2+} clay band area increased to about 30% of its starting value.

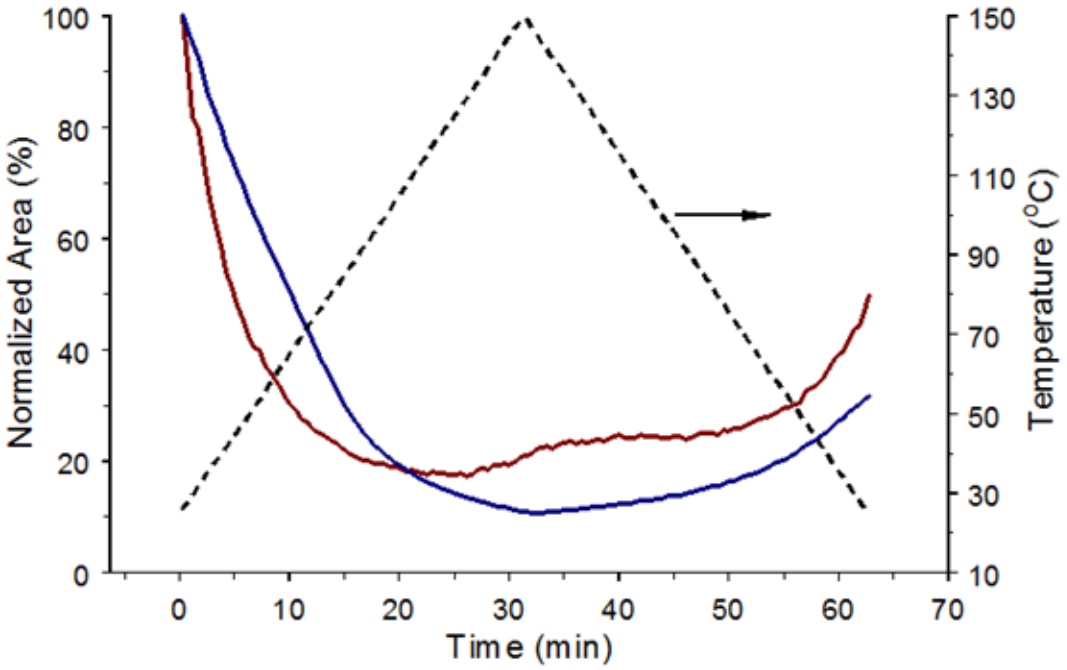

Figure 4.14: Band intensity area between 1700 and 1600 cm^{-1} versus time plots for the K^+ (red) and Ca^{2+} (blue) montmorillonite clay samples. The dashed line represents measured sample temperatures.

Differences in Figure 4.14 plots can be attributed to cation size and charge differences. Because these two clay samples were derived from the same inorganic starting material, the stacked layer structures should have been the same. However, there should have been roughly twice as many K^+ ions than Ca^{2+} ions within the respective enriched clay interlayer spaces. Although the room temperature infrared spectrum for montmorillonite clay appears to be similar to the silica gel spectrum, temperature-dependent spectral changes were quite different.

4.4.3 Gypsum

Calcium sulfate dihydrate (CAS: 1010-4-4) was obtained from Mallinckrodt (St Louis, MO, USA). It was used as received without additional purification. Samples were ground until uniform particles with low micron diameters were obtained. Sample powders were placed on the modified button wire mesh with a spatula and manipulated into the voids using an artist brush to form thin layers at the base of the mesh.

Calcium sulfate dihydrate (gypsum, $CaSO_4 \cdot 2H_2O$) is an abundant mineral with wide-ranging applicability.[229-231] Naturally occurring gypsum can form several meters thick stratified beds that also contain limestone, red clays, halite and other evaporite minerals.[232] $CaSO_4 \cdot 2H_2O$ is roughly 23.3% calcium and 18.5 % sulfur. Gypsum also exists in a refined anhydrite form which is approximately 29.4% calcium and 23.5% sulfur. The hemihydrate form $CaSO_4 \cdot 0.5H_2O$ is often referred

to as plaster of paris or bassanite. The solid-state structure includes sulfate anion sheets linked together by calcium ions to form double sheet layers (Figure 4.15).

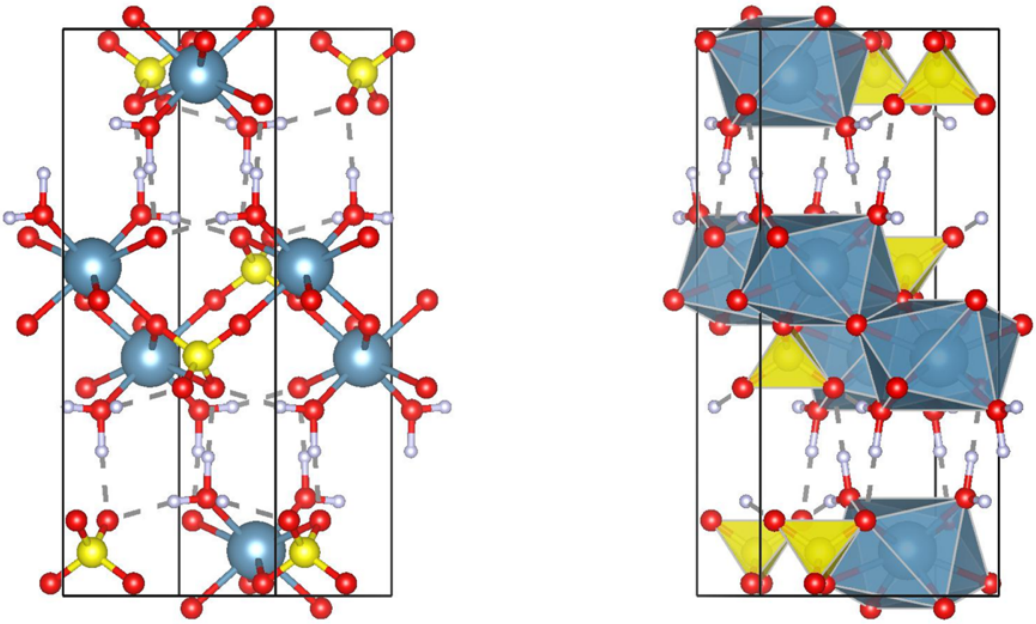

Figure 4.15: Schematic of the gypsum structure from Schofield et al.[233] Structural modelling was accomplished by using the VESTA software.[165]

Gypsum contains water layers interspaced between calcium sulfate layers.[234] Each water molecule oxygen is bound to a calcium ion, and water O-H groups form hydrogen bonds with sulfate oxygens from different double sheet layers.[235] In contrast to silica gel and montmorillonite clay, the more regular water molecule configurations in gypsum results in distinct infrared spectrum bands for the O-H stretching (3550 and 3410 cm^{-1}) and H-O-H bending (1685 and 1620 cm^{-1}) vibrations.[236] Because its properties depend heavily on water content, the dehydration mechanisms for this substance have been studied extensively.[237-241]

A temperature step-up/down perturbation methodology was employed to characterize calcium sulfate dihydrate dehydration processes by acquiring infrared spectra while heating the neat powder from 30 to 150 °C in 10 °C step increments. Two-minute isothermal periods were inserted prior to spectrum measurements at each step temperature. Figure 4.16 shows the initial 30 °C infrared spectrum, the spectrum obtained when the sample temperature was 150 °C, and the spectrum measured after cooling the sample from 150 to 30 °C. These spectra can be distinguished by their O-H stretching vibration band intensity shapes. The initial 30 °C spectrum is consistent with previously published spectra of calcium sulfate dihydrate.[242] The 150 °C spectrum is representative of anhydrous calcium sulfate.[243-244] The final 30 °C spectrum is consistent with calcium sulfate hemihydrate.[244] As shown in Figure 4.17, the temperature dependencies of sample dehydration processes can be characterized by plotting 3800–3000 cm^{-1} infrared spectrum integrated intensities as a function of sample temperature. The circles in Figure 4.17 represent integrated intensities derived from infrared spectra measured at 10 °C step temperature increments, and the squares denote intensities derived from spectra obtained after cooling the sample to 30 °C from those temperatures. The single step transition exhibited by the circles in Figure 4.17 is consistent with a recent study that found that calcium sulfate dihydrate dehydration depended on water vapor partial pressure [$p(H_2O)$].[237] That study found that when $p(H_2O)$ was below 0.2 kPa, slowly heating calcium sulfate

dihydrate resulted in direct conversion to anhydrous calcium sulfate without forming the hemihydrate intermediate. Furthermore, when a 1 °C/min heating rate and 0.18 kPa p(H_2O) were employed, this conversion was essentially complete after the sample temperature reached 100 °C. Because the FTIR dry air purge resulted in a 0.16 kPa p(H_2O) environment, the formation of hemihydrate during sample heating was minimized.

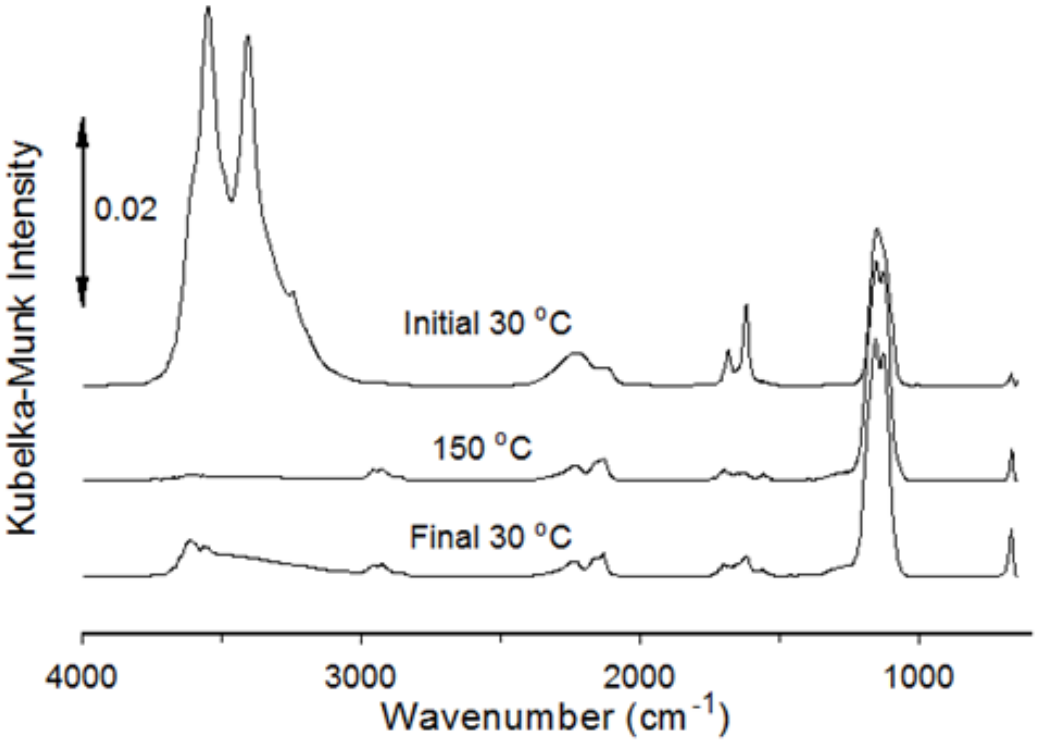

Figure 4.16: Gypsum infrared spectra obtained at 30 °C, after heating to 150 °C, and after cooling back to 30 °C.

The integrated intensities for both plots in Figure 4.17 began to decrease above 50 °C and continued to decrease until 100 °C. The overlap of the circles and squares below 60 °C in Figure 4.17 (region I) indicates that infrared spectrum changes at these temperatures were minimal. These changes are characterized by Figure 4.18a, which shows the results of subtracting the initial 30 °C spectrum from the spectrum obtained at 50 °C (solid line) and by subtracting the 50 °C spectrum from the spectrum obtained after cooling the sample from 50 to 30 °C (dotted line). The solid and dotted line difference spectra are nearly mirror images. When the sample was heated to 50 °C, the solid line shows that spectrum changes were dominated by O-H stretching (>3000 cm^{-1}) and H-O-H bending (1685 and 1620 cm^{-1}) vibration band intensity losses. The 0.0015 intensity loss at 3550 cm^{-1} in Figure 4.18a represents 3.75% of the O-H stretching vibration band intensity in the initial 30 °C spectrum, confirming that intensity loss was minimal. In addition, intensity variations were detected for sulfate anion vibrations over the 1200–1000 cm^{-1} range and at 670 cm^{-1}. The intensity loss between 2300 and 2000 cm^{-1} is associated with the loss of sulfate vibration overtone and combination bands.[236] Intensity increases in the dotted line plot at the same wavenumbers as the negative solid line features indicate that the spectrum changes that occurred due to sample heating were reversed when the sample was cooled. The broad 3400–3000 cm^{-1} features in the two difference spectra represent hydrogen-bonded water molecules. Intensity in this region increased when the sample was heated to 50 °C

and then decreased when the sample was cooled back to 30 °C. This suggests that some of the water molecules responsible for the 3550 and 3400 cm^{-1} bands in the initial 30 °C spectrum remained in the solid state when the sample was heated but adopted orientations that provided more diverse hydrogen bonding interactions. Loss of broad band intensity over the 3400–3000 cm^{-1} range after cooling likely resulted from these water molecules returning to their 30 °C configurations.

The plots in Figure 4.17 exhibit decreased 3800–3000 cm^{-1} band areas for all measurements obtained after the sample had been heated to 60 °C (region II). The diminished intensities in spectra acquired at 30 °C after cooling (squares) indicate that irreversible sample changes (i.e., water loss) occurred at these temperatures. Interestingly, band areas for the spectra obtained at the step temperatures within region II (circles) were larger than those derived from the spectra obtained after the sample cooled to 30 °C (squares). This indicates that the 3800–3000 cm^{-1} spectrum areas continued to decline while the sample was cooling from these incremental step temperatures. Figure 4.18b compares difference spectra representing the changes that occurred by heating the sample from 30 to 80 °C (solid line) and after cooling back to 30 °C (dotted line). Unlike Figure 4.18a, both plots in Figure 14.8b exhibit intensity losses in the O-H stretching vibration band region. The 3700–3300 cm^{-1} expanded plot in Figure 4.18b shows that the dotted line difference spectrum contained positive deviations

near 3550 and 3410 cm^{-1}. This indicates that some water molecules adopted configurations that were similar to those that existed prior to the temperature step. Apparently, heating the dihydrate to temperatures within region II disrupted the layer structure, resulting in water release, and this process continued as the sample cooled back to 30 °C.

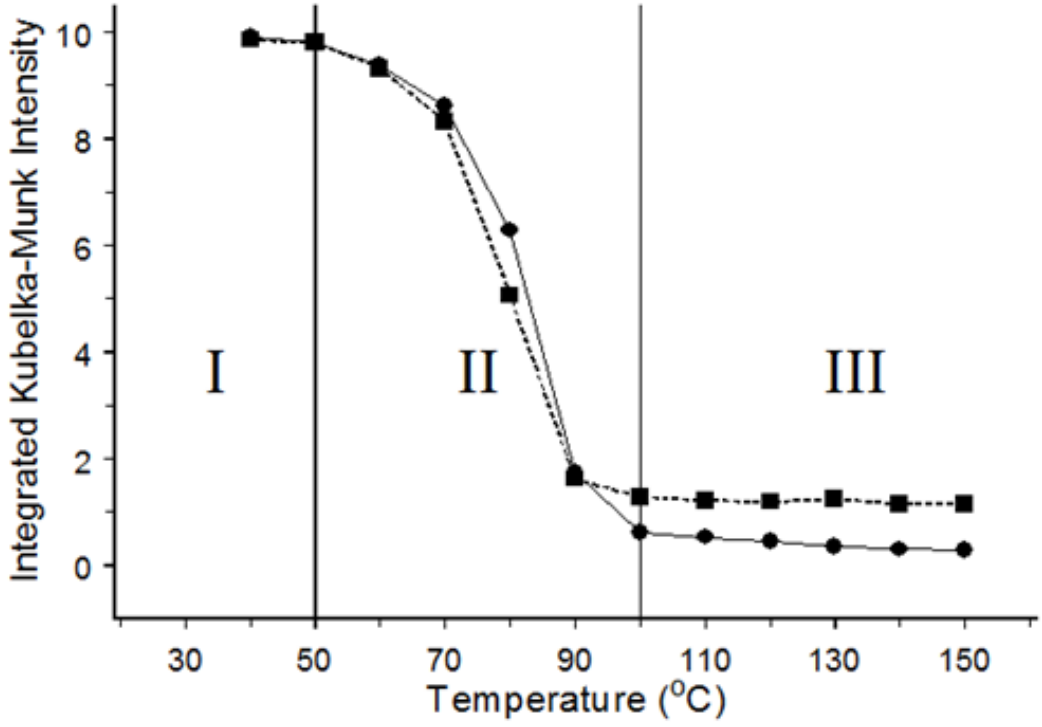

Figure 4.17: Integrated band intensity (area) spanning the O-H stretching vibration range (3800–3000 cm^{-1}) as a function of step temperature. Circles represent band areas from spectra obtained at the step temperatures and squares represent areas in spectra measured after cooling from those temperatures.

The Figure 4.17 plots in region III show that the band areas for the spectra measured over this temperature step range were relatively constant, and that the areas in the spectra obtained after cooling to 30 °C were also relatively constant but consistently greater. The gap between the two plots in region III can be attributed to water absorption during sample cooling. Figure 4.18c shows difference spectra computed in the same manner as described for the Figure 4.18a spectra but derived from the 150 °C temperature step measurements. The subtraction residuals in Figure 4.18c were similar to those observed for the 100–140 °C temperature step spectra. When the sample was heated to 150 °C, spectrum variations were associated with a loss of water and changes to sulfate anion vibrations. When the sample was cooled from 150 to 30 °C, these temperature-dependent changes were largely reversed due to sample re-hydration. The shape of the Figure 4.18c dotted line in the O-H stretching vibration region and the appearance of the 1620 cm^{-1} H-O-H bending vibration band indicate that cooling anhydrous calcium sulfate from 150 to 30 °C resulted in the formation of calcium sulfate hemihydrate. The mirror image relationship between the solid and dotted line plots in Figure 4.18c confirms that heating the sample to temperatures above 90 °C (region III) resulted in the conversion of calcium sulfate hemihydrate to anhydrous calcium sulfate.

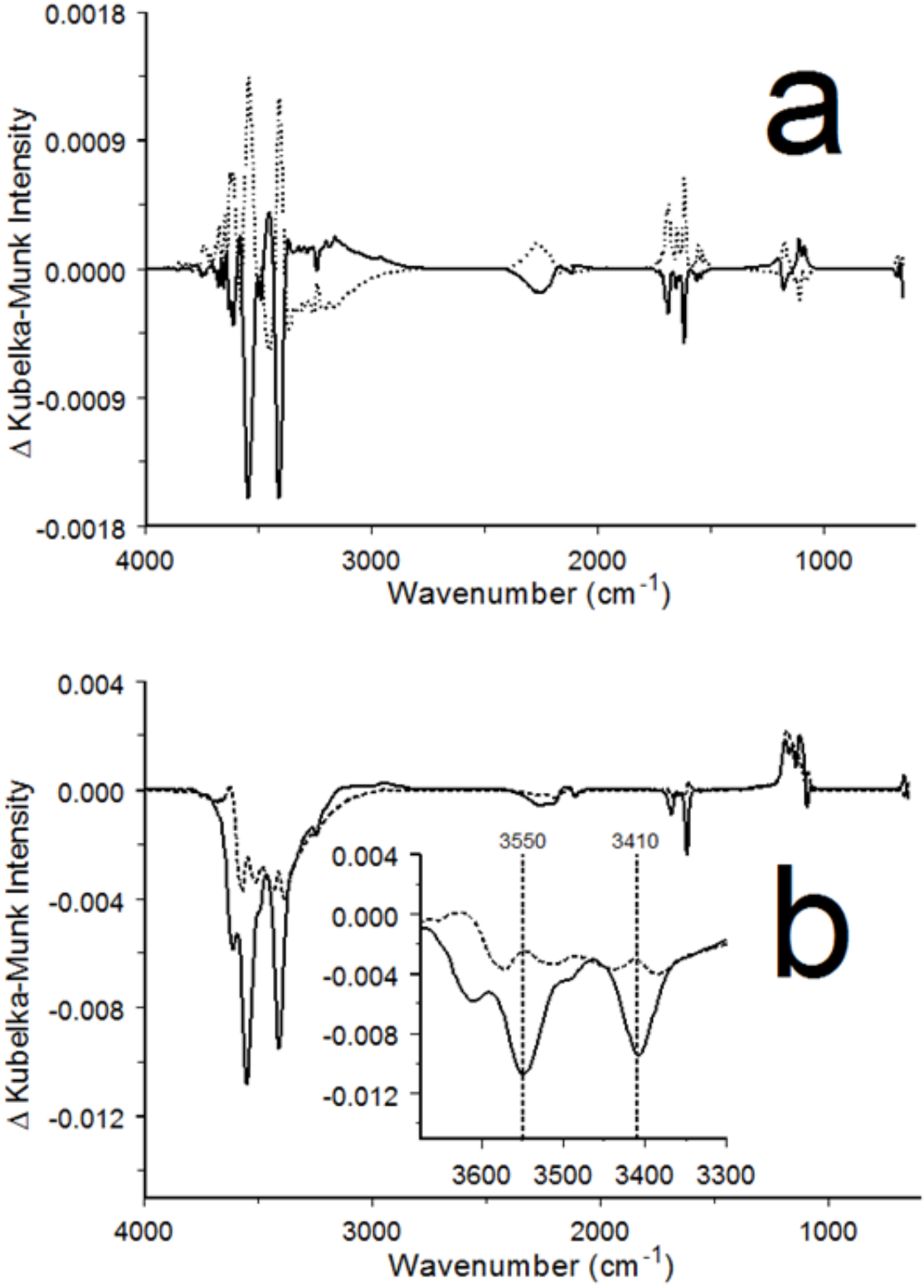
a
0.0018
0.0009
0.0000
-0.0009
-0.0018
Δ Kubelka-Munk Intensity
4000
3000
2000
1000
Wavenumber (cm-1)
b
0.004
0.000
-0.004
-0.008
-0.012
Δ Kubelka-Munk Intensity
3550
3410
0.004
0.000
-0.004
-0.008
-0.012
3600
3500
3400
3300
4000
3000
2000
1000
Wavenumber (cm-1)

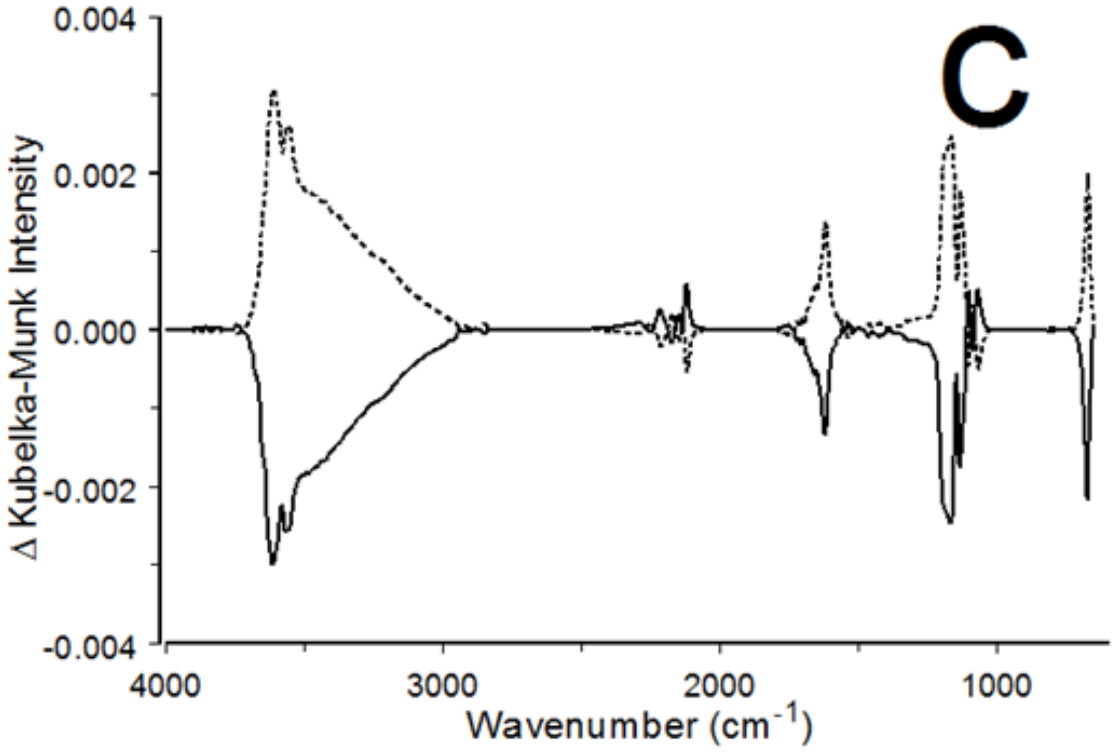

Figure 4.18: Gypsum infrared spectrum differences calculated by subtracting (a) the initial 30 °C spectrum from the 50 °C spectrum (solid) and the 50 °C spectrum from the subsequent 30 °C spectrum (dotted), (b) the 30 °C spectrum from the 80 °C spectrum (solid) and the 80 °C spectrum from the subsequent 30 °C spectrum (dotted), and (c) the 30 °C spectrum from the 150 °C spectrum (solid) and the 150 °C spectrum from the subsequent 30 °C spectrum (dotted).

The spectra in Figure 4.18 reveal variations in sulfate vibration bands as well as those associated with water molecules. The magnitudes of the difference spectrum features attributed to sulfate anions were found to correlate with water molecule vibration band variations. Thus, when water molecule vibration band

changes were reversible, sulfate vibration band changes were also reversible (Figure 4.18a). Complicated difference spectrum intensity profiles reflected sulfate anion symmetry changes at different stages of dehydration. A more complete interpretation of the temperature-dependent infrared spectrum changes attributed to sulfate anion and water molecule motions would likely necessitate additional studies and comparisons with results derived from molecular modeling calculations.

4.4.4 Coal

Lignite and bituminous coals (CAS: 12952-66-0) were obtained from Ward's Natural Science (Rochester, NY, USA). Coal samples were used as received without additional purification. Received powders were ground until uniform particles with low micron diameters were obtained. Sample powders were placed on the modified button wire mesh with a spatula and manipulated into the voids using an artist brush to form thin layers at the base of the mesh.

Coals consist of complex mixtures that are produced by the long-term effects of heat and pressure on organic matter though a process known as "coalification".[245] More than 200 different minerals have been identified in coals.[246] These impurities impact coal properties and can affect energy content. Coals are "ranked" based on carbon content, volatile matter, moisture, and the amount of heat energy they yield. The infrared spectra of lignite and bituminous coals contain infrared spectrum bands associated with organic functionalities and water.

Lignite coal is a soft, brown, and combustible sedimentary rock formed from compressed peat. The lignite stage of coalification is characterized by physical compaction of peat, dehydration, and biogeochemical gelification – the biological and chemical transformation of carbon molecules.[247-248] Lignite coals are the lowest rank of coal because they have a low carbon content (25-25%), high moisture content, and yield low heat energies.[249-250]

Bituminous coals have undergone a greater transformation to carbon than lignite and are categorized as medium-rank with roughly 45-86% carbon content, volatile matter below 14%, and a sub-20% moisture content. Coalification from lignite to bituminous coal results in enlarged aromatic core sizes, increased aliphatic structures, and decreased oxygen containing functional groups.[251] With high heating values, bituminous coals have been commonly used for electricity generation and steel making in the United States.

A lignite coal sample was analyzed by subjecting it to a step-up/down temperature program starting with T_{Low} at 25 °C and 25 °C step intervals to 150 °C. Five-minute isothermal periods were inserted prior to each T_{High} spectrum measurement. Figure 4.19a shows the infrared spectra of the lignite coal sample obtained at 25 °C (blue) and 150 °C (red).

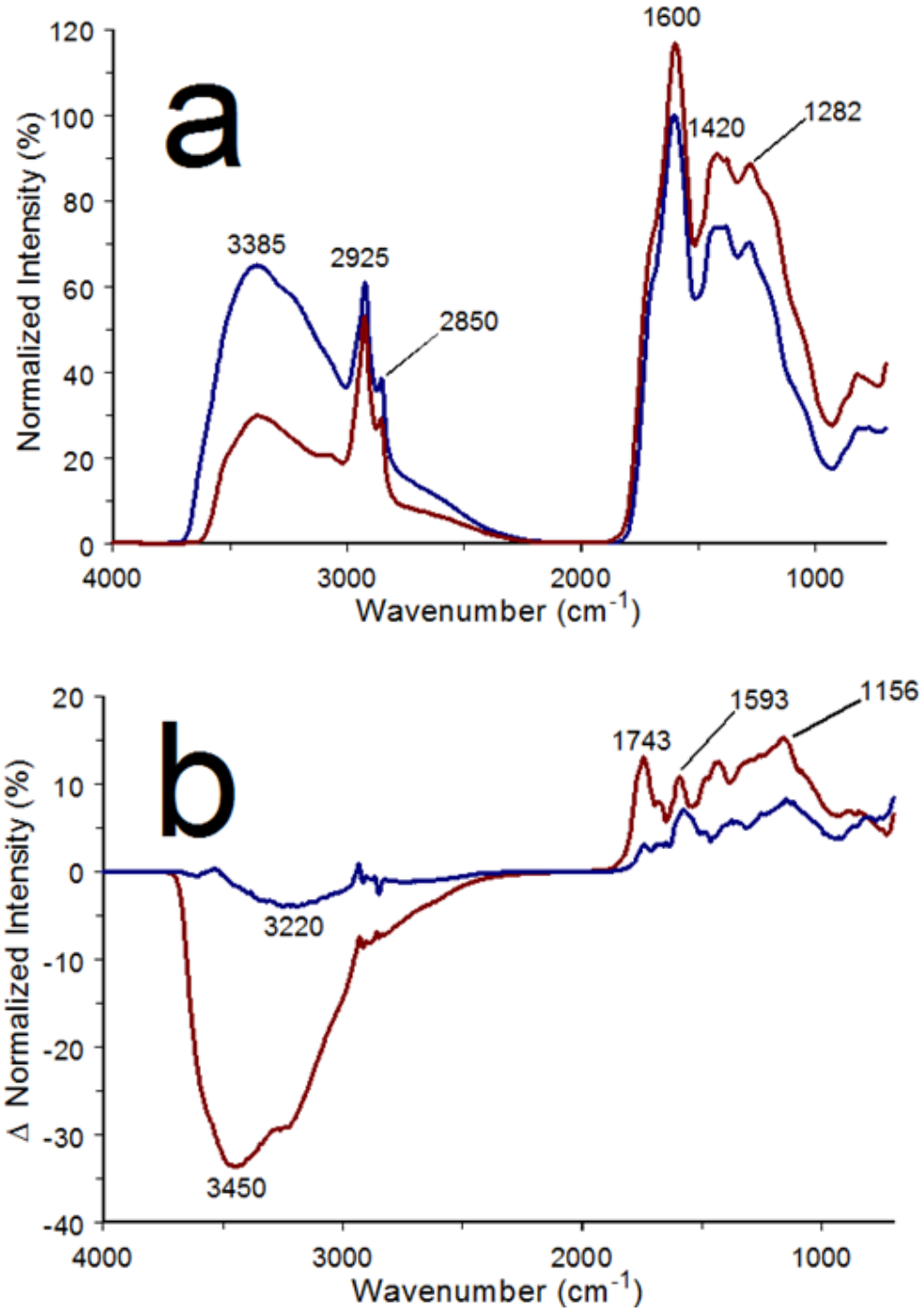

Figure 4.19: (a) Infrared spectra of a lignite coal sample obtained at 25 °C (blue) and 150 (red) °C. (b) Reversible (blue) and irreversible (red) spectrum changes resulting from heating the lignite from 25 to 150 °C.

Both spectra have similar band profiles but with different relative intensities. The broad feature extending from 3600 to 2200 cm^{-1} can be assigned to overlapping O-H stretching vibration bands. In general, band intensity at a lower wavenumber represents the hydroxyl groups involved in stronger hydrogen bonding.[252] The narrow bands at 2925 and 2850 cm^{-1} superimposed on the broad O-H stretching vibration band are representative of asymmetric and symmetric CH_2 stretching vibrations, respectively.[253] Band intensity below 2000 cm^{-1} characterizes the organic constituents of the coal sample and likely consists of several overlapping C-C and C-O stretching and C-C-H, H-C-H, C-O-C, and C-O-H bending vibrations.[254] The 1600 cm^{-1} band has been assigned to aromatic ring C-C stretching vibrations, and the 1282 cm^{-1} band is associated with C-O stretching vibrations.[255]

Figure 4.19a reveals that the O-H stretching vibration band intensity decreased and intensities for overlapping bands below 2000 cm^{-1} increased after the lignite coal sample was heated to 150 °C. Figure 4.19b shows that the cumulative reversible spectrum changes (blue) were smaller than the irreversible (red) changes. Most of the irreversible changes can be attributed to sample dehydration. In addition to dehydration, the loss of organic volatiles containing hydroxyl groups and oxidations of hydroxyl groups to carbonyl functionalities likely contributed to the reduction in the O-H stretching vibration band intensity. The

spectrum variations below 2000 cm^{-1} suggest that loss of substances containing hydroxyl groups was correlated with band intensity increases for a variety of organic functionalities. This intensity increase may have been caused by loss of hydrogen bonding between polar organic functionalities and the desorbed water. The positive peak at 1743 cm^{-1} likely represents carbonyl functional groups in the coal sample.

The step-up/down temperature perturbation program employed 25 °C step increments, making it possible to generate difference spectra representing the incremental sample changes resulting from heating the sample successively from 25 °C to 50, 75, 100, 125, and 150 °C (Figure 4.20). Incremental reversible spectrum changes (Figure 4.20a) exhibited similar intensity profiles that grew larger with increasing step temperature. In contrast, the largest irreversible spectrum changes were detected after heating the sample from 25 to 50 °C (Figure 4.20b). In fact, the shape of the 50 °C irreversible difference spectrum (gray) was similar to the cumulative irreversible difference spectrum in Figure 4.19b (blue). This suggests that most of the lignite coal hydroxyl group loss occurred below 50 °C. This is confirmed by the band area versus step temperature plots in Figure 4.21. Red lines denote 2000–700 cm^{-1} areas, whereas the blue lines represent 3600–2000 cm^{-1} areas. Squares denote areas derived from spectra measured at 25 °C $T_{Low}(n+1)$ temperatures, whereas triangles represent areas in spectra measured at $T_{High}(n)$ temperatures. The 2000–700 cm^{-1} band areas gradually

increased with temperature, whereas the 3600–2000 cm^{-1} areas decreased. The largest decrease in the 3600–2000 cm^{-1} area occurred after heating the sample from 25 to 50 °C, which is consistent with the incremental irreversible changes depicted in Figure 4.20b. Differences between areas derived from spectra measured at $T_{High}(n)$ and $T_{Low}(n+1)$ can be attributed to reversible changes. These area differences were likely due to the re-adsorption of water while cooling the sample after the heating steps. Notably, the 125 and 150 °C irreversible difference spectra contained positive peaks near 1772 cm^{-1} that were not present in the other Figure 4.20b spectra. These intensity increases are evidence of the formation of ester functionalities by sample oxidation.[256]

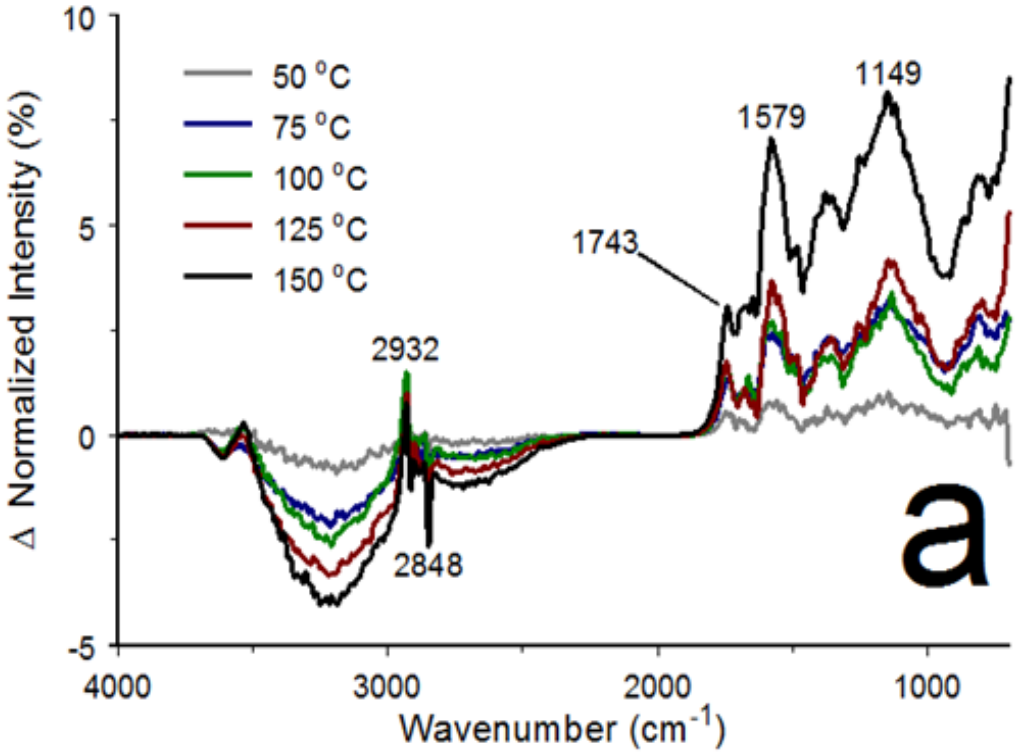

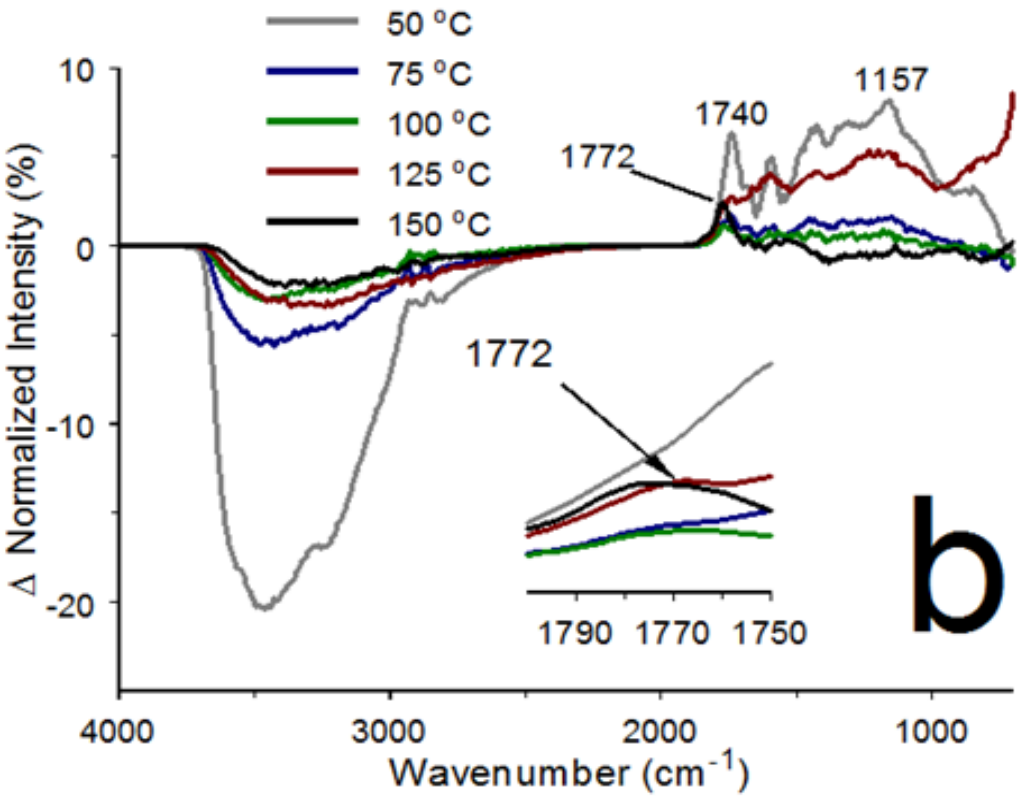

Figure 4.20: Incremental (a) reversible and (b) irreversible spectrum changes resulting from heating the lignite coal sample sequentially from 25 °C to each of the designated step temperatures.

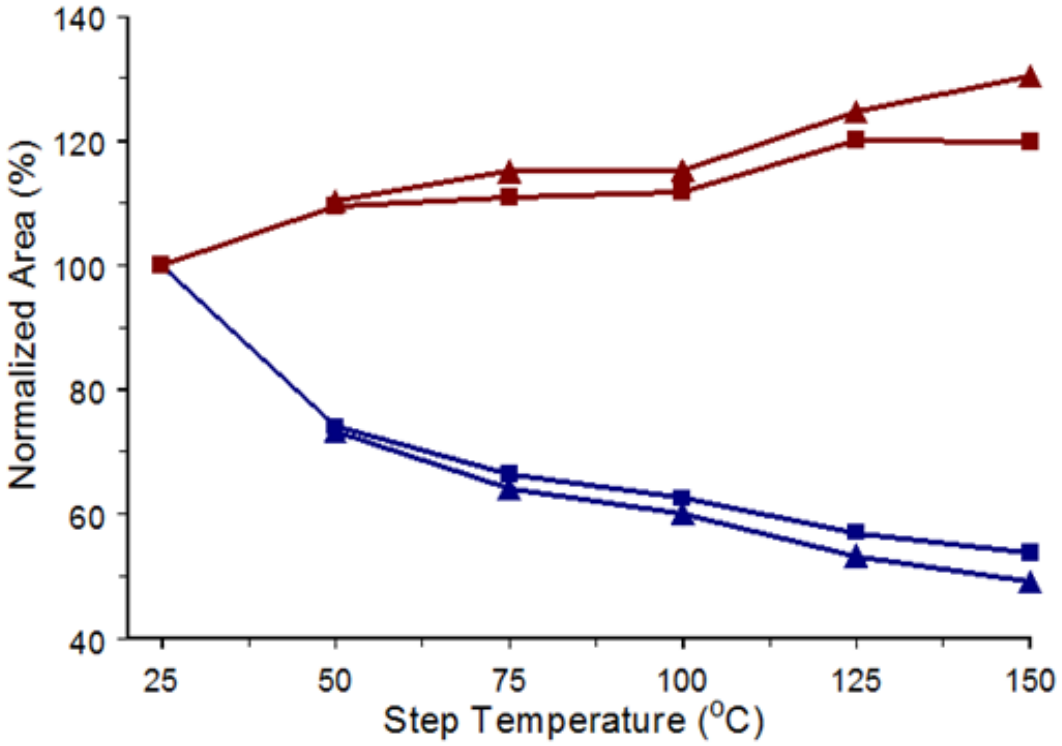

Figure 4.21: Infrared band areas for the 2000–700 cm^{-1} (red) and 3600–2000 cm^{-1} (blue) ranges plotted as a function of lignite coal step temperature.

The cumulative reversible infrared spectrum changes in Figure 4.19b (blue line) and the stepwise reversible changes in Figure 4.20 reveal that at 2925 and 2850 cm^{-1}, the C-H stretching vibration band intensities changed in opposite directions when the sample temperature increased. Figure 4.22 shows plots of the intensities at these wavenumbers as a function of step temperature. Like Figure 4.21, squares represent intensities in spectra measured at 25 °C and triangles denote intensities in spectra obtained at each of the step temperatures. The plot trends confirm that the 2925 cm^{-1} band intensity increased, whereas the 2850 cm^{-1} band intensity decreased with increasing sample temperature. The increasing

divergence of the $T_{Low}(n+1)$ (i.e., 25 °C) spectrum intensities from their initial values after heating the sample to higher step temperatures indicates that some of this intensity variation was irreversible on the time frame of the spectrum measurements. Apparently, the lignite coal sample was altered by temperature changes in a manner that caused the magnitudes of the vibration dipole moment oscillations for the asymmetric CH_2 vibration to increase while the symmetric CH_2 vibration dipole moment changes decreased. Additional information is needed to better understand this trend.

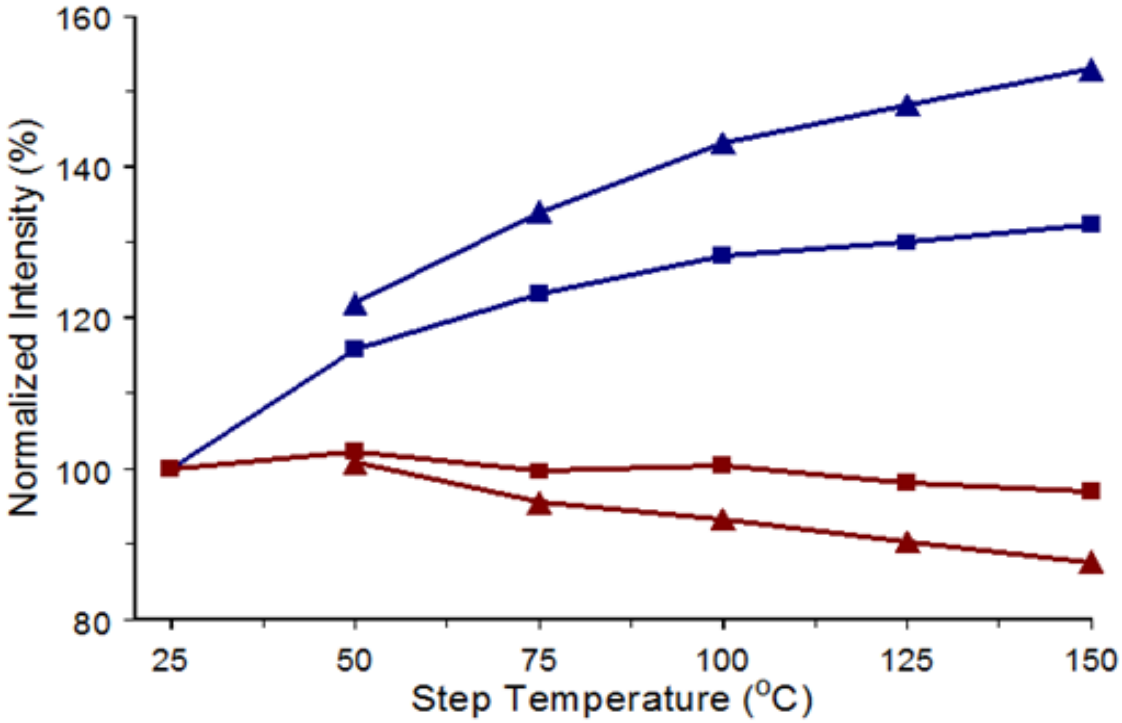

Figure 4.22: Normalized infrared spectrum intensities at 2850 cm^{-1} (red) and 2925 cm^{-1} (blue) as a function of lignite coal step temperature. Triangles represent intensities in spectra measured at the step temperatures and squares represent intensities in spectra obtained after subsequently cooling to 25 °C.

Figure 4.23a shows bituminous coal infrared spectra obtained initially (blue) and after heating the sample to 150 °C (red). Compared to the lignite results, the bituminous coal spectra exhibited a much lower O-H stretching vibration band intensity. Vibration bands below 2000 cm^{-1} associated with organic functionalities were sharper and better resolved. Differences between the bituminous and lignite coal spectra are consistent with a lower organic material content for the higher rank bituminous coal sample. Unlike the lignite spectra, the bituminous coal spectra contained sharp peaks above 3600 cm^{-1} that can be assigned to hydroxyl groups that are not involved in significant hydrogen bonding interactions.[252] These hydroxyl groups are likely associated with clay mineral impurities.[246] The ca. 8% intensity at 3690 cm^{-1} in Figure 4.23a suggests that these impurities represent minor components of the coal sample. Figure 4.23b is an overlay of the cumulative reversible (blue) and irreversible (red) spectrum differences resulting from heating the bituminous coal to 150 °C. Reversible changes included O-H stretching vibration band intensity loss at 3697 cm^{-1} and gain at 3682 cm^{-1}, a broad O-H stretching vibration band intensity loss with minimum at 3272 cm^{-1}, and various intensity gains and losses below 2000 cm^{-1}. The sharp peaks at 3697 and 3682 cm^{-1} in the blue difference spectrum in Figure 4.23b represent changes to narrow regions of the 3690 cm^{-1} O-H stretching vibration band in Figure 4.23a.

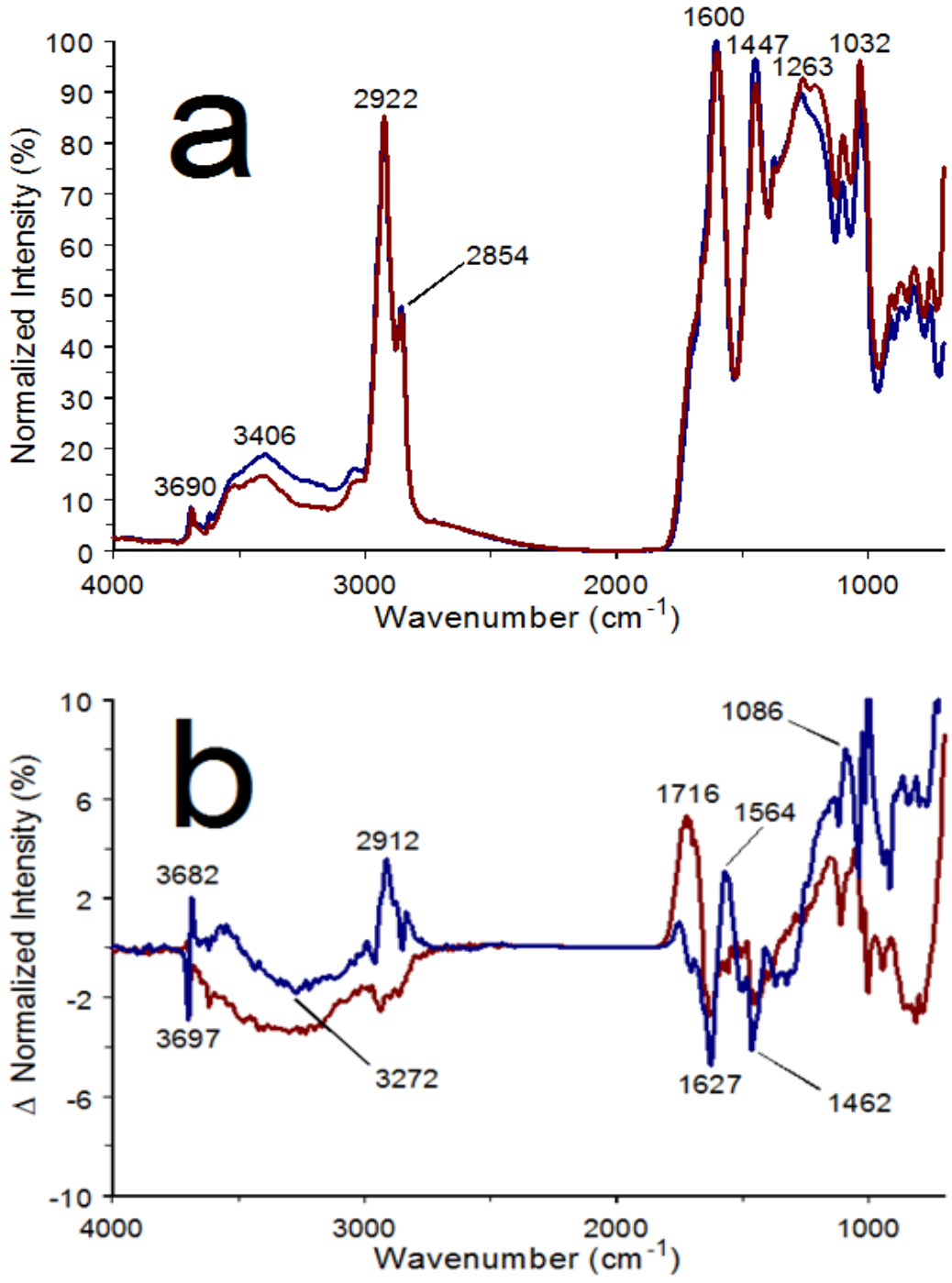

Figure 4.23: (a) Infrared spectra of bituminous coal obtained at 25 °C (blue) and 150 (red) °C. (b) Reversible (blue) and irreversible (red) spectrum changes resulting from heating bituminous coal from 25 to 150 °C.

Figure 4.24 shows plots of the band maximum wavenumber for this peak in the measured spectra as a function of sample temperature. The triangles show that the band maximum gradually shifted to lower wavenumbers with increasing sample temperature. This shift was a consequence of the increasing intensity loss at 3697 and gain at 3682 cm^{-1} with increasing temperature, causing the peak maximum to gradually shift to lower wavenumbers. After cooling from each $T_{High}(n)$ step, the trend for the $T_{Low}(n+1)$ spectra (squares) in Figure 4.24 reveals that the band maximum at 25 °C increased slightly after successive heating steps, indicating that the structure change responsible for this wavenumber shift was not completely reversible.

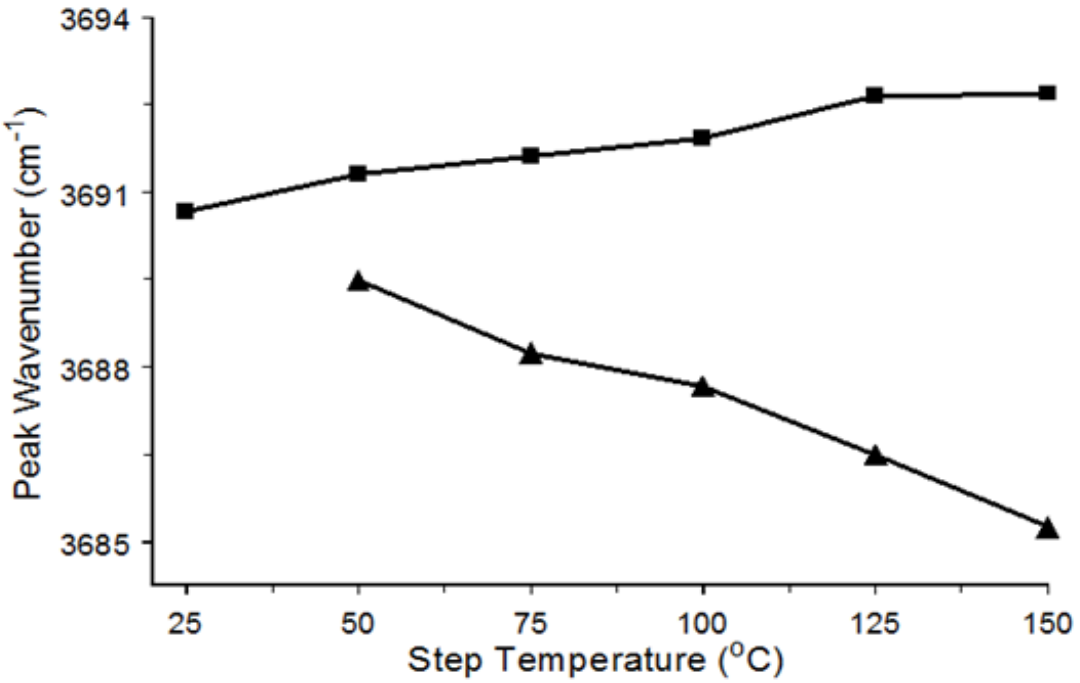

Figure 4.24: Bituminous coal 3690 cm^{-1} band maximum variations in spectra obtained at each step temperature (triangles) and after cooling to 25 °C (squares).

Figure 4.25 shows the incremental reversible and irreversible spectrum changes detected after applying the step-up/down temperature program. The reversible intensity decrease at 1627 cm^{-1} was most likely associated with loss of water at 150 °C that returned to the sample after cooling. The remaining reversible spectrum changes were either due to loss of interactions with the water that was removed by dehydration or bands arising from vibrations for which the dipole moment change was temperature-dependent. The reversible difference spectrum in Figure 4.23b exhibits a broad-band intensity loss that was slightly greater than in the reversible spectrum. Like the lignite coal cumulative irreversible spectrum, the mainly positive difference spectrum residuals below 2000 cm^{-1} were likely the result of loss of hydrogen bonding interactions between water and polar organic groups.

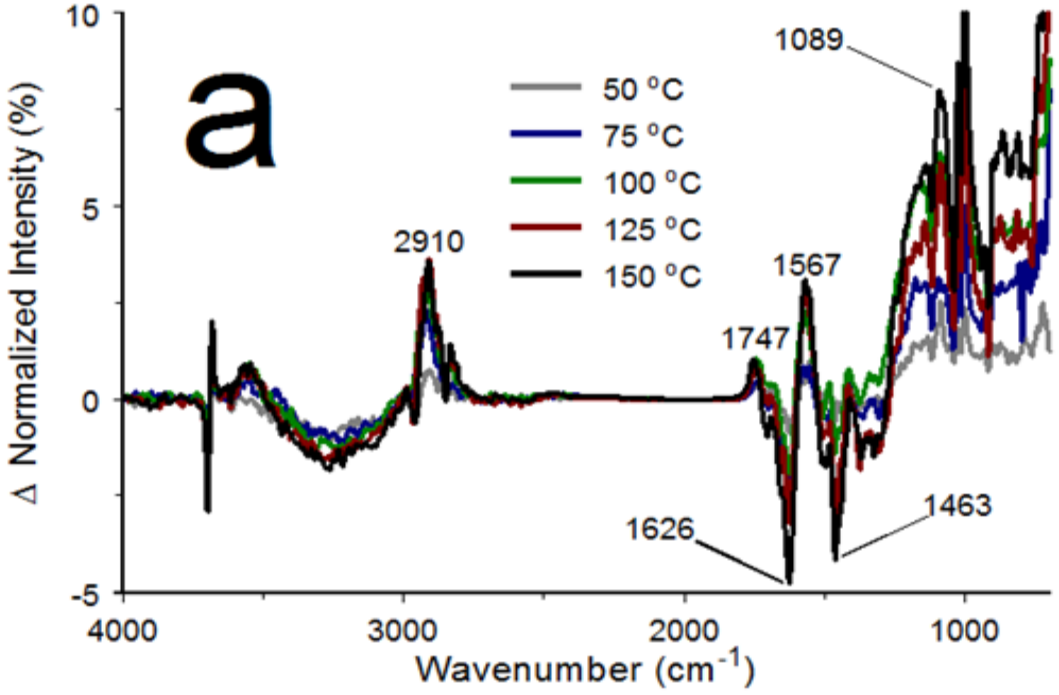

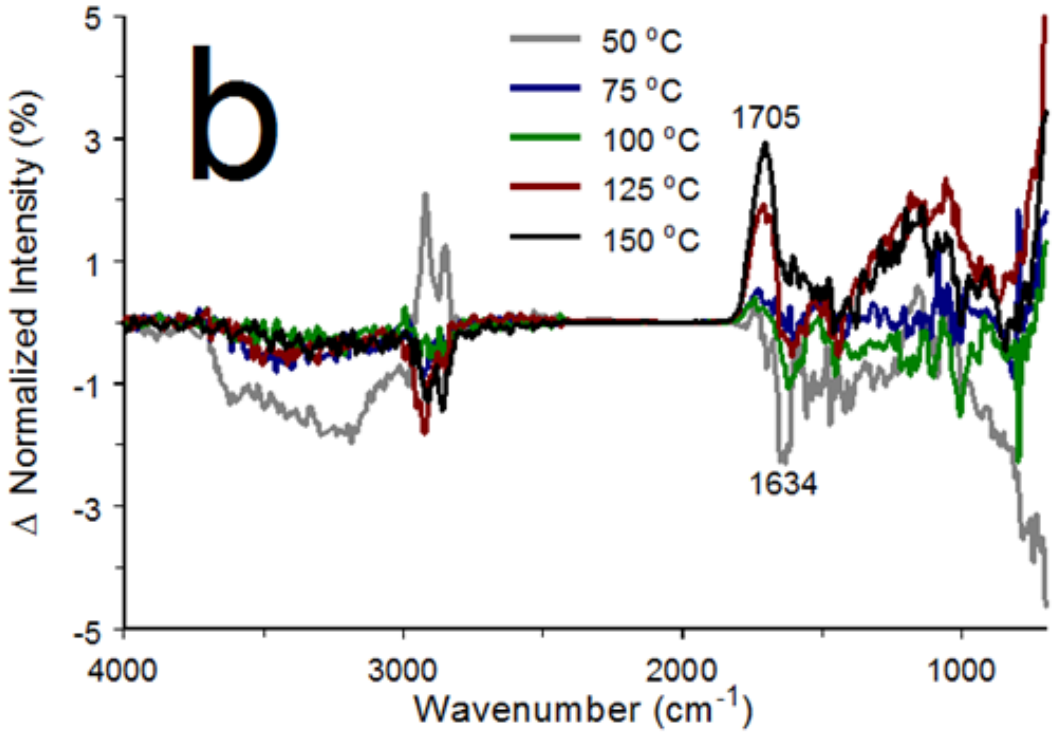

Figure 4.25: Incremental (a) reversible and (b) irreversible spectrum changes resulting from heating the bituminous coal sample to each step temperature.

4.5 Summary and Conclusions

The experimental results derived from the mineral studies described here illustrate the utility of temperature perturbation infrared spectroscopy. The high thermal conductivity of the button sample holder facilitates efficient heat transfer to and from the thermoelectric devices used for heating and cooling, permitting rapid temperature adjustments. This facilitates temperature step programming with minimal “dead time” between spectrum measurements. The sample temperature measurement accuracy and the inherent reproducibility of the FTIR interferometer

scanning results in successive infrared spectrum measurements with high reproducibility.

The temperature perturbation infrared spectroscopy results for crystalline minerals would be expected to follow trends like those exhibited by α-quartz. The 150 °C maximum sample temperature should be insufficient to permanently alter the crystal structures of most minerals. Consequently, infrared difference spectra would contain mostly reversible residuals that provide information regarding unit cell distortions caused by crystal structure thermal expansions and contractions.

Many IMA designated minerals contain water.[198] Water molecules can be incorporated as part of the mineral crystal structure, trapped within void spaces, or adsorbed to mineral surfaces. The temperature perturbation infrared spectroscopy results described here for the silica gel, montmorillonite clay, and gypsum samples exemplify what may be expected for analyses of other hydrated minerals. Infrared difference spectrum features attributed to water loss should be irreversible if measurements are made in a dry (e.g., 0% humidity) atmosphere. Band shapes and intensity versus temperature trends should be related to water molecule binding interactions.

Samples can contain inorganic minerals mixed with organic substances. For example, the 8% relative intensity O-H stretching vibration band at 3690 cm^{-1} in bituminous coal spectra was indicative of small quantities of inorganic oxides present in this heterogeneous material. Temperature perturbation infrared

spectroscopy measurements provided sufficient infrared spectrum measurement sensitivity to reveal the temperature-dependent trends for this low intensity band (Figure 4.24). In general, the analysis results obtained for the low-rank coals described here should be characteristic of those expected for heterogeneous mixtures of minerals and organics, such as soils. Temperature perturbation infrared spectroscopy should readily detect organic material oxidations after prolonged exposures to high temperature in a dry air environment.

Variable temperature infrared spectroscopy provides structure-specific sample information that is not readily apparent in isothermal spectrum measurements. For crystalline minerals, changing the sample temperature induces bond length and angle changes in the structure of the material. These changes result in subtle infrared spectrum functional group vibration band wavenumber shifts and/or band intensity variations. As shown here, a sample temperature perturbation methodology can be employed to detect these small infrared spectrum variations. When minerals consist of multiple components bound together by intermolecular interactions, temperature changes can alter the strengths of these interactions. Like bond length and/or angle changes, variations in constituent interaction strengths can alter sample vibrations, which can be detected by infrared spectroscopy. Thus, variable temperature infrared spectroscopy can provide information regarding temperature-dependent changes to constituent binding interactions. If sufficient energy is provided by sample

heating, constituent binding interactions can be overcome completely, resulting in sample mass losses. The resulting sample composition variations would be identified as irreversible changes in measured infrared spectra.

The minerals selected for the studies described here have been extensively studied by infrared spectroscopy. Consequently, infrared spectrum band assignments for these substances are readily available. These band assignments are used to associate infrared spectrum variations with specific atomic motions in the sample structure. To maximize the sample-dependent information that can be extracted from variable temperature difference spectra, the dependencies of infrared vibration band intensities on temperature must be investigated in greater detail for a wide variety of materials. The development of new molecular modeling tools to aid in predicting temperature-dependent infrared spectrum band shape variations and wavenumber shifts would also be helpful.

Chapter 5: Conclusions and Looking Forward

Infrared (IR) spectroscopy is a swift and non-destructive method allowing researchers to probe molecular structures via the interactions between infrared radiation and polarizable bonds within samples. Despite its widespread popularity in commercial, regulatory, and academic research spaces, innovations of the technique have largely stagnated since the 1960's. This body of work describes a new methodological approach to infrared spectroscopic investigation of materials: Button-IR. Button sample holder design, analytical capabilities, working principle, sampling optimizations and considerations, and mineralogical applications of this sampling method for mid-IR spectroscopy are addressed here.

The Button-IR technique is compatible with solid, liquid, and paste samples. It is capable of both qualitative and quantitative analysis. This technique requires minimal sample processing and is user friendly. The stainless-steel construction and low fabrication costs for button sample holders provide a robust, durable, and "green" alternative to salt windows and ATR-IR crystals, which can be costly and difficult to maintain. They permit neat sample analyses, thus alleviating concerns about chemically reactive samples or spectral artifacts due to sample preprocessing with infrared transparent salts. Button sample holders are easily cleaned with mild soap solutions and ultrasonication yet are durable enough to withstand harsher cleaning methods with mild acids if needed.

It is important to align and maintain alignment of instrument optics throughout diffuse reflection spectra data acquisition to reproducibly obtain accurate spectra. Proper alignment assures that the sample is in the focus of the infrared source radiation beam and avoids spectral artifacts. The maximum depth of the button mesh, alignment pins, standard and rotation slides, and adjustable slide positioner (screw) allow for consistent placement of samples along both the x and y planes.

The best quality VT-DRIFTS spectra were obtained after the button sample holder was adjusted respective to all optical system components in order to achieve the largest interferogram detector signal. Thus, the same components that allow for reproducible placement: the variability of mesh sizes, button rotation angle, slide positioner, and sample loading depth, allow for tunable alignment for maximum single beam emissivity. Additional studies of how the rotation angle affects the amount of radiation collected and delivered to the detector are needed but may require different optical components. In fact, a further exploration of how this tunability impacts spectral features is warranted.

The mesh component of the button sample holder is uniquely suited for direct sample collection through abrasion and affords safe sample storage and transport. Additionally, the mesh serves a dual purpose as a particle sieve, preferentially selecting sample particles that fit within the void spaces, thus eliminating the need for time consuming sample homogenization. This capability

is not possible with other infrared sampling methods and can be tuned by the choice of mesh for each button. Additional sample loading techniques, such as sputter coating, may provide thinner and more uniform layers.

The ability of the button mesh to collect, trap, and store nanogram quantities of sample material make it particularly useful for samples where preservation and repeated analyses are desired. For example, Button-IR would be uniquely suited for characterization of archaeological residues in museum collections. Tiny amounts of sample could be collected inconspicuously, thus maintaining the cultural integrity of the objects. These samples could then be analyzed repeatedly for future studies without need for re-sampling.

Button-IR also shows great promise for in-situ studies. The small size and durability of the button sample holders could be adapted for use with compact portable infrared spectrometers for field-based research. They could provide rapid on-site characterization of forensic samples as well as repeated assays of the same sample later in a laboratory setting, which is not possible with ATR-IR or other currently used methods. Investigators would simply need to collect and store the sample on a single sterilized button. The rigidity and durability of the button sample holder also allows transport and long-term storage under cold or anaerobic conditions, preventing sample degradation. This has the potential to improve forensic cold case outcomes.

As demonstrated in this dissertation, Button-IR can be used for both traditional (DRIFTS) and variable temperature (VT-DRIFTS) diffuse reflectance infrared Fourier transform spectroscopy. Two heating techniques were employed with button sample holders for variable temperature studies – heating the button and sample through contact with heated purge gas and direct heating of the button and sample with thermoelectric cooling (TEC) chips. The latter method yielded similar high quality spectral results but offered enhanced temperature control. The TEC heating and cooling apparatus provided localized heating of the sample with little adverse optical alignment effects due to thermal expansion of the sample chamber. Indeed, the heating was so localized that no heat could be felt when placing a finger directly above a 150 ^{o}C button. This attribute, combined with a closed sample chamber, may allow for a unique method of probing band gap energy of neat semiconductor materials. The TEC chips also enabled unique heating and cooling profiles, permitting rapid targeted investigations of reversible and irreversible temperature-dependent structural changes in samples.

The TEC stack heating and cooling block controls isothermal sample temperatures to within ± 0.1 ^{o}C. Heating and cooling rates exceeding 2 ^{o}C/s could be sustained between 0 and 150 ^{o}C allowing sample temperature to be changed between -40 °C and 150 °C in a matter of seconds. This rate of sample temperature change has not been achievable in traditional VT-DRIFTS and theoretically provides more refined and accurate temperature measurements at which

structural changes are detected. Results obtained when using the dual stack TEC block are limited to -55 °C due to the cooling capacity afforded by the individual chips. Excessively high temperatures (> 150 °C) were purposely avoided in the studies outlined here to prevent oxidation of the stainless-steel button under dry air purge. Multi-stack blocks, TEC chips with enhanced component durability, high temperature button materials, and properly designed evacuated environments could expand the VT-DRIFTS temperature range and facilitate studies at higher temperatures. The VT-DRIFTS apparatus could be connected to evolved gas analysis methods such as mass spectrometry to provide complementary information regarding gaseous chemical reaction products. It may also be possible to combine thermogravimetric analysis with VT-DRIFTS. Extending the upper temperature limit for VT-DRIFTS would be of great utility in green chemistry processing research and materials engineering explorations.

Additional sample perturbations should be explored with the Button-IR technique. For example, purge gas compositions could be slowly varied to investigate specific gas/solid chemical reactions. Infrared spectra could be measured while exposing samples to other radiation sources, such as UV light to study organic pigment degradation or resin curing. Additionally, hyphenated analyses are possible with Button-IR. Real-time infrared monitoring of dissolved solids or liquid compositions could be implemented by combining liquid chromatography with collecting fractions on button sample holders that could be

employed for subsequent infrared analyses. Such applications may result in more rapid response times in water treatment, medical diagnostics, materials research, and fundamental sample preparation and extraction applications. Coupling Button-IR with laser ablation may be used to generate new volatiles that can be used to probe sample structure and reactivity.

Button sample holders show potential for high throughput and chemical mapping applications. The choice of mesh size determines the number of voids, or sample wells per square inch. Thus, by pressing the mesh into a sample, rather than abrading the surface, it is theoretically possible to collect discreet samples isolated in each well. By using microscopic imaging and nano-FTIR, spatially resolved images that map the distribution of different chemical compounds or functional groups within a sample could be derived. This visualization of chemical composition and heterogeneity would be particularly useful in biochemical tissue research studies, such as mapping the locations of cancer cells in biopsy samples.

Although the studies described here were performed in the mid-infrared region, button sample holders should be applicable in most wavelength regions. For example, after optimizing the button material or overall shape, it may be compatible with scanning electron microscopy (SEM), focused ion beam (FIB), and scanning transmission electron microscopy (STEM) analyses.

Kubelka-Munk units were used to represent powdered sample spectra. The Kubelka-Munk theory predicts a linear relationship between spectral output and

sample concentration with an assumed constant scattering coefficient, sample dilution in a non-absorbing matrix, and an infinitely thick sample layer. The highest quality spectra obtained by using Button-IR, however, were obtained when samples consisted of neat particles with diameters of a few microns organized in thin layers. Further studies are warranted to discover why the Kubelka-Munk function, which is derived assuming sample properties that differ significantly from those employed here, has been found to yield more accurate results than apparent absorbance (-log(R)).

Button-IR offers an appealing alternative to commercially available methods. These sample holders are low cost, durable, and damage resistant after repeated analyses and cleaning cycles, making them an affordable and environmentally friendly option. Minimal sample preparation is required, making it competitive with the ATR-IR method. Samples that may damage or permanently contaminate ATR crystals could be analyzed by Button-IR instead. Its utility has been extensively demonstrated for powder samples. However, little has been done to explore its applicability for studies of liquids, pastes, and greases. Based on the results described here, the Button-IR method may provide significant improvements compared to current methods for infrared analyses of these materials. Therefore, benchmark studies for these types of samples should be considered.

References

1. Ingle, J. D.; Crouch, S. R., *Spectrochemical Analysis*. Prentice Hall: Englewood Cliffs, NJ 07632, 1988; p 614.

2. Newton, I., *Opticks : Or, a Treatise of the Reflexions, Refractions, Inflexions and Colours of Light. Also Two Treatises of the Species and Magnitude of Curvilinear Figures.* . printed for Sam. Smith, and Benj. Walford, Printers to the Royal Society, at the Prince's Arms in St. Paul's Church-Yard,: London, MDCCIV. 1704.

3. Kakkar, R., *Atomic and Molecular Spectroscopy*. 2015.

4. Stevens, R. W.; Siriwardane, R. V.; Logan, J., In Situ Fourier Transform Infrared (FTIR) Investigation of CO2 Adsorption onto Zeolite Materials. *Energy & Fuels* **2008,** *22* (5), 3070-3079.

5. Ioakeimidis, C.; Fotopoulou, K. N.; Karapanagioti, H. K.; Geraga, M.; Zeri, C.; Papathanassiou, E.; Galgani, F.; Papatheodorou, G., The degradation potential of PET bottles in the marine environment: An ATR-FTIR based approach. *Sci. Rep.-UK* **2016,** *6* (1), 23501.

6. Renner, G.; Sauerbier, P.; Schmidt, T. C.; Schram, J., Robust Automatic Identification of Microplastics in Environmental Samples Using FTIR Microscopy. *Anal. Chem.* **2019,** *91* (15), 9656-9664.

7. Noneman, H. F.; Hollingsworth, M. E.; Singh, J.; White, R. L., A high sensitivity variable temperature infrared spectroscopy investigation of kaolinite structure changes. *Spectrochim Acta A Mol Biomol Spectrosc* **2021,** *247*.

8. Noneman, H. F.; White, R. L., Temperature Perturbation Infrared Spectroscopy of Minerals. *Minerals* **2024,** *14* (6), 624.

9. Angell, C. L.; Schaffer, P. C., Infrared Spectroscopic Investigations of Zeolites and Adsorbed Molecules. I. Structural OH Groups[1]. *J. Phys. Chem.* **1965,** *69* (10), 3463-3470.

10. Beauvais, C.; Boutin, A.; Fuchs, A. H., Adsorption of water in zeolite sodium-faujasite: A molecular simulation study. *Comptes Rendus Chimie* **2005,** *8* (3), 485-490.

11. Bellat, J.-P.; Paulin, C.; Jeffroy, M.; Boutin, A.; Paillaud, J.-L.; Patarin, J.; Di Lella, A.; Fuchs, A., Unusual Hysteresis Loop in the Adsorption–Desorption of Water in NaY Zeolite at Very Low Pressure. *J. Phys. Chem. C* **2009,** *113* (19), 8287-8295.

12. Beta, I. A.; Böhlig, H.; Hunger, B., Structure of adsorption complexes of water in zeolites of different types studied by infrared spectroscopy and inelastic neutron scattering. *Physical Chemistry Chemical Physics* **2004,** *6* (8), 1975-1981.

13. Breck, D. W. Crystalline zeolite y. US3130007A, 1964/04/21, 1964.

14. Bushuev, Y. G.; Sastre, G.; de Julián-Ortiz, J. V., The Structural Directing Role of Water and Hydroxyl Groups in the Synthesis of Beta Zeolite Polymorphs. *J. Phys. Chem. C* **2010,** *114* (1), 345-356.

15. Flanigen, E. M.; Khatami, H.; Szymanski, H. A., Infrared Structural Studies of Zeolite Frameworks. In *Molecular Sieve Zeolites-I*, 1974; Vol. 101, pp 201-229.

16. Singh, J.; White, R. L., A variable temperature infrared spectroscopy study of NaA zeolite dehydration. *Vibrational Spectroscopy* **2018,** *94*, 37-42.

17. Singh, J.; White, R. L., A variable temperature infrared spectroscopy study of NaY zeolite dehydration. *Spectrochim Acta A Mol Biomol Spectrosc* **2020,** *231*, 118142.

18. Moss, D. A.; Keese, M.; Pepperkok, R., IR microspectroscopy of live cells. *Vib. Spectrosc.* **2005,** *38* (1), 185-191.

19. Derenne, A.; Gasper, R.; Goormaghtigh, E., The FTIR spectrum of prostate cancer cells allows the classification of anticancer drugs according to their mode of action. *Analyst* **2011,** *136* (6), 1134-1141.

20. Shapaval, V.; Walczak, B.; Gognies, S.; Møretrø, T.; P. Suso, H.; Åsli, A. W.; Belarbi, A.; Kohler, A., FTIR spectroscopic characterization of differently cultivated food related yeasts. *Analyst* **2013,** *138* (14), 4129-4138.

21. Anjos, O.; Campos, M. G.; Ruiz, P. C.; Antunes, P., Application of FTIR-ATR spectroscopy to the quantification of sugar in honey. *Food Chem.* **2015,** *169*, 218-223.

22. Balan, B.; Dhaulaniya, A. S.; Jamwal, R.; Amit; Sodhi, K. K.; Kelly, S.; Cannavan, A.; Singh, D. K., Application of Attenuated Total Reflectance-Fourier Transform Infrared (ATR-FTIR) spectroscopy coupled with chemometrics for detection and quantification of formalin in cow milk. *Vib. Spectrosc.* **2020,** *107*, 103033.

23. Amorim, T. L.; Fuente, M. A. d. l.; Oliveira, M. A. L. d.; Gómez-Cortés, P., ATR-FTIR and Raman Spectroscopies Associated with Chemometrics for Lipid Form Evaluation of Fish Oil Supplements: A Comparative Study. *ACS Food Sci. Technol.* **2021,** *1*(3), 318-325.

24. Degnan, T. F., Applications of zeolites in petroleum refining. *Topics in Catalysis* **2000,** *13* (4), 349-356.

25. Ferrer, N., Handbook of instrumental techniques from CCiTUB: Applications of Fourier transform infrared spectroscopy. Molecular, U. d. A., Ed. CCiTUB, Universitat de Barcelona: 2012.

26. Amato, S. R.; Bersani, D.; Lottici, P. P.; Pogliani, P.; Pelosi, C., A Multi-Analytical Approach to the Study of the Mural Paintings in the Presbytery of Santa Maria Antiqua Al Foro Romano in Rome. *Archaeometry* **2017,** *59* (6), 1050-1064.

27. Beltran, V.; Salvadó, N.; Butí, S.; Cinque, G., Micro infrared spectroscopy discrimination capability of compounds in complex matrices of thin layers in real sample coatings from artworks. *Microchemical Journal* **2015,** *118*, 115-123.

28. Daveri, A.; Malagodi, M.; Vagnini, M., The Bone Black Pigment Identification by Noninvasive, In Situ Infrared Reflection Spectroscopy. *J Anal Methods Chem* **2018,** *2018*, 6595643.

29. Manso, M.; Le Gac, A.; Longelin, S.; Pessanha, S.; Frade, J. C.; Guerra, M.; Candeias, A. J.; Carvalho, M. L., Spectroscopic characterization of a masterpiece: the Manueline foral charter of Sintra. *Spectrochim Acta A Mol Biomol Spectrosc* **2013,** *105*, 288-96.

30. Miguel, C.; Lopes, J. A.; Clarke, M.; Melo, M. J., Combining infrared spectroscopy with chemometric analysis for the characterization of proteinaceous binders in medieval paints. *Chemom. Intell. Lab. Syst.* **2012,** *119*, 32-38.

31. Patricia L. Lang, H. F. N., The Long-term Love Affair with Infrared Spectroscopy and Medieval Pigments: A Review. In *Archaeological chemistry: a multidisciplinary analysis of the past*, Orna, V., Ed. 2020.

32. Paula, P. A. J. d., Elements of Physical Chemistry. Fifth ed.; Oxford University Press: Great Britain, 2009; p. 600.

33. Jr., J. I. K. T. J. K. D. R. C., Basic Principles of Forensic Chemistry. Springer, Humana Press: New York, New York, 2011; p. 360. 10.1007/978-1-59745-437-7

34. Herschel, W., On the rays which occasion heat. *Philosophical Transactions of the Royal Society* **1800,** *80*, 284

35. Coblentz, W. W., Investigations of Infrared Spectra Part 1. *Carnagie Institute of Washington* **1905,** *35*.

36. Abney, C.; Lieut.-Colonel, F., On the Influence of the Atomic Grouping in the Molecules of Organic Bodies on Their Absorption in the Infra-Red Region of the Spectrum. *Philosophical Transactions of the Royal Society of London* **1881,** *172*, 887-918.

37. Michelson, A. A.; Morley, E. W., On the relative motion of the Earth and the luminiferous ether. *American Journal of Science* **1887,** *s3-34* (203), 333-345.

38. Sommer, A. J., Infrared Spectroscopy. In *Spectroscopy: Introduction to the Techniques and Recent Advances The SciX 2020 Preview and Companion Guide*, Spectroscopy: 2020 SciX Conference, 2020.

39. Lopes, C. d. C. A.; Limirio, P. H. J. O.; Novais, V. R.; Dechichi, P., Fourier transform infrared spectroscopy (FTIR) application chemical characterization of enamel, dentin and bone. *Applied Spectroscopy Reviews* **2018,** *53* (9), 747-769.

40. Girard, J.-P.; Freyssinet, P.; Chazot, G., Unraveling climatic changes from intraprofile variation in oxygen and hydrogen isotopic composition of goethite and kaolinite in laterites: an integrated study from Yaou, French Guiana. *Geochimica et Cosmochimica Acta* **2000,** *64* (3), 409-426.

41. Li, S.; Ju, H.; Ji, M.; Zhang, J.; Song, K.; Chen, P.; Mu, G., Terrestrial humic-like fluorescence peak of chromophoric dissolved organic matter as a new potential indicator tracing the antibiotics in typical polluted watershed. *J Environ Manage* **2018,** *228*, 65-76.

42. Alqahtani, F. K.; Rashid, K.; Zafar, I.; Iqbal Khan, M.; Ababtain, A. A., Production of sustainable green mortar by ultrahigh utilization of fly ash: Technical, economic and environmental assessment. *Construction and Building Materials* **2021,** *281*.

43. Al-Sharji, D.; Amin, M. O.; Lednev, I. K.; Al-Hetlani, E., Detection of Oral Fluid Stains on Common Substrates Using SEM and ATR-FTIR Spectroscopy for Forensic Purposes. *ACS Omega* **2024,** *9* (28), 30142-30150.

44. Mifsud, D. V.; Juhász, Z.; Herczku, P.; Kovács, S. T. S.; Ioppolo, S.; Kaňuchová, Z.; Czentye, M.; Hailey, P. A.; Muiña, A. T.; Mason, N. J.; McCullough, R. W.; Paripás, B.; Sulik, B., Electron irradiation and thermal chemistry studies of interstellar and planetary ice analogues at the ICA astrochemistry facility. *The European Physical Journal D* **2021,** *75* (6).

45. Moore, M. H.; Ferrante, R. F.; James Moore, W.; Hudson, R., INFRARED SPECTRA AND OPTICAL CONSTANTS OF NITRILE ICES RELEVANT TO TITAN's ATMOSPHERE. *The Astrophysical Journal Supplement Series* **2010,** *191* (1), 96-112.

46. Nellessen, M. A.; Gasda, P.; Crossey, L.; Peterson, E.; Ali, A.; Zhang, J.; Zhou, W.; Hao, M.; Spilde, M.; Newsom, H.; Lanza, N.; Reyes-Newell, A.; Legett, S.; Das, D.; Delapp, D.; Yeager, C.; Labouriau, A.; Clegg, S.; Wiens, R. C., Boron adsorption in clay minerals: Implications for martian groundwater chemistry and boron on Mars. *Icarus* **2023,** *401*.

47. Morlok, A.; Klemme, S.; Weber, I.; Stojic, A.; Sohn, M.; Hiesinger, H.; Helbert, J., Mid-infrared spectroscopy of planetary analogs: A database for planetary remote sensing. *Icarus* **2019,** *324*, 86-103.

48. Izzo, F.; Germinario, C.; Grifa, C.; Langella, A.; Mercurio, M., External reflectance FTIR dataset (4000–400 cm−1) for the identification of relevant mineralogical phases forming Cultural Heritage materials. *Infrared Physics & Technology* **2020,** *106*.

49. Wu, S., Infrared Spectrometry. University of Oklahoma: 2019.

50. Feng, X.; Larson, R. A.; Digman, M. F., Evaluation of Near-Infrared Reflectance and Transflectance Sensing System for Predicting Manure Nutrients. *Remote Sensing* **2022,** *14* (4).

51. Hanifi, A.; McGoverin, C.; Ou, Y. T.; Safadi, F.; Spencer, R. G.; Pleshko, N., Differences in infrared spectroscopic data of connective tissues in transflectance and transmittance modes. *Anal Chim Acta* **2013,** *779*, 41-9.

52. Wold, J. P.; Johansen, I.-R.; Haugholt, K. H.; Tschudi, J.; Thielemann, J.; Segtnan, V. H.; Narum, B.; Wold, E., Non-Contact Transflectance near Infrared Imaging for Representative on-Line Sampling of Dried Salted Coalfish (Bacalao). *Journal of Near Infrared Spectroscopy* **2006,** *14* (1), 59-66.

53. Pilling, M. J.; Bassan, P.; Gardner, P., Comparison of transmission and transflectance mode FTIR imaging of biological tissue. *Analyst* **2015,** *140* (7), 2383-92.

54. Chalmers, J. M.; Everall, N. J.; Ellison, S., Specular reflectance: A convenient tool for polymer characterization by FTIR-microscopy? *Micron* **1996,** *27* (5), 315-328.

55. Voyiatzis, G. A.; Andrikopoulos, K. S.; Papatheodorou, G. N.; Kamitsos, E. I.; Chryssikos, G. D.; Kapoutsis, J. A.; Anastasiadis, S. H.; Fytas, G., Polarized Resonance Raman and FTIR Reflectance Spectroscopic Investigation of the Molecular Orientation in Industrial Poly(vinyl chloride) Specimens. *Macromolecules* **2000,** *33* (15), 5613-5623.

56. Mancini, D.; Percot, A.; Bellot-Gurlet, L.; Colomban, P.; Carnazza, P., On-site contactless surface analysis of modern paintings from Galleria Nazionale (Rome) by reflectance FTIR and Raman spectroscopies. *Talanta* **2021,** *227*, 122159.

57. Machefert, J. M.; Le Calvar, M.; Lenglet, M., FTIR study of nickel and copper oxidation: Theoretical approach and experience. *Surf. Interface Anal.* **1991,** *17* (3), 137-142.

58. Heimsath, A.; Lindner, P.; Klimm, E.; Schmid, T.; Moreno, K. O.; Elon, Y.; Am-Shallem, M.; Nitz, P., Specular reflectance of soiled glass mirrors – Study on the impact of incidence angles. In *AIP Conf. Proc*, AIP Publishing: 2016.

59. Bhatia, D.; Alam, M.; Sarkar, P. C., Specular reflectance and derivative spectrometric studies on lac-epoxy resin blends. *Pigment & Resin Technology* **2007,** *36* (1), 18-29.

60. Lane, M. D.; Glotch, T. D.; Dyar, M. D.; Pieters, C. M.; Klima, R.; Hiroi, T.; Bishop, J. L.; Sunshine, J., Midinfrared spectroscopy of synthetic olivines: Thermal emission, specular and diffuse reflectance, and attenuated total reflectance studies of forsterite to fayalite. *Journal of Geophysical Research* **2011,** *116* (E8).

61. Curtis, N. J.; Gascooke, J. R.; Pring, A., Silicon-Oxygen Region Infrared and Raman Analysis of Opals: The Effect of Sample Preparation and Measurement Type. *Minerals* **2021,** *11* (2).

62. Bliss, M.; Walden, B. L.; White, W. B., Measurement of Infrared Spectra of Dense Ceramics by Specular Reflectance Spectroscopy. *Journal of the American Ceramic Society* **2005,** *73* (4), 1078-1083.

63. Robert J. Lipert, B. D. L., and Marc D. Porter, Specular Reflection Spectroscopy. In *Modern Techniques in Applied Molecular Spectroscopy*, Mirabella, F. M., Ed. John Wiley & Sons, Inc: 1998; pp 83-126.

64. Okamura, H., A simple method for the Kramers-Kronig analysis of reflectance spectra measured with diamond anvil cell. *Journal of Physics: Conference Series* **2012,** *359*.

65. Harrick, N. J., Surface Chemistry Ffrom Spectral Analysis Of Totally Internally Reflected Radiation*. *The Journal of Physical Chemistry* **1960,** *64* (9), 1110-1114.

66. Chen, Y.; Mastalerz, M.; Schimmelmann, A., Characterization of chemical functional groups in macerals across different coal ranks via micro-FTIR spectroscopy. *International Journal of Coal Geology* **2012,** *104*, 22-33.

67. Chen, Y.; Zou, C.; Mastalerz, M.; Hu, S.; Gasaway, C.; Tao, X., Applications of Micro-Fourier Transform Infrared Spectroscopy (FTIR) in the Geological Sciences--A Review. *Int J Mol Sci* **2015,** *16* (12), 30223-50.

68. Smidt, E.; Schwanninger, M., Characterization of Waste Materials Using FTIR Spectroscopy: Process Monitoring and Quality Assessment. *Spectroscopy Letters* **2005,** *38* (3), 247-270.

69. Wang, X.; Bazuin, C. G.; Pellerin, C., Quantitative analysis of hydrogen bonding in electrospun fibers of poly(4-vinyl pyridine)/(4,4′-biphenol) complexes by ATR using liquid blends as models. *Vibrational Spectroscopy* **2014,** *71*, 18-23.

70. Hind, A. R.; Bhargava, S. K.; McKinnon, A., At the solid/liquid interface: FTIR/ATR--the tool of choice. *Adv Colloid Interface Sci* **2001,** *93* (1-3), 91-114.

71. Larkin, P., *Infrared and Raman Spectroscopy*. 2011.

72. M. Milosevic, S. L. B., A Review Of FT IR Diffuse Reflection Sampling Considerations. *Applied Spectroscopy Reviews* **2002,** *37* (4), 347-364.

73. White, C. E.; Provis, J. L.; Riley, D. P.; Kearley, G. J.; van Deventer, J. S., What is the structure of kaolinite? Reconciling theory and experiment. *J Phys Chem B* **2009,** *113* (19), 6756-65.

74. White, R. L., Diffuse reflection mid-infrared spectroscopy of neat powders by using a wire mesh "Button" sample holder. *Anal Chim Acta* **2020,** *1098*, 110-116.

75. Kubelka, P. M., Franz, An article on optics of paint layers. *Z. Tech. Phys.* **1931,** *12*, 593-601

76. Vesna Džimbeg-Malčić Željka Barbarić-Mikočević, K. I., Kubelka-Munk Theory In Describing Optical Properties of Paper (I). *Technical Gazette* **2011,** *18* (1), 117-124.

77. Sirita, J.; Phanichphant, S.; Meunier, F. C., Quantitative analysis of adsorbate concentrations by diffuse reflectance FT-IR. *Anal Chem* **2007,** *79* (10), 3912-8.

78. Law, D. P.; Blakeney, A. B.; Tkachuk, R., The Kubelka–Munk Equation: Some Practical Considerations. *Journal of Near Infrared Spectroscopy* **1996,** *4* (1), 189-193.

79. Dahm, D. J., Why Does the Kubelka—Munk Equation “Fail”? *NIR news* **2003,** *14* (2), 17-18.

80. Masserschmidt, I.; Cuelbas, C. J.; Poppi, R. J.; de Andrade, J. C.; de Abreu, C. A.; Davanzo, C. U., Determination of organic matter in soils by FTIR/diffuse reflectance and multivariate calibration. *Journal of Chemometrics* **1999,** *13* (3-4), 265-273.

81. Navas, N.; Romero-Pastor, J.; Manzano, E.; Cardell, C., Benefits of applying combined diffuse reflectance FTIR spectroscopy and principal component analysis for the study of blue tempera historical painting. *Anal Chim Acta* **2008,** *630* (2), 141-9.

82. White, R. L.; Ai, J., Variable-Temperature Diffuse Reflectance Infrared Studies of Calcium Oxalate Monohydrate. *Applied Spectroscopy* **1992,** *46* (1), 93-99.

83. White, R. L.; Ai, J., Effect of silica on the nonoxidative thermal degradation of poly(vinyl butyral). *Chemistry of Materials* **1992,** *4* (1), 233-239.

84. White, R. L.; Nair, A., Effect of silica on the thermal degradation of poly(vinyl butyral). *Chemistry of Materials* **1990,** *2* (6), 742-748.

85. White, R. L.; Nair, A., Diffuse Reflectance Infrared Spectroscopic Characterization of Silica Dehydroxylation. *Applied Spectroscopy* **1990,** *44* (1), 69-75.

86. Ingram, A. L.; Nickels, T. M.; Maraoulaite, D. K.; White, R. L. Variable Temperature Infrared Spectroscopy Studies of Aromatic Acid Adsorbate Effects on Montmorillonite Dehydration. *Applied Spectroscopy* **2017,** *71*(2), 238-249.

87. Maraoulaite, D. K.; Nickels, T. M.; Ingram, A. L.; White, R. L., VT-DRIFTS Investigations of Interactions Between Benzoic Acid and Montmorillonite Clay. *Spectroscopy* **2015,** *30* (10), 2-8.

88. Nickels, T. M.; Ingram, A. L.; Maraoulaite, D. K.; White, R. L., Variable Temperature Infrared Spectroscopy Investigations of Benzoic Acid Desorption from Sodium and Calcium Montmorillonite Clays. *Appl Spectrosc* **2015,** *69* (12), 1381-9.

89. Nickels, T. M.; Ingram, A. L.; Maraoulaite, D. K.; White, R. L., Variable Temperature Infrared Investigation of Benzoic Acid Interactions with Montmorillonite Clay Interlayer Water. *Applied Spectroscopy* **2015,** *69* (7), 850-6.

90. Nickels, T. M.; Maraoulaite, D. K.; Ingram, A. L.; White, R. L., Infrared Studies of Benzoic Acid Interactions with Montmorillonite Clay. In *248th ACS National Meeting & Exposition*, San Francisco, CA, United States, 2014; pp ANYL-226.

91. Singh, J.; White, R. L., A variable temperature infrared spectroscopy study of CaA zeolite dehydration and carbonate formation. *Spectrochimica Acta Part A: Molecular and Biomolecular Spectroscopy* **2019,** *207*, 189-196.

92. White, D. R.; White, R. L., Isoconversion effective activation energy profiles by variable temperature diffuse reflection infrared spectroscopy. *Appl Spectrosc* **2008,** *62* (1), 116-20.

93. Cervantes-Uc, J. M.; Cauich-Rodríguez, J. V.; Vázquez-Torres, H.; Garfias-Mesías, L. F.; Paul, D. R., Thermal degradation of commercially available organoclays studied by TGA–FTIR. *Thermochim. Acta* **2007,** *457* (1), 92-102.

94. Singh, S.; Wu, C.; Williams, P. T., Pyrolysis of waste materials using TGA-MS and TGA-FTIR as complementary characterisation techniques. *J. Anal. Appl. Pyrolysis* **2012,** *94*, 99-107.

95. Gosav, S.; Dinica, R.; Praisler, M., Choosing between GC–FTIR and GC–MS spectra for an efficient intelligent identification of illicit amphetamines. *J. Mol. Struct.* **2008,** *887* (1), 269-278.

96. Berdeaux, O.; Fontagné, S.; Sémon, E.; Velasco, J.; Sébédio, J. L.; Dobarganes, C., A detailed identification study on high-temperature degradation products of oleic and linoleic acid methyl esters by GC–MS and GC–FTIR. *Chem. Phys. Lipids* **2012,** *165* (3), 338-347.

97. Kuligowski, J.; Quintás, G.; Garrigues, S.; Lendl, B.; de la Guardia, M.; Lendl, B., Recent advances in on-line liquid chromatography - infrared spectrometry (LC-IR). *TrAC, Trends Anal. Chem.* **2010,** *29* (6), 544-552.

98. Jordan, S. L.; Taylor, L. T., HPLC Separation with Solvent Elimination FTIR Detection of Polymer Additives. *J. Chromatogr. Sci.* **1997,** *35* (1), 7-13.

99. Jansen, J. A. J., On-line liquid chromatography — Fourier transform infrared spectroscopy for the analysis of polymers and additives. *Fresenius J. Anal. Chem.* **1990,** *337* (4), 398-402.

100. Fahrenfort, J., Attenuated total reflection: A new principle for the production of useful infra-red reflection spectra of organic compounds. *Spectrochim. Acta* **1961,** *17* (7), 698-709.

101. Andrade, J.; Pereira, C. G.; Almeida Junior, J. C. d.; Viana, C. C. R.; Neves, L. N. d. O.; Silva, P. H. F. d.; Bell, M. J. V.; Anjos, V. d. C. d., FTIR-ATR determination of protein content to evaluate whey protein concentrate adulteration. *Lwt* **2019,** *99*, 166-172.

102. Monnier, G. F., A review of infrared spectroscopy in microarchaeology: Methods, applications, and recent trends. *Journal of Archaeological Science: Reports* **2018,** *18*, 806-823.

103. White, R. L., Diffuse reflection mid-infrared spectroscopy of neat powders by using a wire mesh “Button” sample holder. *Anal. Chim. Acta* **2020,** *1098*, 110-116.

104. HgCdTe Detector. Serial # J-5385-2. InfraRed Associates, Inc.: New Brunwick, NJ, 1985.

105. Milosevic, M.; Berets, S. L., A review of FT-IR diffuse reflection sampling considerations. *Appl. Spectrosc. Rev.* **2002,** *37* (4), 347-364.

106. Singh, J.; White, R. L., Discrimination of commercial ibuprofen tablets by using a button sample holder and mid-infrared spectroscopy. *Anal Methods* **2022,** *14* (12), 1214-1220.

107. Singh, J.; White, R. L., Mid-infrared spectroscopy of liquids by using a modified button sample holder. *Spectrochim Acta A Mol Biomol Spectrosc* **2022,** *267* (Pt 1), 120526.

108. White, R. L., Requirements for thermal analysis by variable temperature diffuse reflectance infrared spectroscopy. *Appl. Spectrosc.* **1992,** *46*, 1508-1513.

109. White, R. L., Removal of baseline artifacts from variable-temperature diffuse reflectance infrared spectra. *Anal. Chem.* **1992,** *64*, 2010-2013.

110. Lin, R.; White, R. L., Effect of diffuse reflectance Fourier transform infrared spectroscopy sample temperature on photoconducting semiconductor and pyroelectric infrared detectors. *Anal. Chem.* **1994,** *66*, 2976-2980.

111. Paredes-Nunez, A.; Jbir, I.; Bianchi, D.; Meunier, F. C., Spectrum baseline artifacts and correction of gas-phase species signal during diffuse reflectance FT-IR analyses of catalysts at variable temperatures. *Appl. Catal. A* **2015,** *495*, 17-22.

112. Paredes-Nunez, A.; Jbir, I.; Bianchi, D.; Meunier, F. C., Spectrum baseline artefacts and correction of gas-phase species signal during diffuse reflectance FT-IR analyses of catalysts at variable temperatures. *Applied Catalysis A: General* **2015,** *495*, 17-22.

113. White, R. L., Diffuse reflection mid-infrared spectroscopy of neat powders by using a wire mesh “button” sample holder. *Anal. Chim. Acta* **2020,** *1098*, 110-116.

114. John G. Miller, T. D. O., Prototropy in Kaolinite During Percussive Grinding. *Clays and Clay Minerals* **1970,** *18*, 313-323.

115. John G. Miller, T. D. O., Some effects of grinding kaolinite with potassium bromide. *Clays and Clay Minerals* **1972,** *20*, 389-390.

116. White, R. L., Thermal analysis by variable temperature infrared spectroscopy with a button sample holder and Peltier heating/cooling. *Talanta* **2023,** *258*, 124474.

117. Yu, J.; Zhao, H.; Xie, K., Analysis of optimum configuration of two-stage thermoelectric modules. *Cryogenics* **2007,** *47*, 89-93.

118. Ma, M.; Yu, J., An analysis on a two-stage cascade thermoelectric cooler for electronics cooling applications. *Int. J. Refrig.* **2014,** *38*, 352-357.

119. Singh, J.; White, R. L., Multiple path length mid-infrared spectra of liquids obtained by using a modified button sample holder. *Anal Methods* **2022,** *14* (16), 1638-1645.

120. O'Reilly, J. M.; Mosher, R. A., Functional groups in carbon black by FTIR spectroscopy. *Carbon* **1983,** *21* (1), 47-51.

121. Nunes, A. P. L.; Peres, A. E. C.; Chaves, A. P.; Ferreira, W. R., Effect of alkyl chain length of amines on fluorapatite and aluminium phosphates floatabilities. *Journal of Materials Research and Technology* **2019,** *8* (4), 3623-3634.

122. Clarke, R. H.; Londhe, S.; Premasiri, W. R.; Womble, M. E., Low-resolution Raman spectroscopy: instrumentation and applications in chemical analysis. *Journal of Raman Spectroscopy* **1999,** *30* (9), 827-832.

123. Miliani, C.; Ombelli, M.; Morresi, A.; Romani, A., Spectroscopic study of acrylic resins in solid matrices. *Surface and Coatings Technology* **2002,** *151-152*, 276-280.

124. Norbygaard, T.; Berg, R. W., analysis of phthalate ester content in poly(vinyl chloride) plastics by means of fourier transform Raman spectroscopy. *Appl Spectrosc* **2004,** *58* (4), 410-3.

125. Han, W. L., T.; Dai, H.; Su, J., COLORED STONES AND ORGANIC MATERIALS. *Gems and Gemology, Quarterly Journal of the Gemological Institute of America* **2015,** *51* (3), 334-345.

126. Custers, D.; Cauwenbergh, T.; Bothy, J. L.; Courselle, P.; De Beer, J. O.; Apers, S.; Deconinck, E., ATR-FTIR spectroscopy and chemometrics: An interesting tool to discriminate and characterize counterfeit medicines. *J. Pharm. Biomed. Anal.* **2015,** *112*, 181-189.

127. Longoni, M.; Lissana, M.; Bottaro, L.; Malberti, F.; Marzullo, M.; Teseo, D.; Ludwig, N.; Bruni, S., Organic residue analysis in archaeological pottery. Heating markers in non-cooking vessels from Etruscan Tarquinia (Italy): A sampling problem? *Journal of Archaeological Science: Reports* **2024,** *53*.

128. Singh, J.; White, R. L., A variable temperature infrared spectroscopy study of NaA zeolite dehydration. *Vibrational Spectroscopy* **2017,** *94*, 37-42.

129. Kubelka, P.; Munk, F., Ein Beitrag zur Optik der Farbanstriche. *Z. Tech. Phys.* **1931,** *12*, 593-601.

130. Nickels, T. M.; Ingram, A. L.; Maraoulaite, D. K.; White, R. L., Variable temperature infrared spectroscopy investigations of benzoic acid desorption from sodium and calcium montmorillonite clays. *Appl. Spectrosc.* **2015,** *69* (12), 1381-1389.

131. Nickels, T. M.; Ingram, A. L.; Maraoulaite, D. K.; White, R. L., Variable Temperature Infrared Spectroscopy Investigation of Benzoic Acid Interactions with Montmorillonite Clay Interlayer Water. *Appl. Spectrosc.* **2015,** *69* (7), 850-856.

132. White, R. L.; Nair, A., Effect of silica on the thermal degradation of poly(vinyl butyral). *Chem. Mater.* **1990,** *2*, 742-748.

133. White, R. L., Thermal analysis by diffuse reflectance Fourier transform infrared spectroscopy/mass spectroscopy. *J. Anal. Appl. Pyr.* **1991,** *18*, 325-339.

134. White, R. L.; Sikabwe, E. C., Thermal degradation of poly[(E,E)-(6.2) paracyclophane-1,5-diene]. *J. Polym. Sci.: Polym. Chem.* **1992,** *30*, 2781-2790.

135. White, R. L.; Ai, J., Variable temperature diffuse reflectance infrared studies of calcium oxalate monohydrate. *Appl. Spectrosc.* **1992,** *46*, 93-99.

136. White, R. L.; Ai, J., Effect of silica on the non-oxidative thermal degradation of poly(vinyl butyral). *Chem. Mater.* **1992,** *4*, 233-239.

137. White, R. L., VT-DRIFTS: a two-dimensional infrared thermal analysis method. *Appl. Spectrosc.* **1993,** *47*, 1492-1496.

138. Ai, J.; Phegley, L. L.; Christen, G.; White, R. L., Effect of silica on the non-oxidative thermal degradation of an acrylic ceramic binder. *J. Am. Ceram. Soc.* **1995,** *78*, 874-880.

139. White, R. L.; Nair, A., Diffuse reflectance infrared spectroscopic characterization of silica dehydroxylation. *Appl. Spectrosc.* **1990,** *44*, 69-75.

140. White, R. L., Variable temperature diffuse reflectance Fourier transform infrared spectroscopy. *Rec. Res. Dev. Appl. Spectrosc.* **1996,** *1*, 1-8.

141. Lin, R.; White, R. L., A ceramic sample heater for variable temperature diffuse reflectance Fourier transform infrared spectroscopy. *Instr. Sci. Tech.* **1996,** *24*, 37-45.

142. White, R. L.; Negelein, D. L., Studies of polymer-substrate interactions using variable-temperature diffuse reflectance FTIR spectroscopy. *Am. Lab.* **1998,** *30* (1), 33-35.

143. White, R. L.; Negelein, D. L., VT-DRIFTS studies of polymer thermal decompositions. *Proc. SPE* **1999**, 2490-2494.

144. White, D. R.; White, R. L., Isoconversion effective activation energies obtained by variable temperature diffuse reflectance infrared spectroscopy. *Appl. Spectrosc.* **2008,** *62* (1), 116-120.

145. Ingram, A. L.; Nickels, T. M.; Maraoulaite, D. K.; White, R. L., Variable temperature infraredsSpectroscopy studies of aromatic acid adsorbate effects on montmorillonite dehydration. *Appl. Spectrosc.* **2017,** *71* (2), 238-249.

146. Maraoulaite, D. K. Temperature-induced spectral artifacts inFourier transform infrared (FTIR) spectroscopy, optimization of variable temperature diffuse reflection FTIR spectroscopy instrumentation. Dissertation, University of Oklahoma, 2016.

147. Kloprogge, J., *Spectroscopic methods in the study of kaolin minerals and their modifications*. Springer Nature Switzerland AG: Cham, Switzerland, 2019; p 428.

148. Cheng, H.; Frost, R. L.; Yang, J.; Liu, Q.; He, J., Infrared and infrared emission spectroscopic study of typical Chinese kaolinite and halloysite. *Spectrochim. Acta A* **2010,** *77* (5), 1014-20.

149. Prost, R.; Dameme, A.; Huard, E.; Driard, J.; Leydecker, J. P., Infrared study of structural OH in kaolinite, dickite, nacrite, and poorly crystalline kaolinite at 5 to 600 K. *Clay Clay Miner.* **1989,** *37* (5), 464-468.

150. Aroke, U. O.; Abdulkarim, A.; Ogubunka, R. O., Fourier-transfrom infrared characterization of kaolin, granite, betonite, and barite. *J. Environ, Tech,* **2013,** *6* (1), 42-53.

151. Marel, H. W. v. d.; Krohmer, P., OH stretching vibrations in kaolinite, and related minerals. *Contrib. Mineral. Petr.* **1969,** *22*, 73-82.

152. Cuadros, J.; Vega, R.; Toscano, A., Mid-infrared features of kaolinite-dickite. *Clay Clay Miner.* **2015,** *63* (2), 73-84.

153. Brindley, G. W.; Kurtossy, S. S., Quantitative determination of kaolinite By x-ray diffraction. *J. Mineral. Soc. Am.* **1961,** *46* (11, 12), 1205-1215.

154. Ekosse, G. I. E., Fourier transform infrared spectrophotometry and x-ray powder diffractometry as complementary techniques in characterizing clay size fraction of kaolin. *J. Appl. Sci. Environ. Mgt.* **2005,** *9* (2), 43-48.

155. Jr., R. F. G.; Datta, P., Hydroxyl orentation in kaolinite, dickite, and nacrite. *Am. Mineral.* **1973,** *58*, 471-479.

156. Bougeard, D.; Smirnov, K. S.; Geidel, E., Vibrational spectra and structure of kaolinite: a computer simulation study. *J. Phys. Chem. B* **2000,** *104*, 9210-9217.

157. White, C. E.; Provis, J. L.; Riley, D. P.; Kearley, G. J.; Deventer, J. S. J. v., What Is the structure of kaolinite? reconciling theory and experiment. *J. Phys. Chem. B* **2009,** *113*, 6756-6765.

158. Frost, R. L.; Kloprogge, J. T., Raman spectroscopy of kaolinite hydroxyls between 25 C and 500 C. *J. Raman Spectrosc.* **2000,** *31*, 415-420.

159. Tosoni, S.; Doll, K.; Ugliengo, P., Hydrogen bond in layered materials: structural and vibrational properties of kaolinite by a periodic B3LYP approach. *Chem. Mater.* **2006,** *18*, 2135-2143.

160. Castro, R.; Pozzi, F.; Leona, M.; Melo, M. J., Combining SERS and microspectrofluorimetry with historically accurate reconstructions for the characterization of lac dye paints in medieval manuscript illuminations. *J. Raman Spectrosc.* **2014,** *45* (11-12), 1172-1179.

161. Weck, P. F.; Kim, E.; Jove-Colon, C. F., Relationship between crystal structure and thermo-mechanical properties of kaolinite clay: beyond standard density functional theory. *Dalton T.* **2015,** *44* (28), 12550-60.

162. Castro, E. A. S.; Martins, J. B. L., Theoretical study of kaolinite. *Int. J. Quantum Chem.* **2005,** *103*, 550-556.

163. Tunega, D.; Bucko, T.; Zaoui, A., Assessment of ten DFT methods in predicting structures of sheet silicates: importance of dispersion corrections. *J. Chem. Phys.* **2012,** *137* (11), 114105.

164. Bish, D. L., Rietveld Refinement of the Kaolinite Structure at 1.5 K. *Clays and Clay Minerals* **1993,** *41* (6), 738-744.

165. Momma, K.; Izumi, F., VESTA 3for three-dimensional visualization of crystal, volumetric and morphology data. *Journal of Applied Crystallography* **2011,** *44* (6), 1272-1276.

166. Rahier, H.; Wullaert, B.; Mele, B. V., Influence of the degree of dehydroxylation of kaolinite on the properties of aluminosilicate glasses. *J. Therm. Anal. Calorim.* **2000,** *62*, 417-427.

167. Drits, V. A.; Derkowski, A.; Sakharov, B. A.; Zviagina, B. B., Experimental evidence of the formation of intermediate phases during transition of kaolinite into metakaolinite. *Am. Mineral.* **2016,** *101*, 2331-2346.

168. Artioli, G., In situ powder diffraction studies of temperature induced transformations in minerals. *Nucl. Instrum. Meth. B* **1997,** *133*, 45-49.

169. White, C. E.; Kearley, G. J.; Provis, J. L.; Riley, D. P., Inelastic neutron scattering analysis of the thermal decomposition of kaolinite to metakaolin. *Chem. Phys.* **2013,** *427*, 82-86.

170. Khana, M. I.; Khan, H. U.; Azizli, K.; Sufian, S.; Man, Z.; Siyal, A. A.; Muhammad, N.; Rehmanb, M. F. u., The pyrolysis kinetics of the conversion of Malaysian kaolin to metakaolin. *Appl. Clay Sci.* **2017,** *146*, 152-161.

171. Gasparini, E.; Tarantino, S. C.; Ghigna, P.; Riccardi, M. P.; Cedillo-González, E. I.; Siligardi, C.; Zema, M., Thermal dehydroxylation of kaolinite under isothermal conditions. *Appl. Clay Sci.* **2013,** *80* (81), 417-425.

172. Singh, J.; White, R. L., A variable temperature infrared spectroscopy study of NaA zeolite dehydration. *Vib. Spectrosc.* **2018,** *94*, 37-42.

173. Singh, J.; White, R. L., A variable temperature infrared spectroscopy study of CaA zeolite dehydration and carbonate formation. *Spectrochim. Acta A* **2019,** *207*, 189-196.

174. Singh, J.; White, R. L., A variable temperature infrared spectroscopy study of NaY zeolite dehydration. *Spectrochim. Acta A* **2020,** *231*, 118142.

175. Maraoulaite, D.; White, R. L., Optical efficiency effects on infrared diffuse reflection spectroscopy signal-to-noise ratio. *Am. Lab.* **2018,** *50* (4), 14-17.

176. Balan, E.; Lazzeri, M.; Saitta, A. M.; Allard, T.; Y. Fuchs; Mauri, F., First-principles study of OH-stretching modes in kaolinite, dickite, and nacrite. *Am. Mineral.* **2005,** *90*, 50-60.

177. Frost, R. L., Hydroxyl deformation in kaolins. *Clay Clay Miner.* **1998,** *46* (3), 280-289.

178. Balan, E.; Saitta, A. M.; Mauri, F.; Calas, G., First-principles modeling of the infrared spectrum of kaolinite. *Am. Mineral.* **2001,** *86*, 1321-1330.

179. Miller, J. G.; Oulton, T. D., Prototropy in kaolinite during percussive grinding. *Clay Clay Miner.* **1970,** *18*, 313-323.

180. Miller, J. G.; Oulton, T. D., Some effects of grinding kaolinite with potassium bromide. *Clay Clay Miner.* **1972,** *20*, 389-390.

181. Griffith, W., Advances in the Raman and infrared spectroscopy of minerals. In *Advances in Spectroscopy (Chichester (West Sussex))*, Wiley: Chichester, UK, 1987; Vol. 14, pp 119-186.

182. Chukanov, N. V.; Chervannyi, A. D., *Infrared spectroscopy of minerals and related compounds*. Springer: New York, NY, USA, 2016.

183. Hunt, J. M.; Turner, D. S., Determination of mineral constituents of rocks by infrared spectroscopy. *Anal. Chem.* **1953,** *25* (8), 1169-1174.

184. Chukanov, N. V., *Infrared spectra of mineral species: extended library*. Springer: New York, NY, USA, 2014.

185. Craddock, P. R.; Herron, M. M.; Herron, S. L., Comparison of quantitative mineral analysis by x-ray diffraction and Fourier transform infrared spectroscopy. *J. Sediment. Res.* **2017,** *87* (6), 630-652.

186. Arean, C. O.; Manoilova, O. V.; Tsyganenko, A. A.; Palomino, G. T.; Mentruit, M. P.; Geobaldo, F.; Garrone, E., Thermodynamics of hydrogen bonding between CO and the supercage bronsted acid sites of the H-Y zeolite - studies from variable temperature IR spectrometry. *Eur. J. Inorg. Chem.* **2001,** *2001* (7), 1739-1743.

187. Garrone, E.; Arean, C. O., Variable temperature infrared spectroscopy: a convenient tool for studying the thermodynamics of weak solid-gas interactions. *Chem. Soc. Rev.* **2005,** *34* (10), 846-857.

188. Vilagosh, Z.; Lajevardipour, A.; Appadoo, D.; Juodkazis, S.; Wood, A. W., Using attenuated total reflection (ATR) apparatus to investigate the temperature depennent dielectric properties of water, ice, and tissue-representative fats. *Appl. Sci.* **2021,** *11*, 2544.

189. Schramm, C., High temperature ATR-FTIR characterization of the interaction of polycarboxylic acids and organotrialkoxysilanes with cellulosic material. *Spectrochim. Acta A Mol. Biomol. Spectrosc.* **2020,** *243*, 118815.

190. Singh, J.; White, R. L., Variable temperature infrared spectroscopy with a button sample holder and thermoelectric heating/cooling. *Anal. Chim. Acta* **2022,** *1198*, 339558.

191. White, R. L., Precise temperature control and rapid heating/cooling of infrared spectroscopy samples with a two-stage thermoelectric device. *Anal Methods* **2023,** *15* (48), 6706-6715.

192. Fuller, M. P.; Griffiths, P. R., Diffuse reflectance measurements by infrared Fourier transform spectrometry. *Anal. Chem.* **1978,** *50* (13), 1906-1910.

193. Kokhanovsky, A. A., Physical interpretation and accuracy of the Kubelka-Munk theory. *J. Phys. D: Appl. Phys.* **2007,** *40*, 2210-2216.

194. Hebert, M.; Hersch, R. D.; Becker, J. M., Compositional reflectance and transmittance model for multilayer specimens. *J. Opt. Soc. Am. A* **2007,** *24* (8), 2628-2644.

195. Kubelka, P., New contributions to the optics of intensely light-scattering materials. Part I. *J. Opt. Soc. Am.* **1948,** *38* (5), 448-457.

196. Korte, E. H.; Roseler, A., Infrared restrahlen revisited: commonly disregarded optical details related to n < 1. *Anal. Bioanal. Chem.* **2005,** *382* (8), 1987-1992.

197. Martin, K. A.; Ferraro, J. R., Restrahlen effects in DRIFT experiments of alkali metal halides in the far-infrared region. *Appl. Spectrosc.* **1987,** *41* (1), 45-49.

198. Project, R. IMA database of mineral properties. https://rruff.info/ima/ (accessed 5/28/2024)

199. White, R. L., Thermal analysis by variable vemperature infrared spectroscopy with a button sample holder and peltier heating/cooling. *Talanta* **2023,** *258*, 124474.

200. White, R. L., Precise temperature control and rapid heating/cooling of infrared spectroscopy samples with a two-stage thermoelectric device. *Anal. Meth.* **2023,** *15*, 6706-6715.

201. Fuller, M. P.; Griffiths, P. R., Diffuse reflectance measurements by infrared Fourier transform spectrometry. *Analytical Chemistry* **1978,** *50* (13), 1906-1910.

202. Singh, J. Applications of Button Sample Holders for Mid-Infrared Spectroscopy Measurements. Dissertation, University of Oklahoms, ShareOK Creative Commons, 2021.

203. Dichicco, M. C.; De Bonis, A.; Mongelli, G.; Rizzo, G.; Sinisi, R., μ-Raman spectroscopy and X-ray diffraction of asbestos' minerals for geo-environmental monitoring: The case of the southern Apennines natural sources. *Applied Clay Science* **2017,** *141*, 292-299.

204. Dunn, T. L.; Cressey, G.; McSween Jr, H. Y.; McCoy, T. J., Analysis of ordinary chondrites using powder X-ray diffraction: 1. Modal mineral abundances. *Meteoritics and Planetary Science* **2010**.

205. Farmer, V. C., The infra-red spectra of talc, saponite, and hectorite. *Mineralogical Magazine and Journal of the Mineralogical Society* **1958,** *31* (241), 829-845.

206. Farmer, V. C.; Lumsdon, D. G., An assessment of complex formation between aluminium and silicic acid in acidic solutions. *Geochimica et Cosmochimica Acta* **1994,** *58* (16), 3331-3334.

207. Petit, S., Chapter 12.6 Fourier Transform Infrared Spectroscopy. In *Handbook of Clay Science*, 2006; pp 909-918.

208. Critelli, S.; Muto, F.; Perri, F.; Tripodi, V., Interpreting provenance relations from sandstone detrital modes, southern Italy foreland region: Stratigraphic record of the Miocene tectonic evolution. *Marine and Petroleum Geology* **2017,** *87*, 47-59.

209. Weltje, G. J.; von Eynatten, H., Quantitative provenance analysis of sediments: review and outlook. *Sedimentary Geology* **2004,** *171* (1-4), 1-11.

210. Kholoshyn, I.; Panteleeva, N.; Trunin, O.; Burman, L.; Kalinichenko, O., Infrared spectroscopy as the method for evaluating technological properties of minerals and their behavior in technological processes. *E3S Web of Conferences* **2020,** *166*.

211. Periodic Table. https://periodic-table.rsc.org/ (accessed March 2025)

212. Gotze, J.; Pan, Y.; Muller, A., Mineralogy and mineral chemistry of quartz: A review. *Mineral. Mag.* **2021,** *85*, 639-664.

213. Gotze, J., Chemistry, textures and physical properties of quartz - geological interpretation and technical application. *Mineral. Mag.* **2009,** *73* (4), 645-671.

214. Rosa, A. L.; El-Barbary, A. A.; Heggie, M. I.; Briddon, P. R., Structural and thermodynamic properties of water related defects in α-quartz. *Physics and Chemistry of Minerals* **2005,** *32* (5-6), 323-331.

215. Glinnemann, J.; King Jr, H. E.; Schulz, H.; Hahn, T.; La Placa, S. J.; Dacol, F., Crystal structures of the low-temperature quartz-type phases of SiO2 and GeO2 at elevated pressure. *Zeitschrift für Kristallographie - Crystalline Materials* **1992,** *198* (1-4), 177-212.

216. Alderson, A.; Evans, K. E., Deformation mechanisms leading to auxetic behaviour in the α-cristobalite and α-quartz structures of both silica and germania. *Journal of Physics: Condensed Matter* **2009,** *21* (2).

217. Borhara, K.; Onasch, C. M., Evidence for silica gel and its role in faulting in the Tuscarora sandstone. *J. Struct. Geol.* **2020,** *139*, 104140.

218. Li, P.; Ohtsuki, C.; Kokubo, T.; Nakanishi, K.; Soga, N.; Nakamura, T.; Yamamuro, T., Apatite Formation Induced by Silica Gel in a Simulated Body Fluid. *Journal of the American Ceramic Society* **2005,** *75* (8), 2094-2097.

219. Leal, O.; Bolívar, C.; Ovalles, C.; García, J. J.; Espidel, Y., Reversible adsorption of carbon dioxide on amine surface-bonded silica gel. *Inorganica Chimica Acta* **1995,** *240* (1-2), 183-189.

220. Siouffi, A. M., Silica gel-based monoliths prepared by the sol-gel method: facts and figures. *J Chromatogr A* **2003,** *1000* (1-2), 801-18.

221. Kalapathy, U., A simple method for production of pure silica from rice hull ash. *Bioresource Technology* **2000,** *73* (3), 257-262.

222. Younssi, E.; Rhadfi, T.; Atlamsani, A.; J.P. Quisefit; Herbst, F.; Draoui, K., K-10 montmorillonite: an efficient and reusable catalyst for the aerobic C-C bond

cleavage of alpha-substituted ketones. *J. Mol. Catal. A Chem.* **2012**, 363-364, 437-445.

223. Ingram, A. L.; Nickels, T. M.; Maraoulaite, D. K.; White, R. L., Thermogravimetry-mass spectrometry investigations of montmorillonite interlayer water perturbations caused by aromatic acid adsorbates. *J. Therm. Anal. Calorim.* **2016,** *126*, 1157-1166.

224. Mering, J., Smectites. In *Soil Components*, Gieseking, J. E., Ed. Springer-Verlag: New York, 1975; Vol. 2, pp 97-119.

225. Gournis, D.; Lappas, A.; Karakassides, M. A.; Többens, D.; Moukarika, A., A neutron diffraction study of alkali cation migration in montmorillonites. *Physics and Chemistry of Minerals* **2007,** *35* (1), 49-58.

226. Gates, W. P.; Bordallo, H. N.; Aldridge, L. P.; Seydel, T.; Jacobsen, H.; Marry, V.; Churchman, G. J., Neutron Time-of-Flight Quantification of Water Desorption Isotherms of Montmorillonite. *J. Phys. Chem. C* **2012,** *116* (9), 5558-5570.

227. Emmerich, K.; Koeniger, F.; Kaden, H.; Thissen, P., Microscopic structure and properties of discrete water layer in Na-exchanged montmorillonite. *J. Colloid Interf. Sci.* **2015,** *448*, 24-31.

228. Zviagina, B. B.; McCarty, D. K.; Srodon, J.; Drits, V. A., Interpretation of infrared spectra of dioctahedral smectites in the region of OH-stretching vibrations. *Clays Clay Miner.* **2004,** *52* (4), 399-410.

229. Miller, W. P.; Sumner, M. E., Agricultural and industrial uses of by-product gypsums. In *Agricultural uses of by-products and wastes*, Rechcigl, J. E.; MacKinnon, H. C., Eds. 1997; Vol. 668, pp 226-239.

230. Watts, D. B.; Dick, W. A., Sustainable uses of FGD gypsum in agricultural systems: introduction. *J. Environ. Qual.* **2014,** *43*, 246-252.

231. Thomas, M. V.; Puleo, D. A., Calcium sulfate: properties and clinical applications. *J. Biomed. Mater. Res. Part B: Appl. Biomater.* **2009,** *88B*, 597-610.

232. Gypsum. https://virtual-museum.soils.wisc.edu/display/gypsum/ (accessed October 15, 2025)

233. Schofield, P. F.; Knight, K. S.; Stretton, I. C., Thermal expansion of gypsum investigated by neutron powder diffraction. *American Mineralogist* **1996,** *81* (7-8), 847-851.

234. Pedersen, B. F.; Semmingsen, D., Neutron diffraction refinement of the structure of gypsum, CaSO4-2H2O. *Acta Cryst.* **1982,** *B38*, 1074-1077.

235. Yan, C.; Nishida, J.; Yuan, R.; Fayer, M. D., Water of hydration dynamics in minerals gypsum and bassanite: ultrafast 2D IR spectroscopy of rocks. *J. Am. Chem. Soc.* **2016,** *138*, 9694-9703.

236. Rosi, F.; Daveri, A.; Doherty, B.; Nazzareni, S.; Brunetti, B. G.; Sgamellotti, A.; Miliani, C., On the use of overtone and combination bands for the analysis of the CaSO4-H2O system by mid-infrared reflection spectroscopy. *Appl. Spectrosc.* **2010,** *64* (8), 956-963.

237. Iwasaki, S.; Zushi, Y.; Koga, N., An advanced kinetic approach to the multistep thermal dehydration of calcium sulfate dihydrate under different heating and water vapor conditions: kinetic deconvolution and universal isoconversional analyses. *Phys. Chem. Chem. Phys.* **2022,** *24*, 9492-0508.

238. Preturlan, J. G. D.; Vieille, L.; Quiligotti, S.; Favergeon, L., Kinetics and mechanism of the dehydration of calcium sulfate dihydrate: a comprehensive approach for studying the dehydration of ionic hydrates under controlled temperature and water vapor pressure. *J. Phys. Chem. C* **2020,** *124*, 26352-26367.

239. Lou, W.; Guan, B.; Wu, Z., Dehydration behavior of FGD gypsum by simultaneous TG and DSC analysis. *J. Therm. Anal. Calorim.* **2011,** *104*, 661-669.

240. Hudson-Lamb, D. L.; Strydom, C. A.; Potgieter, J. H., The thermal dehydration of natural gypsum and pure calcium sulphate dihydrate (gypsum). *Thermochim. Acta* **1996,** *282/283*, 483-492.

241. Iwasaki, S.; Zushi, Y.; Koga, N., An advanced kinetic approach to the multistep thermal dehydration of calcium sulfate dihydrate under different heating and water vapor conditions: kinetic deconvolution and universal isoconversional analyses. *Phys Chem Chem Phys* **2022,** *24* (16), 9492-9508.

242. Anbalagan, G.; Mukundakumari, S.; Murugesan, K. S.; Gunasekaran, S., Infrared, optical absorption, and EPR spectroscopic studies on natural gypsum. *Vib. Spectrosc.* **2009,** *50*, 226-230.

243. Prasad, P. S. R.; Chaitanya, V. K.; Prasad, K. S.; Rao, D. N., Direct formation of the gamma-CaSO4 phase in dehydration process of gypsum: . *Am. Mineral.* **2005,** *90*, 672-678.

244. Bensted, J.; Prakash, S., Investigation of the calcium sulphate-water system by infrared spectroscopy. *Nature* **1968,** *219*, 60-61.

245. O'Keefe, J. M. K.; Bechtel, A.; Christanis, K.; Dai, S.; DiMichele, W. A.; Eble, C. F.; Esterle, J. S.; Mastalerz, M.; Raymond, A. L.; Valentim, B. V.; Wagner, N. J.; Ward, C. R.; Hower, J. C., On the fundamental difference between coal rank and coal type. *Int. J. Coal Geol.* **2013,** *118*, 58-87.

246. Finkelman, R. B.; Dai, S.; French, D., The importance of minerals in coal as the hosts of chemical elements: a review. *Int. J. Coal Geol.* **2019,** *212*, 103251.

247. Rosa Martínez-Tarazona, M.; Martínez-Alonso, A.; Tascón, J. M. D., Characterization of common lignite, xylitic lignite and pyropissite varieties of low-rank coals. *Fuel* **1994,** *73* (11), 1723-1728.

248. Teichmüller, M., The genesis of coal from the viewpoint of coal petrology. *International Journal of Coal Geology* **1989,** *12* (1-4), 1-87.

249. Wingo, O. T., Investigation of lignite coal. Mining, C. o. M. a., Ed. ProQuest ProQuest Congressional: House and Senate Reports - Reports on Public Bill, 1918; Vol. 1:7454, p 10.

250. Xu, T.; Pisupati, S. V.; Bhattacharya, S., Comparison of entrained flow CO2 gasification behaviour of three low-rank coals – Victorian brown coal, Beulah lignite, and Inner Mongolia lignite. *Fuel* **2019,** *249*, 206-218.

251. Wang, C.; Xing, Y.; Shi, K.; Wang, S.; Xia, Y.; Li, J.; Gui, X., Chemical Structure Characteristics and Model Construction of Coal with Three Kinds of Coalification Degrees. *ACS Omega* **2024,** *9* (1), 1881-1893.

252. Dai, F.; Zhuang, Q.; Huang, G.; Deng, H.; Zhang, X., Infrared spectrum characteristics and quantification of OH groups in coal. *ACS Omega* **2023,** *8*, 17064-17076.

253. Tahmasebi, A.; Yu, J.; Han, Y.; Yin, F.; Bhattacharya, S.; Stokie, D., Study of chemical structure changes of chinese lignite upon drying in superheated steam, microwave, and hot air. *Energ. Fuels* **2012,** *26*, 3651-3660.

254. Loghinov, A. P.; Kozyrenko, V. N.; Mikhailov, I. D.; Chukhanov, N. V.; Kumpanenko, I. V., Generalized coupled oscillator model for defect polymers. I. calculation of frequency branches of n-paraffins, fatty acids and glymes. *Chem. Phys.* **1979,** *36* (2), 187-196.

255. Painter, P. C.; Starsinic, M.; Squires, E.; Davis, A. A., Concerning the 1600 cm-1 region in the i.r. spectrum of coal. *Fuel* **1983,** *62* (6), 742-744.

256. Geng, W.; Nakajima, T.; Takanashi, H.; Ohki, A., Analysis of carboxyl group in coal and coal aromaticity by Fourier transform infrared (FT-IR) spectrometry. *Fuel* **2009,** *88*, 139-144.

Appendix A – Mesh Photos and Laser Scattering Properties

50 Mesh

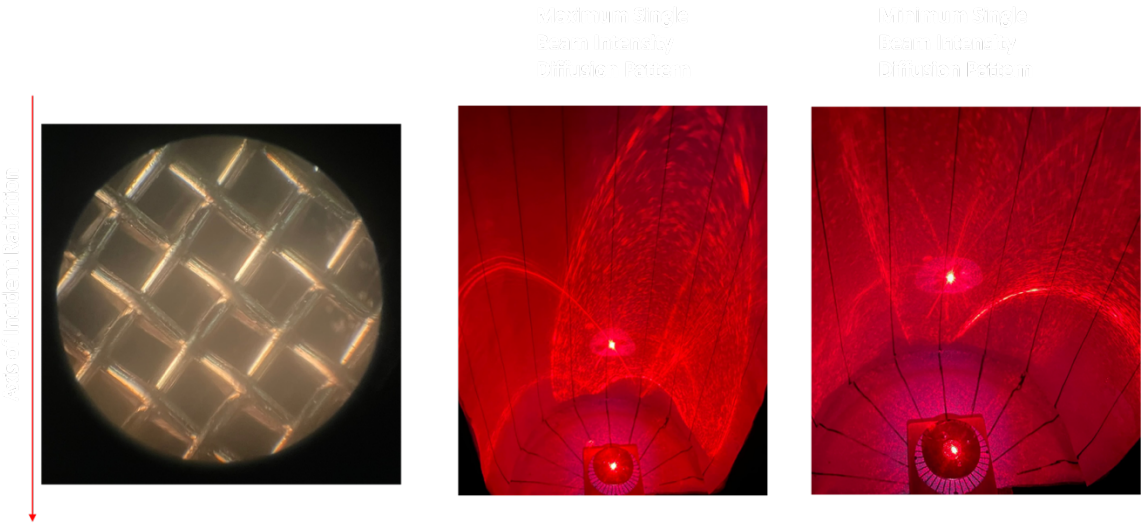

100 mesh

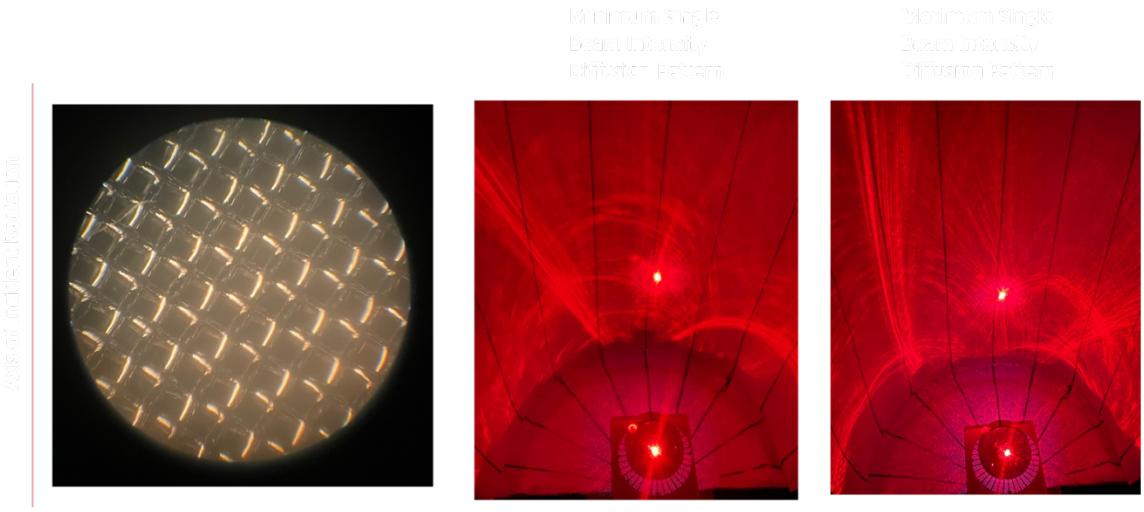

200 mesh

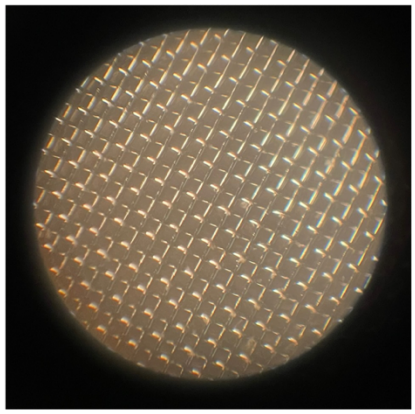

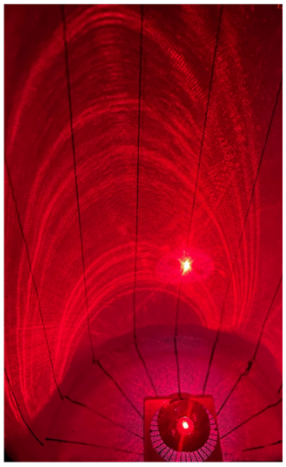



635 mesh

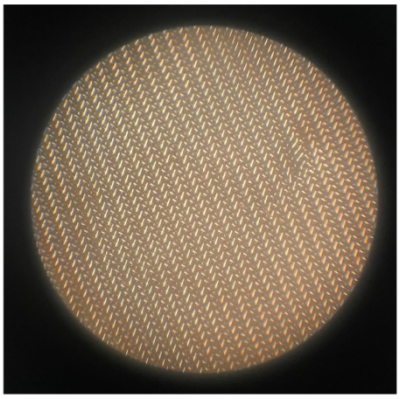





2800 mesh

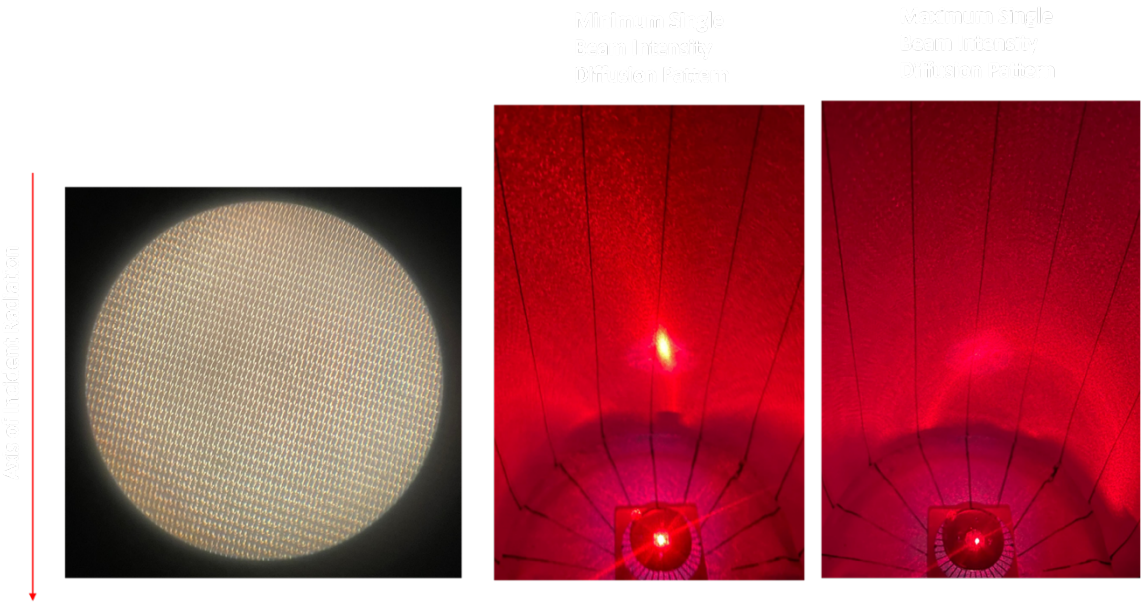
Minimum Single Beam Intensity Diffusion Pattern
Maximum Single Beam Intensity Diffusion Pattern

Appendix B – Crystal Modeling Parameters

Montmorillonite Crystal Lattice Parameters
Si3.9 Al.86 Li.08 Fe.1 Mg.14 O10 H
Space Group: C 2/m (#12-1)
a = 5.17500 Å α = 90.0000°
b = 8.89600 Å β = 99.6900°
c = 12.45000 Å γ = 90.0000°
V = 564.9808 Å^3

Gypsum Crystal Lattice Parameters
Ca S O6 D4
Space Group: I 2/c (#15-12)
a = 5.67400 Å α = 90.0000°
b = 15.10490 Å β =118.5130°
c = 6.49090 Å γ = 90.0000°
V = 488.8291 Å^3

Kaolinite Crystal Lattice Parameters
Al2 Si2 O9 H4
Space Group: C 1 (#1-4)
a = 5.15350 Å α = 91.9260°
b = 8.94190 Å β =105.0460°
c = 7.39060 Å γ = 89.7970°
V = 328.7081 Å^3

Alpha Quartz Crystal Lattice Parameters Measured
Si O2
Space Group: Custom (#1-1)
a = 4.92100 Å α = 90.0000°
b = 4.92100 Å β = 90.0000°
c = 5.41630 Å γ =120.0000°
V = 113.5900 Å^3

Alpha Quartz Crystal Lattice Parameters Modelled
Si O2
Space Group: Custom (#1-1)
a = 4.98000 Å α = 90.0000°
b = 4.98000 Å β = 90.0000°
c = 5.46000 Å γ =120.0000°
V = 117.2687 Å^3

Appendix C – Copyright

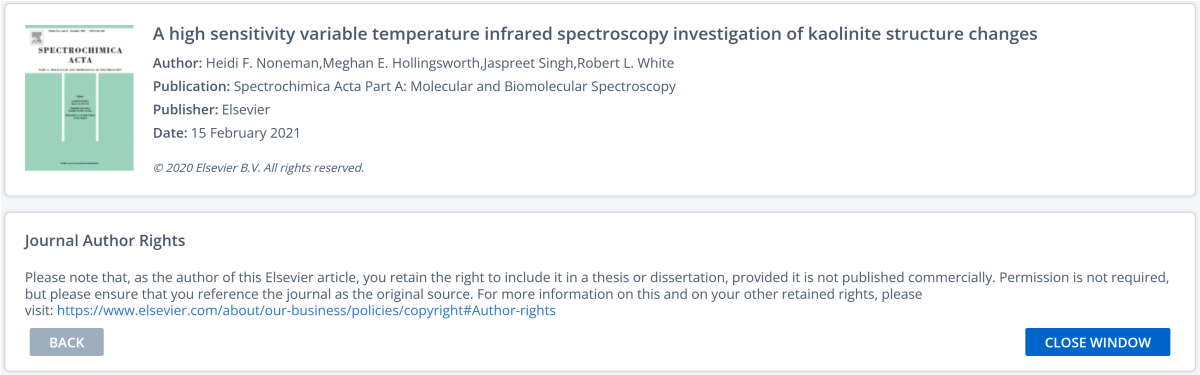

A high sensitivity variable temperature infrared spectroscopy investigation of kaolinite structure changes

Author: Heidi F. Noneman,Meghan E. Hollingsworth,Jaspreet Singh,Robert L. White

Publication: Spectrochimica Acta Part A: Molecular and Biomolecular Spectroscopy

Publisher: Elsevier

Date: 15 February 2021

© 2020 Elsevier B.V. All rights reserved.

Journal Author Rights

Please note that, as the author of this Elsevier article, you retain the right to include it in a thesis or dissertation, provided it is not published commercially. Permission is not required, but please ensure that you reference the journal as the original source. For more information on this and on your other retained rights, please visit: https://www.elsevier.com/about/our-business/policies/copyright#Author-rights

BACK CLOSE WINDOW

Noneman, H. F., Hollingsworth, M. E., Singh, J. & White, R. L. A high sensitivity variable temperature infrared spectroscopy investigation of kaolinite structure changes. *Spectrochimica Acta Part A: Molecular and Biomolecular Spectroscopy* 247, 119113 (**2021**).

Noneman, H. F., White, R. L. Temperature perturbation infrared spectroscopy of minerals. *Minerals, 14*(6), 624 (2024)

Copyright and Licensing
For all articles published in MDPI journals, copyright is retained by the authors. Articles are licensed under an open access Creative Commons CC BY 4.0 license, meaning that anyone may download and read the paper for free.